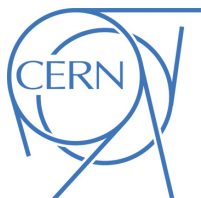




ATLAS Note

ANA-HDBS-2020-09-INT1

31st October 2022



Draft version 0.1

1

2 Search for $t\bar{b}$ resonance using boosted top-quark 3 topology in the lepton+jets final state at $\sqrt{s} = 13$ 4 TeV with the ATLAS detector

5

De La Torre Perez, Hector^a, Gombas, Jason Peter^a, Schwienhorst, Reinhard^a,
6 Sato, Koji^b, Hirose, Shigeki^b, Yamauchi, Hiroki^b, Salvador Salas, Adrian^c, Riu,
7 Imma^c, Mir Martinez, Lluisa Maria^c

8

^a*Michigan State University (US)*

9

^b*University of Tsukuba (JP)*

10

^c*The Barcelona Institute of Science and Technology (BIST) (ES)*

11

A search for $t\bar{b}$ resonances with a boosted top tagging technique is presented, focusing on a final state consisting of a single charged lepton and multiple jets as well as a top-tagged large- R jet. The analysis is based on the pp collision data at the centre-of-mass energy of 13 TeV collected with the ATLAS detector with an integrated luminosity of 139 fb^{-1} . As a hypothetical particle with spin-0(1), a charged Higgs boson (a W' boson) scenario is searched in the mass range from 1 TeV up to 5 TeV.

17

© 2022 CERN for the benefit of the ATLAS Collaboration.

18

Reproduction of this article or parts of it is allowed as specified in the CC-BY-4.0 license.

19 **Contents**

20	1 Introduction	7
21	2 Data and MonteCarlo Simulated Events	9
22	2.1 Data Sample	9
23	2.2 Signal Samples	9
24	2.2.1 $\bar{t}bH^+$ Samples	10
25	2.3 Background Samples	10
26	2.3.1 $t\bar{t}$ +jets	11
27	2.3.2 $t\bar{t}H$	12
28	2.3.3 $t\bar{t}V$	12
29	2.3.4 Single top	12
30	2.3.5 tH	13
31	2.3.6 Rare t processes	14
32	2.3.7 Vector bosons plus jets	14
33	2.3.8 Dibosons	15
34	3 Object Reconstruction	16
35	3.1 Electrons	16
36	3.2 Muons	16
37	3.3 Taus	16
38	3.4 Small- R jets and b -tagging	16
39	3.5 Large- R jets and top-tagging	17
40	3.6 Overlap Removal	17
41	4 Analysis Strategy	19
42	4.1 Event Selection	19
43	4.1.1 Signal region (SR)	19
44	4.1.2 Control region (CR)	20
45	4.1.3 Summary	21
46	4.2 Multivariable analysis using BDT	22
47	4.2.1 Signal and background definition in BDT training	22
48	4.2.2 BDT training settings	23
49	4.2.3 Input variables in BDT	24
50	4.2.4 Results of BDT training	26
51	5 Background modeling	32
52	5.1 Blind strategy	32
53	5.2 Data/MC comparison for BDT input variables	32
54	5.3 Data/MC comparison for BDT distributions	34
55	5.4 Reweighting technique	38
56	6 Systematics Uncertainties	45
57	6.1 Luminosity and pile-up modeling	45
58	6.1.1 Luminosity	45
59	6.1.2 Pile-up modeling	45

60	6.2	Reconstructed objects	45
61	6.2.1	Charged leptons	45
62	6.2.2	Small- R jets, Large- R jets	47
63	6.3	Signal modeling	49
64	6.3.1	H^+ signal	49
65	6.4	Background modeling	49
66	6.4.1	$t\bar{t}$ +jets	49
67	6.4.2	Other backgrounds	51
68	7	Profile Likelihood Fit (Without reweighting)	53
69	7.1	Method	53
70	7.2	Pruning and smoothing of systematic uncertainties	53
71	7.3	Asimov fit results	54
72	7.4	Post-fit plots for Asimov fit	71
73	7.5	Asimov fit results summary	75
74	7.6	Upper cross-section limits as a function of the H^+ mass	76
75	8	Test of tbW' generation	77
76	8.1	tbW' MC generation in private	77
77	8.2	Kinematics study in truth level	77
78	8.2.1	Reconstructed truth objects	77
79	8.2.2	Event selection	78
80	8.2.3	Kinematics comparison with tbH^+ events	78
81	9	Summary and Conclusions	84
82	Appendices		93
83	A	TOPQ1 DAOD list	93
84	A.1	Data	93
85	A.2	$\bar{t}bH^+$	93
86	A.3	$t\bar{t}$ + jets	93
87	A.4	$t\bar{t}H$	94
88	A.5	$t\bar{t}V$	95
89	A.6	Single top	95
90	A.7	tH	96
91	A.8	Rare t processes	96
92	A.9	Vector bosons plus jets	96
93	A.9.1	W + jets	96
94	A.9.2	Z + jets	97
95	A.10	Diboson	99
96	B	Signal/background comparisons	100
97	B.1	BDT input variables	100
98	B.2	BDT output	102
99	B.3	H_T^{jets} distribution in CR	108

100 **C Pruning**
101 C.1 Asimov fit

109
109

102 List of contributions

De La Torre Perez, Hector	W' vs H+ comparisons, W' generation
Gombas, Jason Peter	W' NLO model, W' vs H+ comparisons, W' generation
Schwienhorst, Reinhard	W' NLO model, Jason supervision
Sato, Koji	Analysis contact, supervision of Hiroki
Hirose, Shigeki	Analysis contact, ntuple production, BDT training, MC production, supervision of Hiroki
103 Yamauchi, Hiroki	Main analyser: ntuple production, fit studies and limits extraction
Salvador Salas, Adrian	Main analyser of resolved analysis, providing technical support; ntuple production
Riu, Imma	Signal AODs and TOPQ1s production; provision of other technical support from resolved analysis
Mir Martinez, Lluisa Maria	Monte Carlo production

104

105 **Remaining to do**

106 **The reweighting method:** A complete proposal is to be discussed at the EB request (HBSM meeting) on
107 21st July, and incorporate comments and discussions there for the method, summarize them in the
108 note in 1-2 weeks after the meeting.

109 **W' MC production:** Validations are to be finalized by the end of July so that the MC generator can be
110 implemented into the ATLAS official software. We aim for finishing the MC production as well as
111 limit evaluations by the end of September. This is to be done in parallel to EB review, as agreed with
112 the HBSM / HDBS conveners.

113 **Theoretical interpretation:** Interpret limits in terms of the theoretical H+/W' scenarios, such as hMSSM
114 and XXX. This will be done by the end of September.

115 **Version log with major updates:**

116 **v1.1:**

- 117 • Filled the Section 5.4 that describes the reweighting technique.
118 • Added the Figures 69(a) to 69(j) in Appendix B.2 to show BDT output distributions of events used
119 for deriving reweighting factors.
120 • Updated the Table 16 and the Section 6.4 with the systematics source of $t\bar{t}$ + jets reweighting included.
121 (The original Section 5.4 that describes the reweighting systematics sources was put into the Section
122 6.4)

123 1 Introduction

124 The discovery of a neutral boson with a measured mass around 125 GeV at the Large Hadron Collider
 125 (LHC) in 2012 [1–3] opens the question whether this is the Higgs boson of the Standard Model (SM)
 126 or part of an extended scalar sector. Indeed, charged Higgs bosons¹ are predicted in several extensions
 127 of the SM, which add a second doublet [4–7] or triplets [7–11] to its scalar sector. In CP-conserving
 128 Two-Higgs-Doublet Models (2HDMs) H^+ production and decay at tree level depend on its mass and
 129 two parameters: the mixing angle α of the neutral CP-even Higgs bosons, and the ratio of the vacuum
 130 expectation values of the two Higgs doublets ($\tan \beta$).

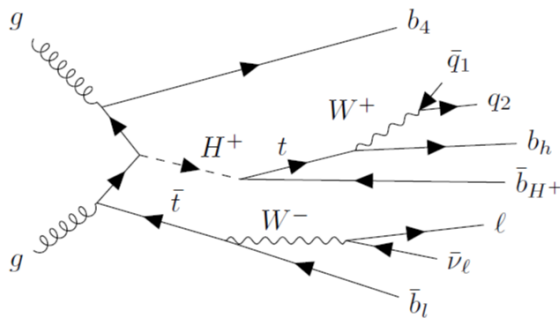


Figure 1: Feynman diagram for $pp \rightarrow tbH^+ \rightarrow tb(tb)$

131 For H^+ masses above the top-quark mass the leading production mode is $gg \rightarrow tbH^+$ and, close to the
 132 alignment limit when $\cos(\beta - \alpha) \approx 0$, the dominant decay mode is $H^+ \rightarrow tb$. For lower H^+ masses, the
 133 dominant decay mode is $H^+ \rightarrow \tau\nu$, as well as for large values of $\tan \beta$ irrespective of the charged Higgs
 134 mass. Therefore, the two decay modes naturally complement each other in searches for charged Higgs
 135 bosons.

136 The ATLAS and CMS collaborations have searched for charged Higgs bosons in pp collisions at $\sqrt{s} = 7, 8$
 137 and 13 TeV, probing the mass range below the top-quark mass in the $\tau\nu$ [12–17], cs [18, 19], and cb [20]
 138 decay modes, as well as above the top-quark mass in the $\tau\nu$ and tb decay modes [14, 16, 17, 21–27]. In
 139 addition, $H^+ \rightarrow WZ$ was searched for in the vector-boson-fusion production mode [28, 29]. No evidence for
 140 charged Higgs bosons was found in any of these searches.

141 This note presents a search for H^+ production in the $H^+ \rightarrow tb$ decay mode using pp collisions at $\sqrt{s} = 13$
 142 TeV. Events with one charged lepton ($l = e, \mu$) and jets in the final state are considered. Compared with the
 143 previous analysis using the same final state and the dataset [24] (so-called ‘resolved analysis’), boosted
 144 top tagging technique is used to identify a hadronically decaying top quark originated from the decay
 145 of the heavy H^+ . This technique allows to improve sensitivities in the high mass regions, where all top
 146 decay products are merged into a single large-R jet, and therefore cannot be reconstructed in the resolved
 147 analysis [24]. To separate signal from SM background, multivariate discriminants are employed in the
 148 regions where the signal rate is expected to be the largest. Limits on the $H^+ \rightarrow tb$ production cross-section
 149 are set by a simultaneous fit of BDT distributions.

¹ Charge-conjugate is implied elsewhere in this note.

¹⁵⁰ Furthermore, the analysis technique is extended to a search for the $W' \rightarrow tb$ decay, where W' is produced in
¹⁵¹ association with tb .

¹⁵² The analysis replies on ATLAS official background as well as requested H^+ and W' signal samples, as
¹⁵³ detailed in Section 2, with the TOPQ1 derivation. The ntuples are produced using the TTHbbAnalysis
¹⁵⁴ software package.² These ntuples are used as inputs to TRExFitter to perform statistical analysis.³

² https://gitlab.cern.ch/atlasHTop/TTHbbAnalysis/-/tree/user/hyamauch/pflow_dev_HplusBoosted

³ <https://gitlab.cern.ch/hyamauch/TRExFitter>

155 2 Data and MonteCarlo Simulated Events

156 2.1 Data Sample

157 This analysis uses pp collision data collected from 2015 to 2018 by the ATLAS detector at $\sqrt{s} = 13$ TeV.
 158 Selected events are recorded using unprescaled triggers, as detailed in Table 1. Only runs with stable
 159 colliding beams and all ATLAS subsystems operational are used. These are summarized in the Good
 160 Run Lists (GRL) shown in Table 2, together with the integrated luminosity collected each year. The total
 161 integrated luminosity is 139 fb^{-1} [30].

Year		Single-electron triggers
2015	e24_lhmedium_L1EM20VH_OR_e60_lhmedium_OR_e120_lhloose	
2016-2018	e26_lhtight_nod0_ivarloose_OR_e60_lhmedium_nod0_OR_e140_lhloose_nod0	
<hr/>		
(a)		
Year		Single-muon triggers
2015	mu20_iloose_L1MU15_OR_mu50	
2016-2018	mu26_ivarmedium_OR_mu50	
<hr/>		
(b)		

Table 1: Single-electron (a) and single-muon (b) trigger menus used depending on the year of data-taking.

Year	Luminosity (pb^{-1})	GRL
2015	3219.6	data15_13TeV/20170619/physics_25ns_21.0.19.xml
2016	32988.1	data16_13TeV/20180129/physics_25ns_21.0.19.xml
2017	44307.4	data17_13TeV/20180619/physics_25ns_Triggerno17e33prim.xml
2018	58450.1	data18_13TeV/20190318/physics_25ns_Triggerno17e33prim.xml

Table 2: Integrated luminosity for each year of data-taking, computed with the OffLumi-13TeV-010 luminosity tag [31], together with the corresponding GRLs [32].

162 2.2 Signal Samples

163 This paragraph describes MC samples used for each signal event's estimation. The summary is shown in
 164 Table 3.

Physics process	Generator	PS generator	Normalisation	PDF set
$t b H^+$ ($M_{H^+} \leq 3.0$ TeV)	MG5_aMC 2.6.2	Pythia 8.212	NLO	NNPDF2.3NLO
$t b H^+$ ($M_{H^+} = 4.0, 5.0$ TeV)	MG5_aMC 2.8.1	Pythia 8.244	NLO	NNPDF3.0NLO
$t b W'$		<i>Getting ready</i>		

Table 3: Nominal simulated signal event samples. The generator, parton shower generator and cross-section used for normalisation are shown together with the applied PDF set.

165 2.2.1 $\bar{t}bH^+$ Samples

166 The H^+ signal samples are generated with MadGraph5_aMCatNLO (MG5_aMC) [33], which is a generator
 167 based on a four-flavor scheme (4FS) next-to-leading order (NLO) in QCD [34]. The NNPDF2.3NLO
 168 [35] parton distribution function (PDF) set is used.⁴ The width of the H^+ is set to zero. Dynamic QCD
 169 factorisation and renormalisation scales (μ_f and μ_r) are set to $\frac{1}{3} \sum_i \sqrt{m(i)^2 + p_T(i)^2}$, where i runs over the
 170 final state particles (H^+ , t and b) used in the generation. The events are showered with Pythia 8.212 [37]
 171 with the A14 [38] set of underlying-event related parameters tuned to ATLAS. Ten different H^+ mass points
 172 between 1000 and 5000 GeV are generated as detailed in Table 4. The table also shows cross sections from
 173 MG5_aMC and Santander-matched cross sections for 2HDM type-II (a la MSSM), but without SUSY
 174 QCD corrections [33, 39–41]. All samples are fully simulated with the proportions of mc16a, mc16d and
 175 mc16e corresponding to the amount of data recorded in the 2015-2016, 2017 and 2018 data-taking years.

DSID	H^+ mass [GeV]	Size	$\sigma^{\text{MG5_aMC}}$ [fb]	$\sigma_{\tan \beta=1}^{\text{MSSM}}$ [fb]	$\sigma_{\tan \beta=60}^{\text{MSSM}}$ [fb]
450004	1000	1.0M	3.28	40.9	37.8
450598	1200	1.0M	1.31	16.4	15.1
450599	1400	1.0M	5.62×10^{-1}	7.1	6.5
450600	1600	1.2M	2.54×10^{-1}	3.2	3.0
450601	1800	1.3M	1.21×10^{-1}	1.5	1.4
450602	2000	1.9M	5.90×10^{-2}	0.8	0.7
451490	2500	1.9M	1.11×10^{-2}	<i>Not available</i>	
451491	3000	1.9M	2.34×10^{-3}	<i>Not available</i>	
508710	4000	1.9M	9.75×10^{-5}	<i>Not available</i>	
508711	5000	1.9M	4.28×10^{-6}	<i>Not available</i>	

Table 4: Generated H^+ samples. All samples are simulated with FullSim and available in the appropriate proportions of mc16a, mc16d and mc16e. The cross-section values for $\tan \beta = 1$ or $\tan \beta = 60$ take into account the production of H^\pm .

176 The W' sample is produced only privately at this point. In this version of the note, all information regarding
 177 W' is summarised in Section 8.

178 2.3 Background Samples

179 This paragraph describes MC samples used for each background event's estimation. The summary is shown
 180 in Table 5.

⁴ The samples with masses of 4 and 5 TeV are generated using NNPDF3.0NLO [36] PDF set.

Physics process	Generator	PS generator	Normalisation	PDF set
$t\bar{t}$ + jets	PowhegBox v2	Pythia 8.230	NNLO+NNLL	NNPDF3.0NLO
$t\bar{t}H$	PowhegBox v2	Pythia 8.230	NNLO	NNPDF3.0NLO
$t\bar{t}V$	MG5_aMC 2.3.3	Pythia 8.210	NLO	NNPDF3.0NLO
Single top t-chan.	PowhegBox v2	Pythia 8.230	aNNLO	NNPDF3.0NLOnf4
Single top s-chan.	PowhegBox v2	Pythia 8.230	aNNLO	NNPDF3.0NLO
Single top tW	PowhegBox v2	Pythia 8.230	aNNLO	NNPDF3.0NLO
$tHjb$	MG5_aMC 2.6.X	Pythia 8.230	NLO	NNPDF3.0NLOnf4
tHW	MG5_aMC 2.6.2	Pythia 8.235	NLO	NNPDF3.0NLO
tZq	MG5_aMC 2.3.3	Pythia 8.212	NLO	CTEQ6L1LO
tZW	MG5_aMC 2.3.3	Pythia 8.212	NLO	NNPDF3.0NLO
4 tops	MG5_aMC 2.3.3	Pythia 8.230	NLO	NNPDF3.1NLO
V + jets	Sherpa 2.2.1	Sherpa 2.2.1	NNLO	NNPDF3.0NLO
Diboson	Sherpa 2.2	Sherpa 2.2	NLO	NNPDF3.0NLO

Table 5: Nominal simulated background event samples. The generator, parton shower generator and cross-section used for normalisation are shown together with the applied PDF set.

2.3.1 $t\bar{t}$ +jets

The production of $t\bar{t}$ events is modeled using the PowhegBox [42–45] v2 generator, which provides matrix element (ME) at NLO in the strong coupling constant (α_S) with the NNPDF3.0NLO PDF set [36] and the h_{damp} parameter ⁵ set to $1.5m_{\text{top}}$ [46]. The functional form of μ_f and μ_r is set to the default scale $\sqrt{m_t^2 + p_{T,t}^2}$. The events are showered with Pythia 8.230 [47].

The uncertainty due to initial-state-radiation (ISR) is estimated using weights in the ME and in the parton shower (PS). To simulate higher parton radiation μ_f and μ_r are varied by a factor of 0.5 in the ME while using the *Var3c* upward variation from the A14 tune. For lower parton radiation, μ_f and μ_r varied by a factor of 2.0 while using the *Var3c* downward variation in the PS. The impact of final-state-radiation (FSR) is evaluated using PS weights which vary μ_r for QCD emission in the FSR by a factor of 0.5 and 2.0, respectively. The impact of the PS and hadronisation model is evaluated by changing the showering of the nominal PowhegBox events from Pythia to Herwig 7.04 [48, 49].

To assess the uncertainty due to the choice of the matching scheme, the Powheg sample is compared to a sample of events generated with MG5_aMC v2.6.0 and the NNPDF3.0NLO PDF set showered with Pythia 8.230. The shower starting scale has the functional form $\mu_q = H_T/2$ [50], where H_T is defined as the scalar sum of the p_T of all outgoing partons. Choice of μ_f and μ_r is the same as that for the Powheg setup.

To enhance the statistics in the phase-space relevant for this analysis, for all the samples described above, dedicated filtered samples were produced, requiring b - or c -hadrons in addition to those arising from the decays of the top quarks, as follows:

- One sample was produced with at least two additional b -hadrons with $p_T > 15$ GeV.

⁵ The h_{damp} parameter controls the transverse momentum of the first additional emission beyond the LO Feynman diagram in the parton shower and therefore regulates the high- p_T emission against which the $t\bar{t}$ system recoils.

- 201 • One sample was produced with at least one additional b -hadron with $p_T > 5$ GeV and failing the
 202 previous requirement.
- 203 • One sample was produced with at least one additional c -hadron with $p_T > 15$ GeV and failing the
 204 previous two requirements.

205 The combined use of the unfiltered and filtered samples is done by assuring no overlap between them (by
 206 the use of the heavy flavour filter flag, *TopHeavyFlavorFilterFlag*) and weighted with the appropriate
 207 cross-section and filter efficiencies.

208 2.3.2 $t\bar{t}H$

209 The production of $t\bar{t}H$ events is modeled in the 5F scheme using PowhegBox [51] at NLO in α_S with
 210 the NNPDF3.0NLO PDF set. The h_{damp} parameter is set to $3/4 \times (m_t + m_{\bar{t}} + m_H) = 352.5$ GeV. The
 211 events are showered with Pythia 8.230. The uncertainties due to ISR, FSR, PS and hadronisation model,
 212 as well as that due to the matching scheme, are evaluated with the same procedures used for the $t\bar{t}$ + jets
 213 background.

214 2.3.3 $t\bar{t}V$

215 The production of $t\bar{t}V$ events is modeled using the MG5_aMC v2.3.3 generator, which provides ME at
 216 NLO in α_S with the NNPDF3.0NLO PDF set. The functional form of μ_f and μ_r is set to the default scale
 217 $0.5 \times \sum_i \sqrt{m_i^2 + p_{T,i}^2}$ where the sum runs over all the particles generated from the ME calculation. The
 218 events are showered with Pythia 8.210.

219 Additional $t\bar{t}V$ samples are produced with Sherpa 2.2.0 [52] at LO accuracy, using the MEPS@LO setup
 220 [53, 54] with up to one additional parton for the $t\bar{t}V$ sample and two additional partons for the others. A
 221 dynamic μ_r is used, defined similarly to that of the nominal MG5_aMC+Pythia samples. The CKKW
 222 matching scale of the additional emissions is set to 30 GeV. The default Sherpa 2.2.0 PS is used along with
 223 the NNPDF3.0NNLO PDF set.

224 2.3.4 Single top

225 t -channel

226 Single-top t -channel production is modeled using the PowhegBox v2 generator, which provides ME
 227 at NLO in α_S in the 4F scheme with the NNPDF3.0NLOnf4 PDF set. The functional form of μ_f and
 228 μ_r is set to $\sqrt{m_b^2 + p_{T,b}^2}$, following the recommendation of Ref. [55]. The events are showered with
 229 Pythia 8.230.

230 The impact of the PS and hadronisation model is evaluated by comparing the nominal generator
 231 setup with a sample produced with the PowhegBox v2 generator at NLO in QCD in the 4FS using
 232 the NNPDF3.0NLOnf4 PDF set. The same events produced for the nominal PowhegBox+Pythia8
 233 sample are used. The events are showered with Herwig 7.04.

234 To assess the uncertainty due to the choice of the matching scheme, the nominal sample is compared
 235 to a sample generated with the MG5_aMC v2.6.2 generator at NLO in QCD in the 4FS, using the
 236 NNPDF3.0NLOnf4 PDF set. Top quarks are decayed at LO using MadSpin [56, 57] to preserve all
 237 spin correlations. The events are showered with Pythia 8.230.

238 **s-channel**

239 Single-top *s*-channel production is modeled using the PowhegBox v2 generator, which provides ME
 240 at NLO in α_S in the 5F scheme with the NNPDF3.0NLO PDF set. The functional form of μ_f and μ_r
 241 is set to the default scale, which is equal to the top quark mass. The events are showered with Pythia
 242 8.230.

243 The impact of the PS and hadronisation model is evaluated by comparing the nominal generator
 244 setup with a sample produced with the PowhegBox v2 generator at NLO in QCD in the 5FS using the
 245 NNPDF3.0NLO PDF set. The same events produced for the nominal PowhegBox+Pythia8 sample
 246 are used. The events are showered with Herwig 7.04.

247 To assess the uncertainty due to choice of the matching scheme, the nominal sample is compared
 248 to a sample generated with the MG5_aMC v2.6.2 generator at NLO in QCD in the 5FS, using
 249 the NNPDF3.0NLO PDF set. Top quarks are decayed at LO using MadSpin to preserve all spin
 250 correlations. The events are showered with Pythia 8.230.

251 ***tW***

252 Single-top *tW* associated production is modeled using the PowhegBox v2 generator, which provides ME
 253 at NLO in α_S in the 5F scheme with the NNPDF3.0NLO PDF set. The functional form of μ_f
 254 and μ_r is set to the default scale, which is equal to the top quark mass. The diagram removal scheme
 255 [58] is employed to handle the interference with $t\bar{t}$ production [46]. The events are showered with
 256 Pythia 8.230.

257 The nominal Powheg+Pythia8 sample is compared to an alternative sample generated using the
 258 diagram subtraction scheme [46, 58] to estimate the uncertainty due to the interference with $t\bar{t}$
 259 production.

260 The impact of the PS and hadronisation model is evaluated by comparing the nominal generator
 261 setup with a sample produced with the Powheg v2 generator at NLO in QCD in the 5FS using the
 262 NNPDF3.0NLO PDF set. The same events produced for the nominal Powheg+Pythia8 sample are
 263 used. The events are showered with Herwig 7.04.

264 To assess the uncertainty due to the choice of the matching scheme, the nominal sample is compared
 265 to a sample generated with the MG5_aMC v2.6.2 generator at NLO in QCD in the 5FS, using the
 266 NNPDF2.3NLO PDF set. The events are showered with Pythia 8.230.

267 **2.3.5 *tH***

268 ***tHjb* production**

269 The production of *tHjb* events is modeled in the 4F scheme using the MG5_aMCv2.6.0 with
 270 the NNPDF3.0NLOnf4 PDF set. The functional form of μ_f and μ_r is set to the default scale
 271 $1/2 \times \sum_i \sqrt{m_i^2 + p_{T,i}^2}$, where the sum runs over all the particles generated from the ME calculation.

272 The shower starting scale has the functional form $\mu_q = H_T/2$, where H_T is defined as the scalar sum
 273 of the p_T of all outgoing partons. The events are showered with Pythia 8.230.

274 ***tHW* production**

275 The production of *tHW* events is modeled in the 5F scheme using the MG5_aMCv2.6.2 with the
 276 NNPDF3.0NLO PDF set. The functional form μ_f and μ_r is set to the default scale $1/2 \times \sum_i \sqrt{m_i^2 + p_{T,i}^2}$
 277 where the sum runs over all the particles generated from the ME calculation. The shower starting
 278 scale has the functional form $\mu_q = H_T/2$, where H_T is defined as the scalar sum of the p_T of all
 279 outgoing partons. The events are showered with Pythia 8.235.

280 **2.3.6 Rare *t* processes**

281 ***tZq***

282 The *tZq* MC samples [59] are generated at LO in α_S using MG5_aMC 2.3.3 in the 4F scheme,
 283 with the CTEQ6L1 [60] LO PDF set. Following the recommendations taken from Ref. [55], the
 284 renormalisation and factorisation scales are set to $4 \times \sum_b \sqrt{m_i^2 + p_{T,b}^2}$, where the *b*-quark is the one
 285 coming from the gluon splitting. The events are showered with Pythia 8.212.

286 ***tZW***

287 The *tZW* sample is simulated using the MG5_aMC v2.3.3 generator at NLO in α_S with the
 288 NNPDF3.0NLO PDF set. The top quark is decayed inclusively while the *Z* boson decays to a pair of
 289 leptons, by means of Pythia 8.212. The 5F scheme is used where all the quark masses are set to zero,
 290 except for the top quark. μ_f and μ_r are set to the top quark mass. The DR1 scheme [58] is employed
 291 to handle the interference between *tWZ* and *ttZ*, and is applied to the *tWZ* sample.

292 **4 tops**

293 The production of 4 tops events is modeled using the MG5_aMC v2.3.3 generator, which provides
 294 ME at NLO in α_S with the NNPDF3.1NLO PDF set. The functional form of μ_f and μ_r is set to
 295 $0.25 \times \sum_i \sqrt{m_i^2 + p_{T,i}^2}$, where the sum runs over all the particles generated from the ME calculation,
 296 following the Ref.[61]. The events are showered with Pythia 8.230.

297 **2.3.7 Vector bosons plus jets**

298 QCD vector bosons plus jets production is simulated with the Sherpa v2.2.1 PS Monte Carlo generator. In
 299 this setup, NLO-accurate ME for up to two jets, and LO-accurate ME for up to four jets are calculated with
 300 the Comix [62] and OpenLoops [63, 64] libraries. The default Sherpa PS [65] based on Catani-Seymour
 301 dipoles and the cluster hadronisation model [66] are used. They employ the dedicated set of tuned
 302 parameters developed by the Sherpa authors for this version based on the NNPDF3.0nnlo set. The NLO ME
 303 of a given jet-multiplicity are matched to the PS using a colour-exact variant of the MC@NLO algorithm
 304 [67]. Different jet multiplicities are then merged into an inclusive sample using an improved CKKW
 305 matching procedure [53, 54], which is extended to NLO accuracy using the MEPS@NLO prescription
 306 [68]. The merging cut is set to $Q_{\text{cut}} = 20$ GeV.

307 QCD scale uncertainties are evaluated on-the-fly [69] using 7-point variations of μ_f and μ_r in the ME. The
 308 scales are varied independently by factors of 0.5 and 2 but avoiding opposite factors. PDF uncertainties for
 309 the nominal PDF set are evaluated using the 100 variation replicas, as well as ± 0.001 shifts of α_S .

310 2.3.8 Dibosons

311 Diboson samples are simulated with the Sherpa v2.2 generator. In this setup multiple ME are matched
312 and merged with the Sherpa PS based on Catani-Seymour dipole using the MEPS@NLO prescription.
313 For semileptonically and fully leptonically decaying diboson samples, as well as loop-induced diboson
314 samples, the virtual QCD correction for ME at NLO accuracy are provided by the OpenLoops library.
315 For electroweak $VVjj$ production, the calculation is performed in the G_μ scheme, ensuring an optimal
316 description of pure electroweak interactions at the electroweak scale. All samples are generated using
317 the NNPDF3.0nnlo set, along with the dedicated set of tuned PS parameters developed by the Sherpa
318 authors.

319 3 Object Reconstruction

320 3.1 Electrons

321 Electrons are reconstructed from energy clusters in the electromagnetic calorimeter matched to tracks
 322 reconstructed in the inner detector (ID) [70, 71], and are required to have $p_T > 10$ GeV and $|\eta| < 2.47$.
 323 Candidates in the barrel–endcap transition region of the calorimeter ($1.37 < |\eta| < 1.52$) are excluded.
 324 Electrons must satisfy the *tight* identification criterion based on a likelihood discriminant described in
 325 Ref. [71] and the following constraints in the longitudinal and transverse impact parameters: $|z_0| < 0.5$ mm
 326 and $|d_0|/\sigma_{d_0} < 5$. The impact parameters are defined with respect to beam line. Electrons are required to
 327 satisfy the *FCTight* isolate criteria [72].

328 3.2 Muons

329 Muons are reconstructed from either track segments or full tracks in the muon spectrometer which are
 330 matched to tracks in the ID [73]. Tracks are then re-fitted using information from both detector system.
 331 Muons are required to have $p_T > 10$ GeV and $|\eta| < 2.5$ and the following constraints in the longitudinal
 332 and transverse impact parameters: $|z_0| < 0.5$ mm and $|d_0|/\sigma_{d_0} < 3$. Muons should satisfy the *medium*
 333 identification and the *FCTightTrackOnly* isolation criteria [72].

334 3.3 Taus

335 Hadronically decaying tau leptons (τ_{had}) are distinguished from jets using the track multiplicity and the
 336 τ_{had} identification algorithm based on a recurrent neural network [74]. This algorithm exploits the track
 337 collimation, jet substructure, kinematic information and so son. These τ_{had} candidates are required to have
 338 $p_T > 25$ GeV, $|\eta| < 2.5$ and pass the *Medium τ* -identification working point. Although taus are not used in
 339 the analysis, the consistent configuration with the resolved analysis as well as the $t\bar{t}H(\rightarrow bb)$ analysis is
 340 kept.

341 3.4 Small- R jets and b -tagging

342 Jets are reconstructed using the anti- k_t clustering algorithm [75] on particle-flow objects [76] with a radius
 343 of $R = 0.4$. Jets are calibrated using the standard jet calibration procedure, which corrects the jet energy to
 344 match on average the true jet energy at particle level and applies an in-situ correction for data [77]. The
 345 jet collection name in ATLAS is `AntiKt4EMPF1lowJets_BTagging201903`. Jets are required to have
 346 $|\eta| < 2.5$ such that they are within the acceptance of the ID and the recommended jet vertex tagging (JVT)
 347 requirement [78] is applied to jets with $p_T < 60$ GeV in order to remove jets originating from pile-up.

348 Small- R jets originating from the hadronisation of b -quarks (referred to as b -jets hereafter) are identified
 349 using an algorithm based on multivariate techniques to combine information from the impact parameters
 350 of displaced tracks as well as properties of secondary and tertiary decay vertices reconstructed within the
 351 jets. In this analysis, b -tagging relies on the *DL1r* tagger [79], trained on simulated $t\bar{t}$ events, and the event
 352 selection makes use of jets b -tagged with the *DL1r* algorithm at the 70% efficiency working point.

353 3.5 Large- R jets and top-tagging

354 Top quarks with high transverse momentum ($p_T \gtrsim 2m_t$) are expected to result in decay products that are
 355 collimated. For top quarks decaying hadronically (bqq'), the three quarks may not be resolved as three
 356 separate jets. In order to reconstruct these boosted hadronically-decaying top quarks, large-radius (large- R)
 357 jets are used. The large- R jets are formed from the topological clusters of calorimeter cells which are
 358 calibrated to the hadronic energy scale using the local calibration weighting method [80], and reconstructed
 359 using the anti- k_t algorithm with radius parameter of $R = 1.0$. The jet collection name in ATLAS is
 360 `AntiKt10LCTopoTrimmedPtFrac5SmallR20Jets`. These jets are further trimmed to remove the effects
 361 of pile-up and underlying event. The trimming [81] is done by reclustering the original constituents of a
 362 large- R jet into a collection of R_{sub} subjets using k_t algorithm [82]. The subjets are then discarded if they
 363 carry less than a specific fraction (f_{cut}) of the p_T of the original large- R jet. In this analysis, the optimized
 364 values ($R_{\text{sub}} = 0.2$, $f_{\text{cut}} = 5\%$) are used [83]. The large- R jet energy and mass scale are then calibrated
 365 using correction factors derived from simulation. The mass of the large- R jets is calculated using tracking
 366 and calorimeter information, so called combined mass technique [84]. Only the large- R jets that satisfy
 367 $200 < p_T < 3000 \text{ GeV}$, $|\eta| < 2.0$ and $40 < m_{\text{comb}} < 600 \text{ GeV}$ are considered in this analysis.

368 The identification of hadronically decaying top quarks that are reconstructed as large- R jets is performed
 369 using a multivariate classification algorithm employed in a deep neural network [85]. In the kinematic
 370 region of interest in this search, a single large- R jet captures the top quark decay products, resulting in a
 371 characteristic multi-core structure within the jet, in contrast to a typical single-core structure associated
 372 with jets in multijet. In order to exploit this characteristic behaviour for the top quark identification, a
 373 multivariate top-tagging classifier was developed. The tagger uses multiple jet-level discriminants as
 374 inputs, such as calibrated jet p_T and mass, information about the dispersion of the jet constituents such as
 375 N -subjettiness [86], splitting scales [87] and energy correlation functions [88].

376 Top-tagging, associated scale factors and uncertainties are only provided for jets with $350 < p_T < 2500$
 377 GeV. The tagger used is optimized for the contained top definition, in which the signal category is defined
 378 using jets matched to a truth top quark. In addition, a truth jet matched to the reconstructed jet is required
 379 to have a mass above 140 GeV and at least one b -hadron ghost matched to it.

380 In this analysis, large- R jets which pass the 80% efficiency working point of the contained top-tagging
 381 criterion ($J_{\text{top-tagged}}$) are chosen as the boosted top candidates. Especially, the leading boosted top candidate
 382 out of them is represented by $J_{\text{top-tagged}}^{\text{1st}}$ in the following sections.

383 3.6 Overlap Removal

384 In order to avoid counting a single detector response as more than one lepton or jet, the following overlap
 385 removal procedure is applied.

386 To prevent double-counting of electron energy deposits as jets, the small- R jet within $\Delta R_y = \sqrt{(\Delta y)^2 + (\Delta \phi)^2} =$
 387 0.2 of a selected electron is removed. Here, the rapidity is defined as $y = \frac{1}{2} \ln \frac{E+p_z}{E-p_z}$, where E is the energy
 388 and p_z is the longitudinal component of the momentum along the beam pipe. If the nearest small- R jet

surviving that selection is within $\Delta R_y = 0.4$ of the electron, the electron is discarded. In the case that a large- R jet is found within $\Delta R = 1.0$ of the electron, the large- R jet is removed.⁶

Muons are removed if their distance from the nearest small- R jet is within $\Delta R_y < 0.4$. This treatment reduces the background from heavy-flavor decays inside small- R jets. However, if this small- R jet has fewer than three associated tracks, the muon is kept and the small- R jet is removed instead. This avoids an inefficiency for high-energy muons undergoing significant energy loss in the calorimeter.

A τ_{had} candidate is rejected if it is within $\Delta R_y < 0.2$ from any selected electron or muon. Also, small- R jets with $\Delta R_y < 0.2$ around a τ_{had} candidate are rejected. The overlap removal with τ_{had} is applied in order to keep consistency with the $t\bar{t}H(\rightarrow bb)$ analysis as well as the $H^+ \rightarrow tb$ analysis.

Small- R jets within $\Delta R < 1.0$ of a leading top-tagged large- R jet are removed⁶ to prevent double-counting of jet energy deposits.

All of the above overlap removal procedures are summarized in Table 6.

Reject	Against	Criteria
Small- R jet	Electron	$\Delta R_y < 0.2$
Electron	Small- R jet	$0.2 < \Delta R_y < 0.4$
Small- R jet	Muon	$N_{\text{track}} < 3$ in jet and $\Delta R_y < 0.4$
Muon	Small- R jet	$\Delta R_y < 0.4$
τ_{had}	Electron	$\Delta R_y < 0.2$
τ_{had}	Muon	$\Delta R_y < 0.2$
Small- R jet	τ_{had}	$\Delta R_y < 0.2$
Large- R jet	Electron	$\Delta R < 1.0$
Small- R jet	Leading top-tagged large- R jet	$\Delta R < 1.0$

Table 6: Summary of overlap removal procedures in this analysis.

⁶ Following the recommendation for ATLAS analyses in Run 2 [89], the overlap removal implemented in the *AssociationUtils* package [90] is based on ΔR_y . It is found more appropriate in the case of non-massless objects [91]. However, overlap removal for large- R jets is performed in the ttHOffline software, and is computed based on ΔR .

4 Analysis Strategy

4.1 Event Selection

In this analysis, two regions, “Signal region (SR)” and “Control region (CR)”, are defined according to the number of lepton, top tagged large- R jets and b -tagged small- R jets as following.

4.1.1 Signal region (SR)

Figure 2 show the schematic of boosted event topology in case of $H^+ \rightarrow tb$ event. An signal event is expected to have one $J_{\text{top-tag}}$, three b -jets and one lepton+MET. However, the b -jet originated from the gluon is typically not detected, because it tend to fly in the forward directions and therefore outside the detector acceptance. Therefore, at least two b -jets are required in this analysis.

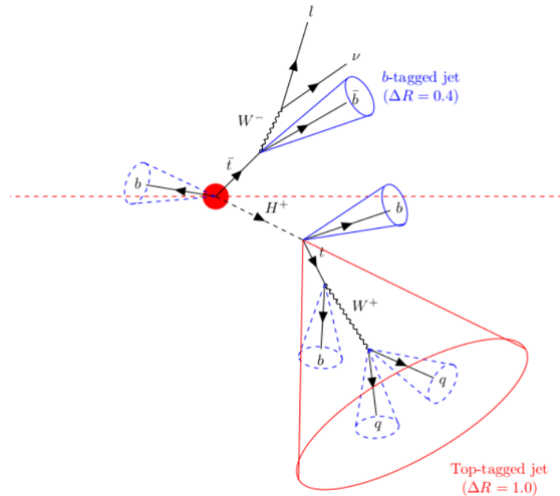


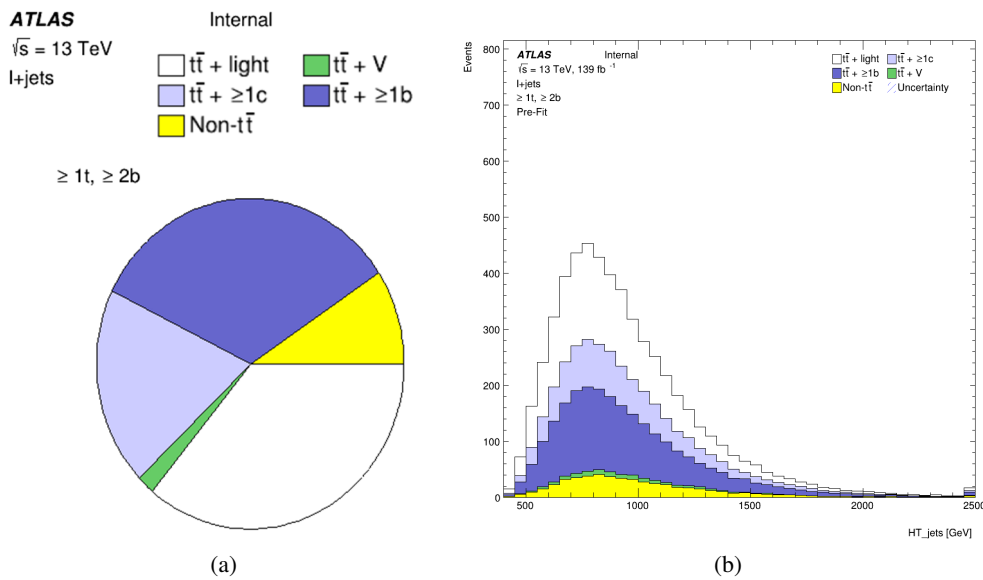
Figure 2: Feynman diagram (a) and schematic of boosted event topology (b). Signal event has at least one $J_{\text{top-tag}}$ and at least two b -tagged small- R jets.

To be consistent with the signal event as shown in Figure ??, events are required to have exactly one lepton (e or μ) that is matched to the one firing one of the single lepton triggers. Events are also required to have at least one top-tagged large- R jet and at least two b -tagged small- R jets. The b -jets must additionally satisfy $\Delta R(J_{\text{top-tag}}^{1st}, b\text{-jet}) > 1.0$ to ensure these b -jets are not constituent of the leading top-tagged jet. Missing E_T is not required in this analysis. These selections are summarized in Table 7.

Cut	Criteria
leptons	Exactly 1 lepton in event
	<u>Electron</u> <u>Muon</u>
	$p_T > 27 \text{ GeV}$ $p_T > 27 \text{ GeV}$
	$ \eta < 1.37 \text{ or } 1.52 < \eta < 2.47$ $ \eta < 2.5$
Top-tagged large- R jets	≥ 1 top-tagged large-R jets
	$350 \text{ GeV} < p_T < 2500 \text{ GeV}$
	$ \eta < 2.0$
b -tagged small- R jets	≥ 2 b-tagged small-R jets
	$p_T > 25 \text{ GeV}$
	$ \eta < 2.5$
	$\Delta R(J_{\text{top-tag}}^{1\text{st}}, b\text{-jet}) > 1.0$

Table 7: Event selections in the SR.

Events passing the event selections in Table 7 are expected to have the boosted-topology as shown in Figure ???. The expected background composition and distributions in the SR is illustrated in Figure 3. Events containing $t\bar{t}$ fully dominate the SR. In this figure, H_T^{jet} denotes the sum of p_T of $J_{\text{top-tag}}^{1\text{st}}$ and all small- R jets in event, and enhances the characteristics of the signal events which have high p_T jets from the heavy H^+ decay. Table ?? shows the cut flow for each signal sample.

Figure 3: Background composition in the SR is shown in the pie chart (a) and the H_T^{jet} distributions (b).

4.1.2 Control region (CR)

In order to constrain the yields of events with $t\bar{t}$ in association with at least one light-flavor jet, a dedicated control region (CR) is prepared. Requirements in the CR are identical to that in the SR, except the number of b -tagged small- R jets. Exactly one b -tagged small- R jet is required in the CR in order to keep orthogonality

424 to the SR where two or more b -tagged small- R jets are required. The selections in the CR are summarized
 425 in Table 8.

Cut	Criteria
leptons	Same as in the SR
Top-tagged large- R jets	Same as in the SR
b -tagged small- R jets	Exactly one b -tagged small- R jet Other kinematic requirements are the same as in the SR

Table 8: Event selections in the CR.

426 After applying the event selections for the CR, the events mostly contain $t\bar{t}$ in association with at least one
 427 light-flavor jet. The background composition is illustrated in Figure 4. This CR is included in the profile
 428 likelihood fit discussed in Section 7.

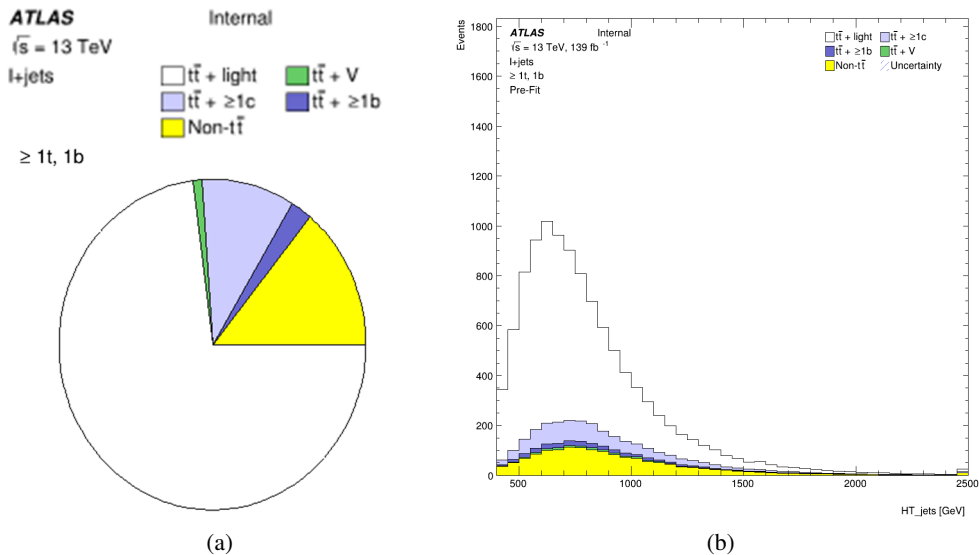


Figure 4: Background composition in the CR is shown in the pie chart (a) and the H_T^{jets} distributions (b).

429 4.1.3 Summary

430 The number of expected signal and background events in the SR and CR are shown in Table 9.
 431 The predicted number of H^+ signal events for the 1000 and 3000 GeV mass hypothesis assume
 432 $\sigma(pp \rightarrow tbH^+) \times Br(H^+ \rightarrow tb) = 0.046\text{pb}$. This is the upper limit at $M_{H^+} = 1000$ GeV obtained from
 433 the resolved analysis, the largest upper limit from the resolved analysis in the mass range $1000 \geq M_{H^+} \geq 2000$
 434 GeV where both resolved and our boosted analyses search for H^+ . We use the signal $\sigma \times Br$ in the decision
 435 of blinded regions.

	SR	CR
$t\bar{t}$ + light	1979 ± 89	7848 ± 329
$t\bar{t}+ \geq 1c$	1070 ± 56	1052 ± 38
$t\bar{t}+ \geq 1b$	1840 ± 84	246 ± 11
$t\bar{t} + W$	38 ± 20	52 ± 27
$t\bar{t} + Z$	67 ± 34	49 ± 6
Wt channel	183 ± 93	422 ± 212
t channel	37 ± 3	63 ± 5
Other top sources	38 ± 15	11 ± 1
$VV, V+jets$	152 ± 55	1001 ± 342
$t\bar{t}H$	103 ± 4	18 ± 0
Total	5565 ± 256	10763 ± 566
H^+ 1000 GeV	58 ± 6	4 ± 0
H^+ 3000 GeV	67 ± 16	13 ± 3

Table 9: Number of expected and selected events split according to the analysis region. The quoted uncertainties include both statistical and systematic uncertainties before fitting.

436 4.2 Multivariable analysis using BDT

437 In this search, the most important background is $t\bar{t}$ + jets as discussed in Section 4.1.1. To enhance
 438 separation between signal and background, multivariable analysis is performed using Boosted Decision
 439 Trees (BDT) technique of TMVA [92]. Obtained BDT score distribution is used in the profile likelihood fit
 440 as a final discriminant (Section 7).

441 4.2.1 Signal and background definition in BDT training

442 To classify H^+ signal and $t\bar{t}$ + jets background events, BDTs are trained using the simulated H^+ signal and
 443 $t\bar{t}$ + jets background samples, as summarized in Table 10. Ten different H^+ mass hypotheses are considered
 444 in this analysis, and the training is performed on each H^+ mass hypothesis. On the other hand, the $t\bar{t}$ + jets
 445 background samples are common in each training. Since kinematics of H^+ signals become harder in higher
 446 mass hypotheses, as shown in Section 4.2.3, the BDTs trained using the higher H^+ mass samples typically
 447 have greater separation power.

H^+ mass point [GeV]	DSIDs
1000	450004
1200	450598
1400	450599
1600	450600
1800	450601
2000	450602
2500	451490
3000	451491
4000	508710
5000	508711

(a)

$t\bar{t} + \text{jets}$ sample type	DSIDs
Inclusive	410470, 410471
BBFilter	411073, 411076
BFilterBBVeto	411074, 411077
CFilterBVeto	411075, 411078

(b)

Table 10: List of signal (a) and background (b) samples used in BDT training. Training is performed on each H^+ mass hypothesis. On the other hand, the $t\bar{t} + \text{jets}$ background samples are common in each training.

4.2.2 BDT training settings

In order to make full use of statistics of simulation samples, we adopt the 4-fold cross-validation method in the BDT training (Figure 5). Each simulation sample is divided into four sub-datasets (Fold1, Fold2, Fold3 and Fold4). For each MC event, a random number is generated with the MC event number as a seed, and the event is categorized into one of the sub-datasets according to the generated number. Two of the four sub-datasets are labeled "TRAIN", which are used for BDT training. One of the other sub-datasets are labeled "VALID", and is used to optimize the BDT performance. The last sample, "TEST", is used to construct a fit template. Four combination of sub-dataset usage (Split1 to Split4 in Figure 4) are tried, and we obtain four statistically-independent BDTs and fit templates. They are combined into one fit template and is used in the profile likelihood fit (Section 7).

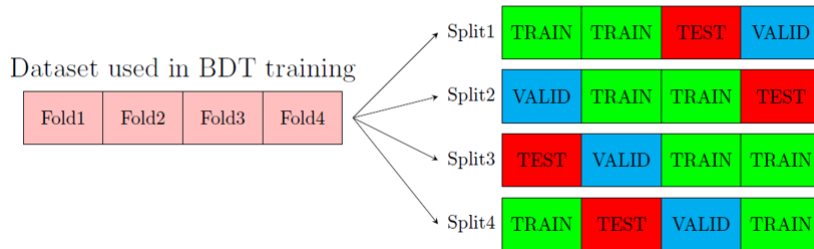


Figure 5: Scheme of 4-fold cross-validation in this analysis.

⁴⁵⁸ Hyperparamerters for the BDTs are summarized in Table. 11. Those hyperparameters are chosen to obtain
⁴⁵⁹ the best sensitivity.

Configuration	
Algorithm	Gradient boosting
<i>Hyperparameters</i>	
NTrees	100
MinNodeSize	2.5
MaxDepth	3
nCuts	20

Table 11: List of hyperparameters used in the trainging of a BDT

⁴⁶⁰ 4.2.3 Input variables in BDT

⁴⁶¹ Jets originating from an H^+ decay have higher p_T comparing with $t\bar{t} + \text{jets}$ events due to its heavy mass.
⁴⁶² Additionally, correlation among jets are different between H^+ and $t\bar{t} + \text{jets}$ events because H^+ creates a
⁴⁶³ resonance. The BDT is trained in order to fully exploit these kinematic characteristics. List of variables
⁴⁶⁴ used in BDT training is summarized in Table 12. Any variables for missing E_T are not used in BDT traning.
⁴⁶⁵ In Figure 6, each distribution in the H^+ sample with a mass of 3000 GeV is compared with the $t\bar{t} + \text{jets}$
⁴⁶⁶ background. Table 13 shows the ranking of these variables.

Symbol	Description
HT_jets	Scalar sum of the transverse energy of all jets
LeadingJet_pt	Leading jet p_T
Mjjj_MaxPt	Invariant mass of the jet triplet with maximum p_T
Mbb_MaxPt	Invariant mass of the b-jet pair with maximum p_T
Muu_MinR	Invariant mass of the untagged jet-pair with minimum ΔR
dRlepb_MindR	ΔR between the lepton and the pair of b -jets with smallest ΔR
dRbb_avg	Average ΔR between all b -jet pairs in the event
Centrality_all	Centrality calculated using all jets and leptons
H1_all	Second Fox-Wolfram moment calculated using all jets and leptons
LeadingTop_pt	Leading top-tagged jet p_T
LeadingTop_m	Invariant mass of leading top-tagged jet
Pt_tb	p_T of the pair of leading top-tagged jet and leading b -jet
M_tb	Invariant mass of the pair of leading top-tagged jet and leading b -jet
PtAsymm_tb	p_T asymmetry between leading top-tagged jet and leading b -jet

Table 12: List of variables included in the training of the BDT

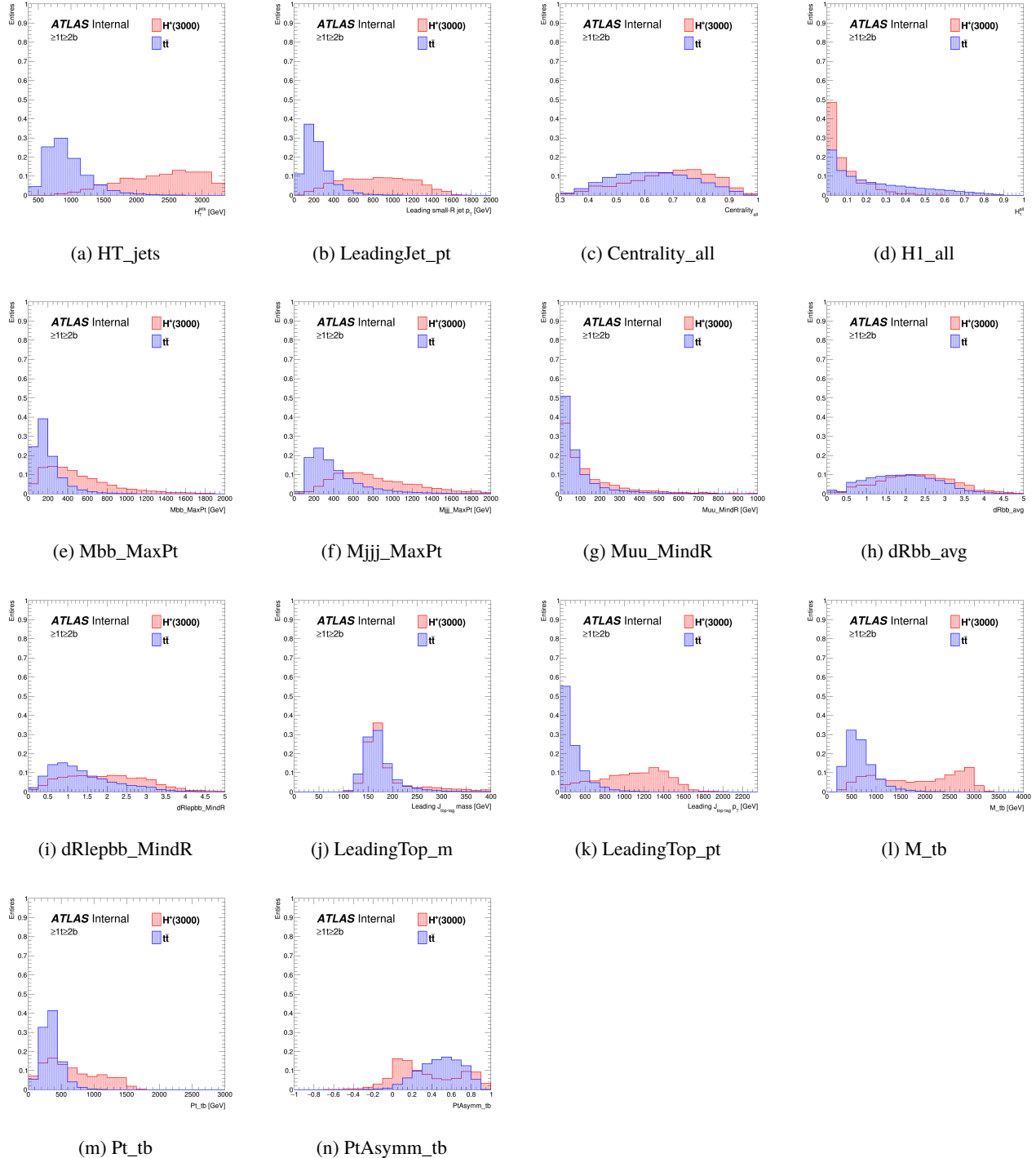


Figure 6: Comparison of input variables for BDT training between H^+ and $t\bar{t} + \text{jets}$ events under 3000 GeV H^+ mass hypothesis.

Ranking	Variable	Importance				Avg.
		Fold1	Fold2	Fold3	Fold4	
1	HT_jets	9.509E-02	1.118E-01	1.216E-01	1.073E-01	1.089E-01
2	Centrality_all	1.053E-01	9.995E-02	1.126E-01	1.012E-01	1.048E-01
3	M_tb	9.192E-02	9.473E-02	8.282E-02	8.014E-02	8.740E-02
4	LeadingTop_pt	8.710E-02	8.107E-02	6.472E-02	7.292E-02	7.645E-02
5	Pt_tb	7.944E-02	7.816E-02	7.888E-02	6.795E-02	7.611E-02
6	LeadingJet_pt	6.180E-02	7.860E-02	6.628E-02	7.577E-02	7.061E-02
7	dRlepb_MindR	6.997E-02	7.842E-02	6.968E-02	6.393E-02	7.050E-02
8	dRbb_avg	6.236E-02	6.435E-02	5.331E-02	7.843E-02	6.461E-02
9	Mbb_MaxPt	5.348E-02	6.657E-02	7.339E-02	5.552E-02	6.224E-02
10	PtAsymm_tb	5.209E-02	6.526E-02	5.843E-02	6.620E-02	6.050E-02
11	Mjjj_MaxPt	6.439E-02	6.248E-02	5.503E-02	5.577E-02	5.942E-02
12	H1_all	6.316E-02	4.577E-02	4.876E-02	6.291E-02	5.515E-02
13	LeadingTop_m	5.868E-02	3.864E-02	5.567E-02	5.748E-02	5.262E-02
14	Muu_MindR	4.438E-02	3.422E-02	5.889E-02	5.439E-02	4.797E-02

Table 13: Importance ranking of variables used in BDT training on 3000 GeV H^+ mass hypothesis. Importance values are output from TMVA.

4.2.4 Results of BDT training

The BDT output distributions for signal and background in the analysis region for different values of the H^+ mass are shown in Figure 7 to 14, together with receiver operating characteristic (ROC) curves.

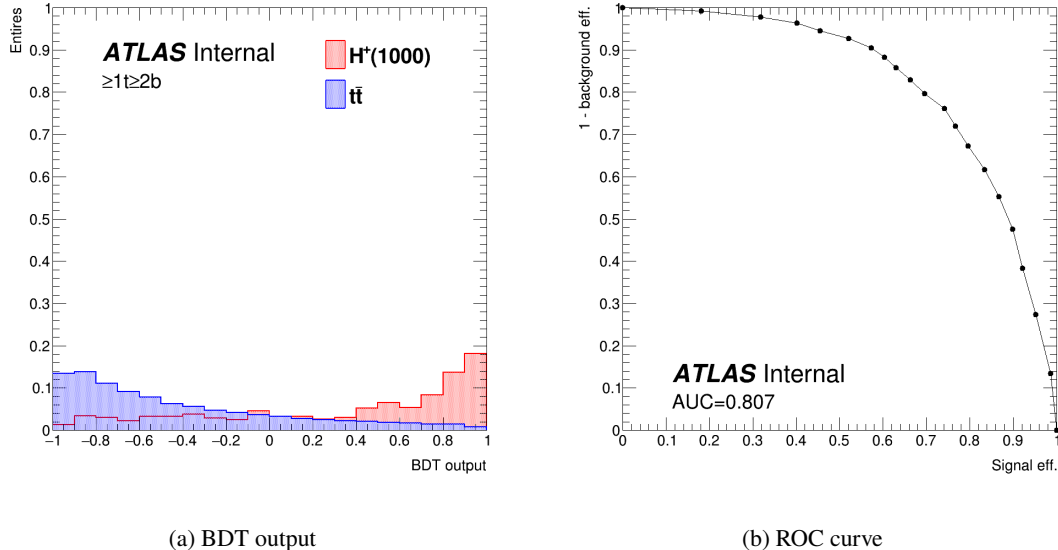


Figure 7: BDT distribution and ROC curve for the 1000 GeV H^+ mass hypothesis.

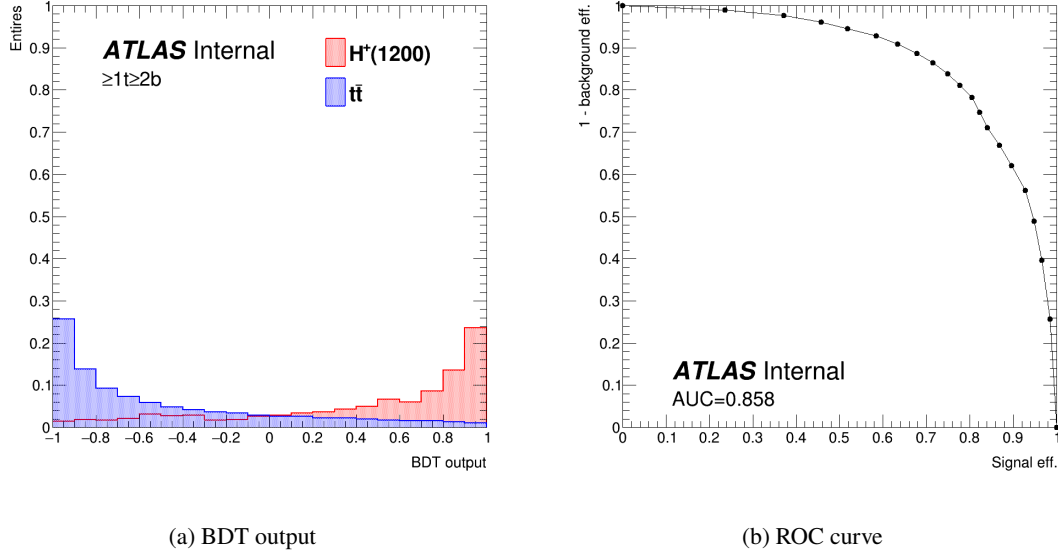


Figure 8: BDT distribution and ROC curve for the 1200 GeV H^+ mass hypothesis.

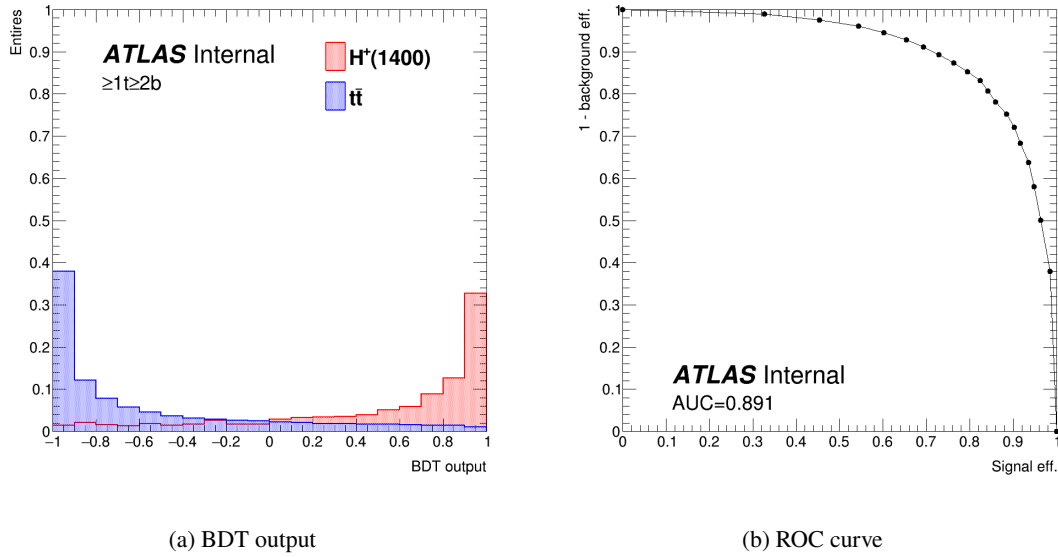


Figure 9: BDT distribution and ROC curve for the 1400 GeV H^+ mass hypothesis.

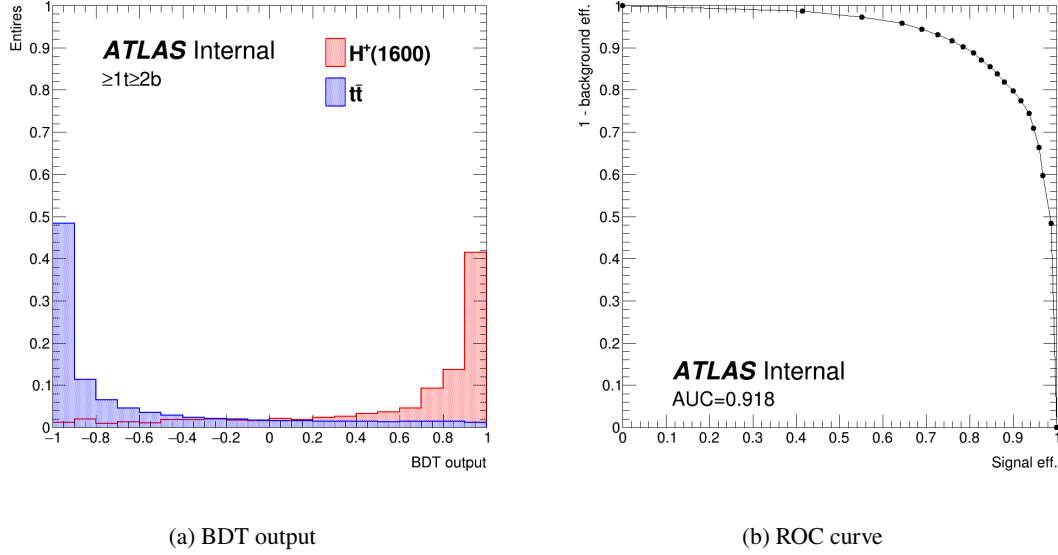


Figure 10: BDT distribution and ROC curve for the 1600 GeV H^+ mass hypothesis.

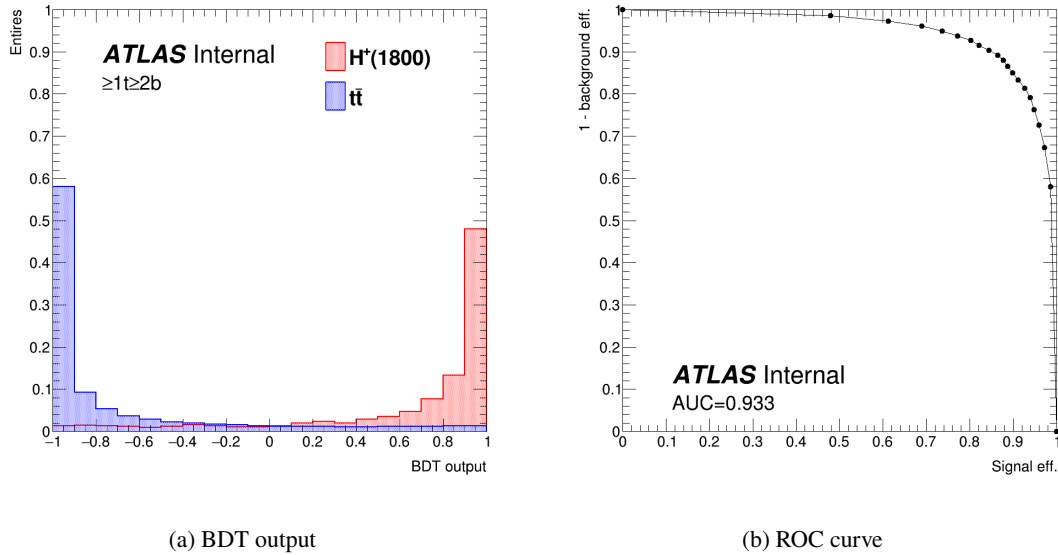


Figure 11: BDT distribution and ROC curve for the 1800 GeV H^+ mass hypothesis.

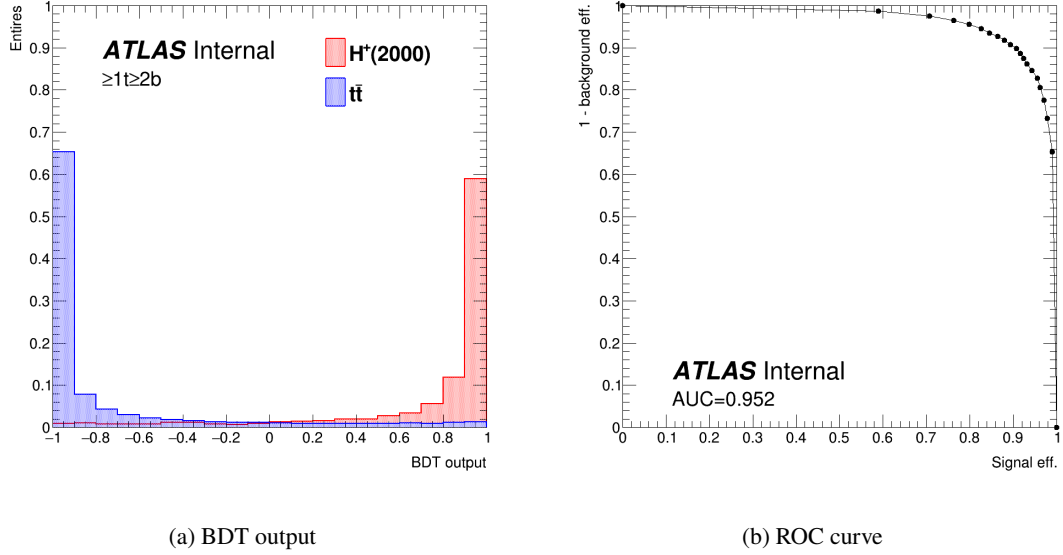


Figure 12: BDT distribution and ROC curve for the 2000 GeV H^+ mass hypothesis.

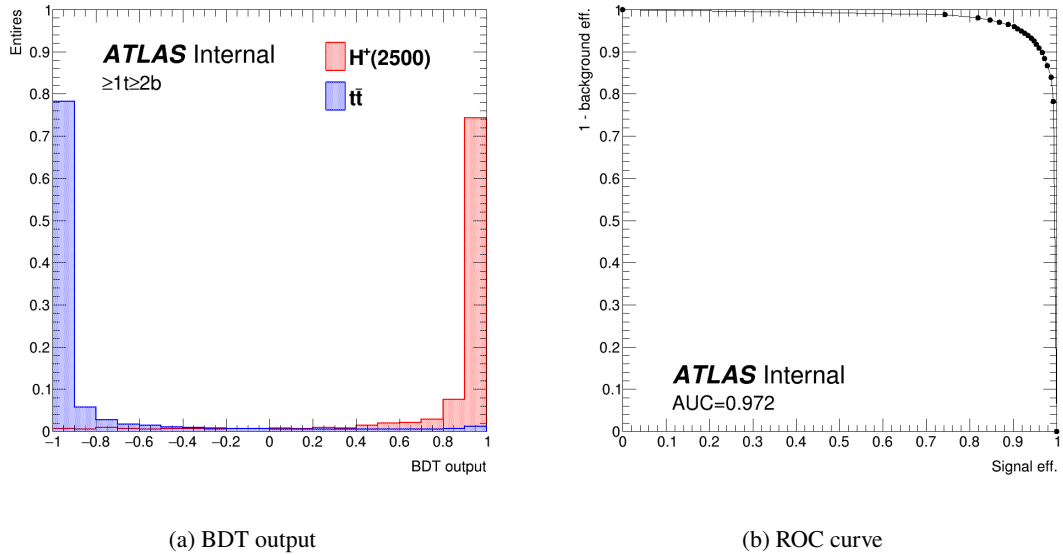


Figure 13: BDT distribution and ROC curve for the 2500 GeV H^+ mass hypothesis.

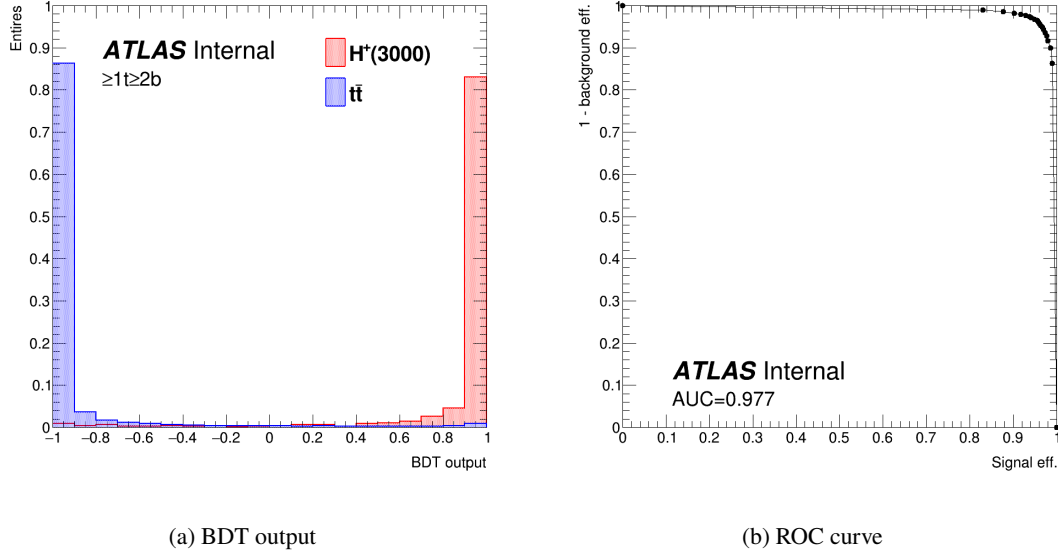


Figure 14: BDT distribution and ROC curve for the 3000 GeV H^+ mass hypothesis.

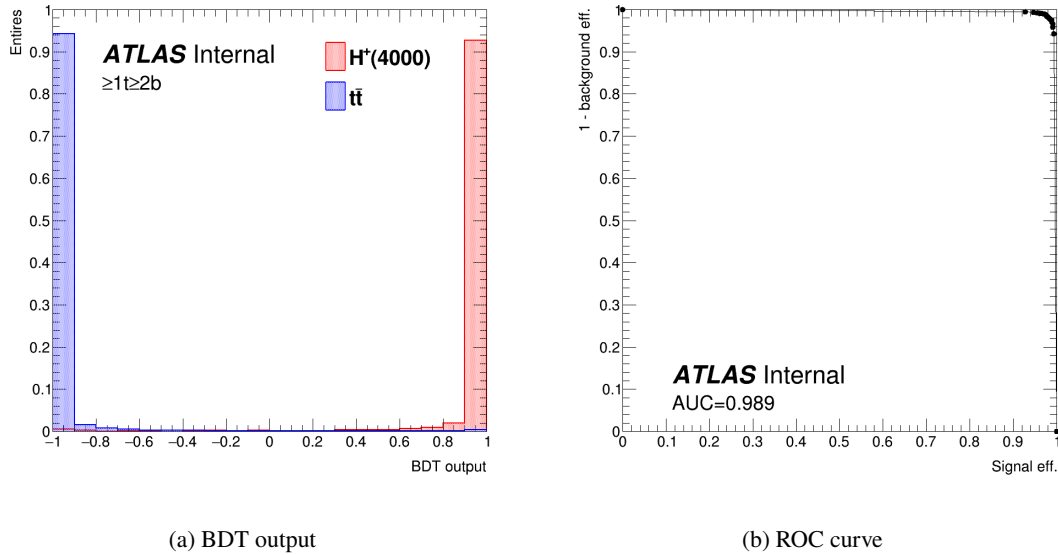


Figure 15: BDT distribution and ROC curve for the 4000 GeV H^+ mass hypothesis.

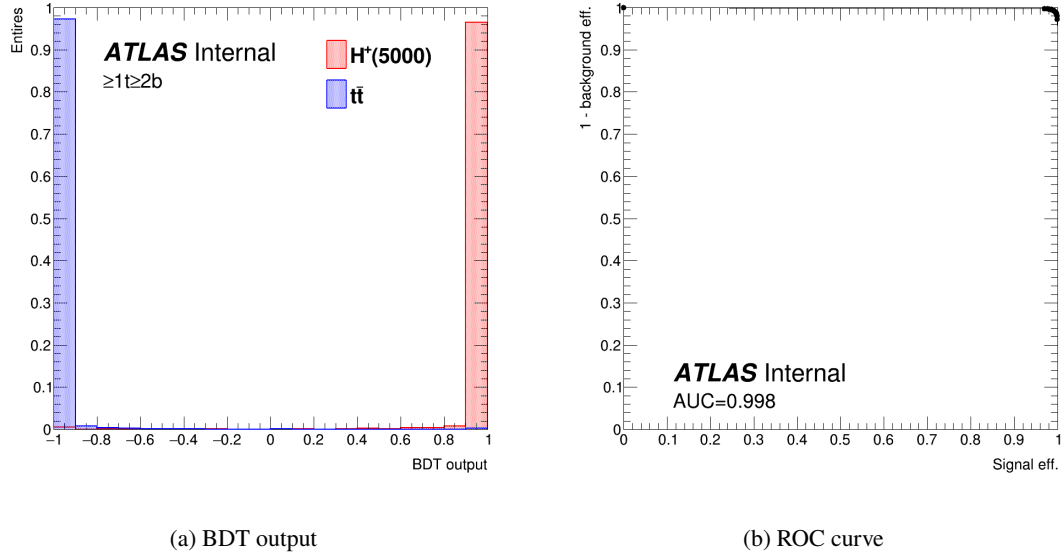


Figure 16: BDT distribution and ROC curve for the 5000 GeV H^+ mass hypothesis.

470 **5 Background modeling**

471 **5.1 Blind strategy**

472 In the following sections, modeling of kinematic distributions, in particular the ones used for BDT training,
473 of the $t\bar{t} + \text{jets}$ background is checked by comparing the data and MC. In order to avoid observing signals
474 or any other biases before fixing the analysis procedure, the following blinding strategy is applied. The
475 signal to noise ratio (S/B) is calculated in each bin of each distribution for all H^+ mass hypothesis (more
476 details in Appendix B). The signal cross section (σ_{signal}) on each H^+ mass hypothesis is set to 0.046 pb,
477 which is the upper limits at 1 TeV H^+ mass point obtained from the resolved $H^+ \rightarrow tb$ search [24], and
478 therefore it can be considered as the most conservative assumption. The data in bins with $S/B > 0.05$ in at
479 least one H^+ mass hypothesis are blinded when the data is compared with MC.

480 **5.2 Data/MC comparison for BDT input variables**

481 Figures 17 show the distributions of input variables for BDT training. Data are blinded according to
482 the blind strategy in Section 5.1. No significant difference between the data and MC is found in each
483 variable.

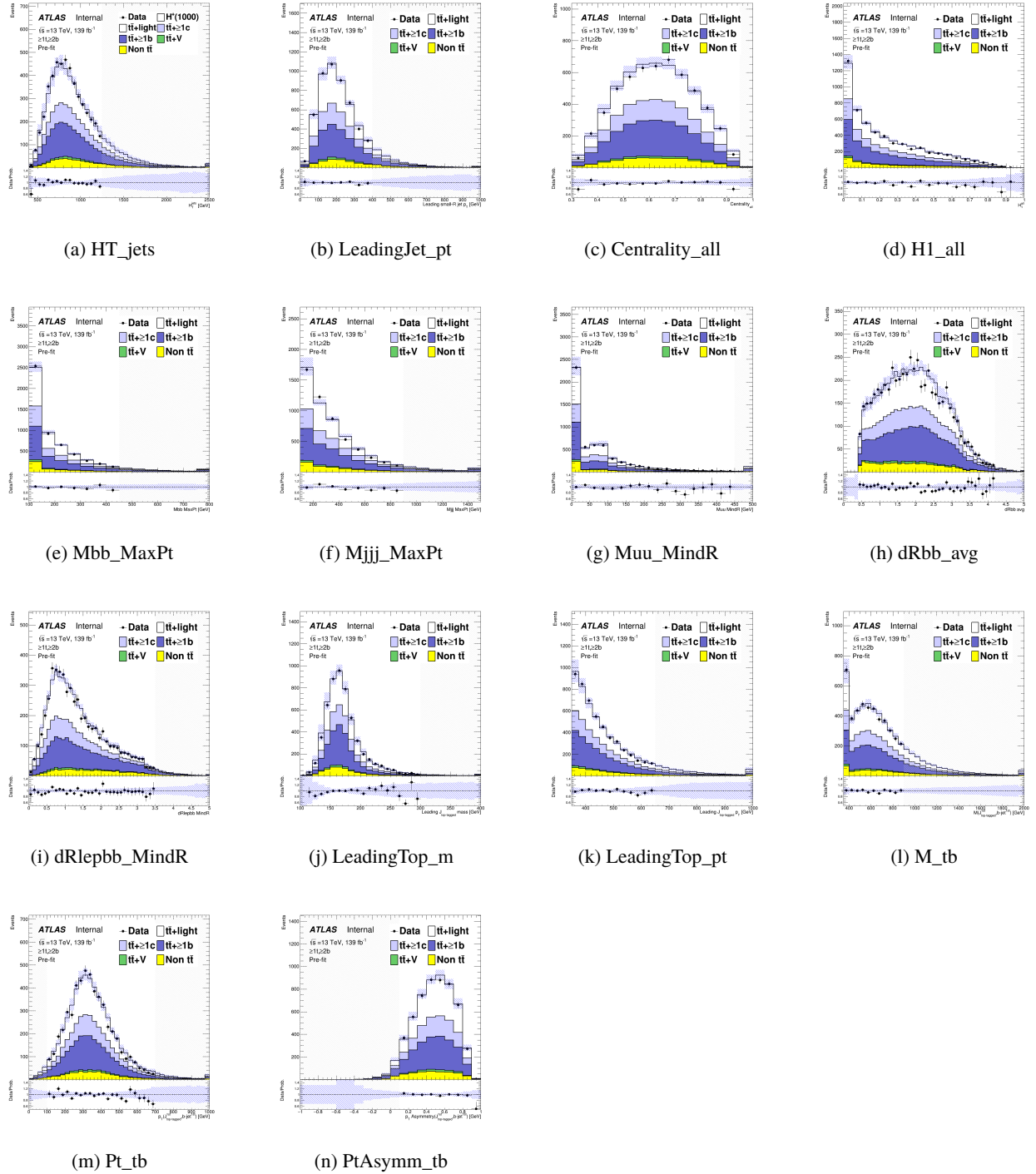


Figure 17: Comparison of the kinematic variables included in the BDT in the SR for the data and MC.

484 5.3 Data/MC comparison for BDT distributions

485 Figures 18 to 25 show the distributions of BDT output in SR and H_T^{jets} in CR. The binning of the BDT
 486 output is optimized for the search sensitivity by *TransfoD* algorithm [93]. Such binning results in extremely
 487 narrow bins towards high BDT scored, and makes the plot hard to see as shown in Figure 68 in Appendix
 488 B.2, when plotted in a usual manner. We rather show the distribution with equal interval for each bin. The
 489 distributions are input into the profile likelihood fit on each H^+ mass hypothesis as shown in Section 7. It
 490 is observed that the data/MC ratio tends to be lower for the high BDT score regions, which may bias search
 491 for the signal in the highest BDT bins. The reweighting to correct for the slope is discussed in Section 5.4.
 492 In H_T^{jets} distributions, there is no significant difference in the shape, while the normalization is significantly
 493 different. The $t\bar{t}$ + light yields are therefore determined by floating them in the fit.

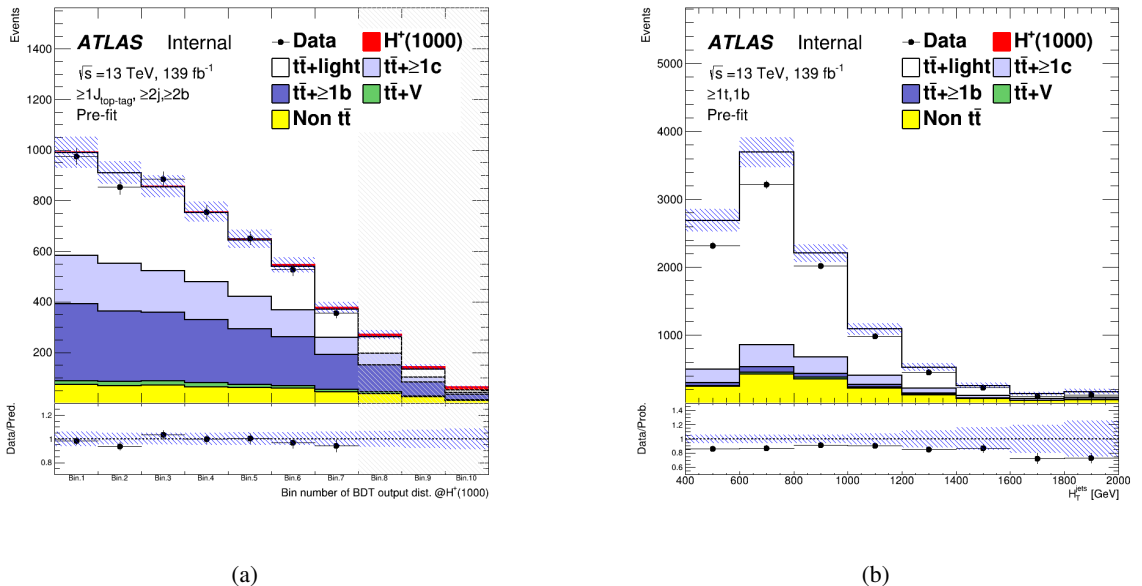


Figure 18: Pre-fit distribution of BDT output in the SR (a) and H_T^{jets} in the CR for the 1000 GeV H^+ mass hypotheses.

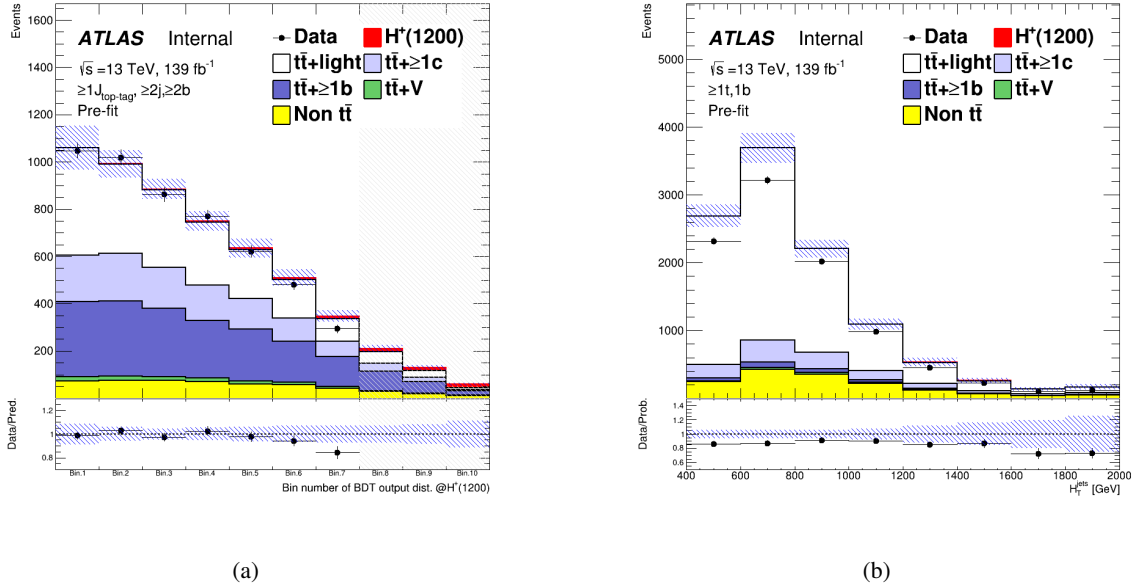


Figure 19: Pre-fit distribution of BDT output in the SR (a) and H_T^{jets} in the CR for the 1200 GeV H^+ mass hypotheses.

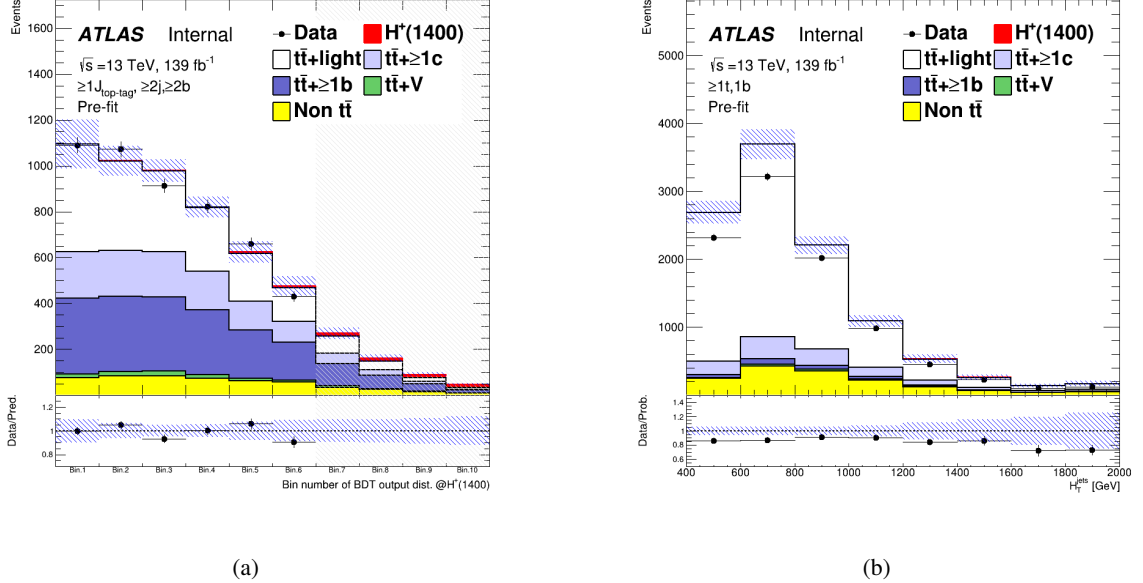


Figure 20: Pre-fit distribution of BDT output in the SR (a) and H_T^{jets} in the CR for the 1400 GeV H^+ mass hypotheses.

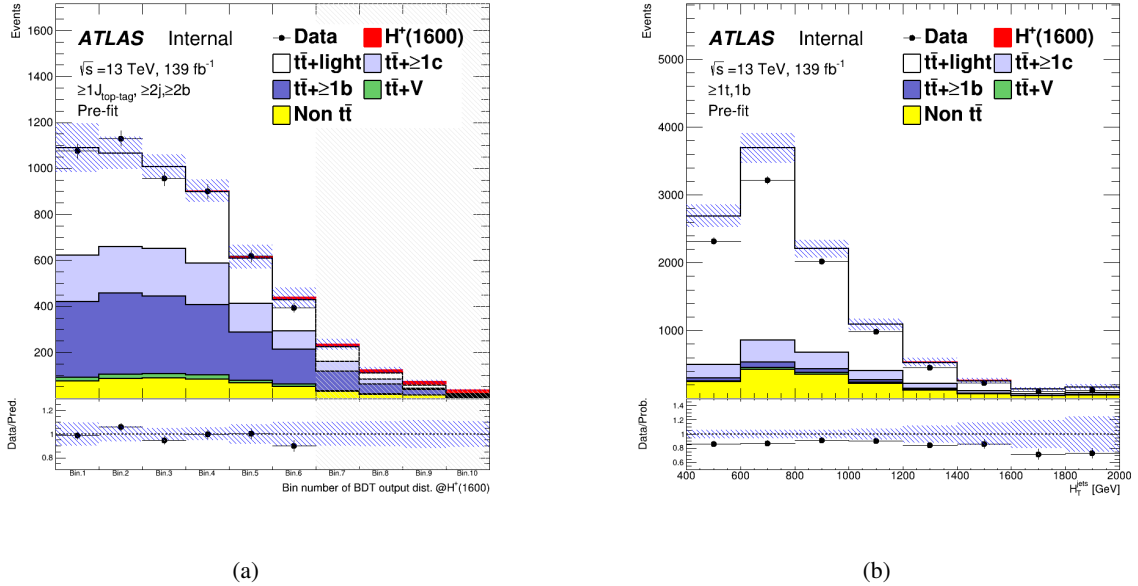


Figure 21: Pre-fit distribution of BDT output in the SR (a) and H_T^{jets} in the CR for the 1600 GeV H^+ mass hypotheses.

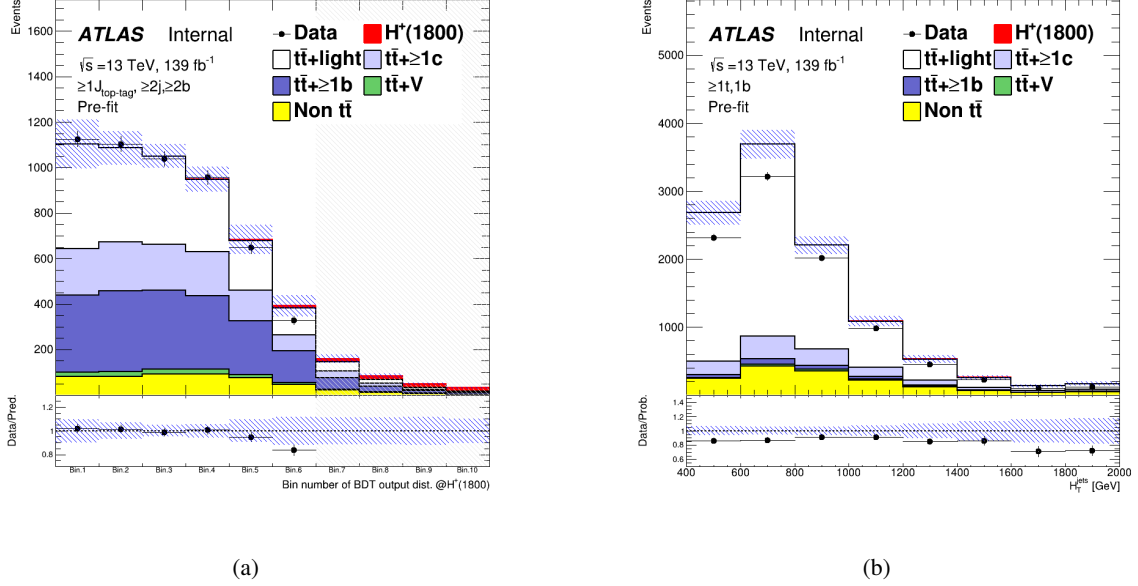


Figure 22: Pre-fit distribution of BDT output in the SR (a) and H_T^{jets} in the CR for the 1800 GeV H^+ mass hypotheses.

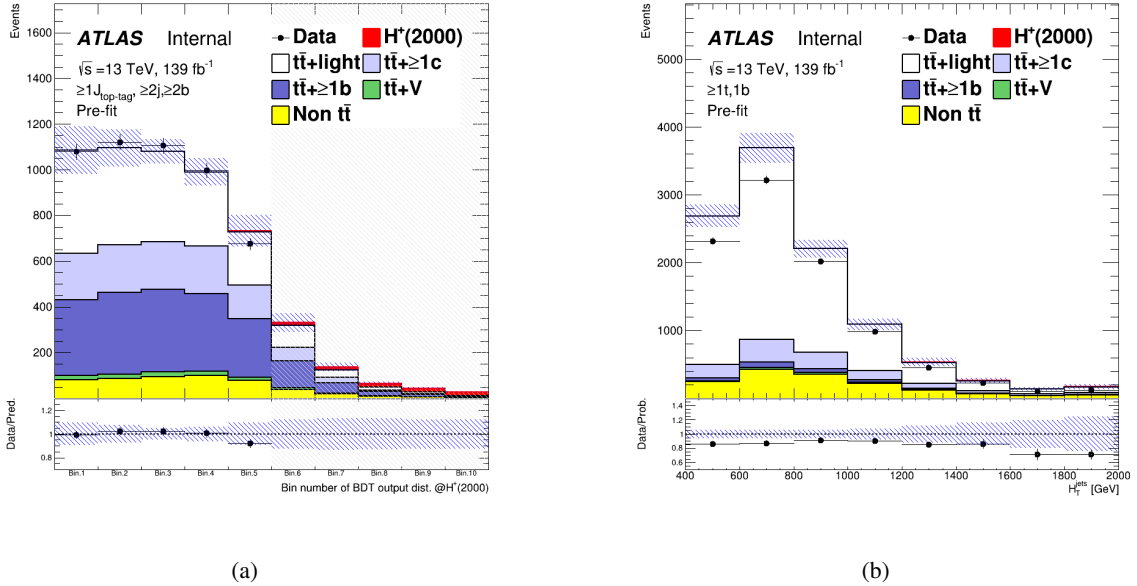


Figure 23: Pre-fit distribution of BDT output in the SR (a) and H_T^{jets} in the CR for the 2000 GeV H^+ mass hypotheses.

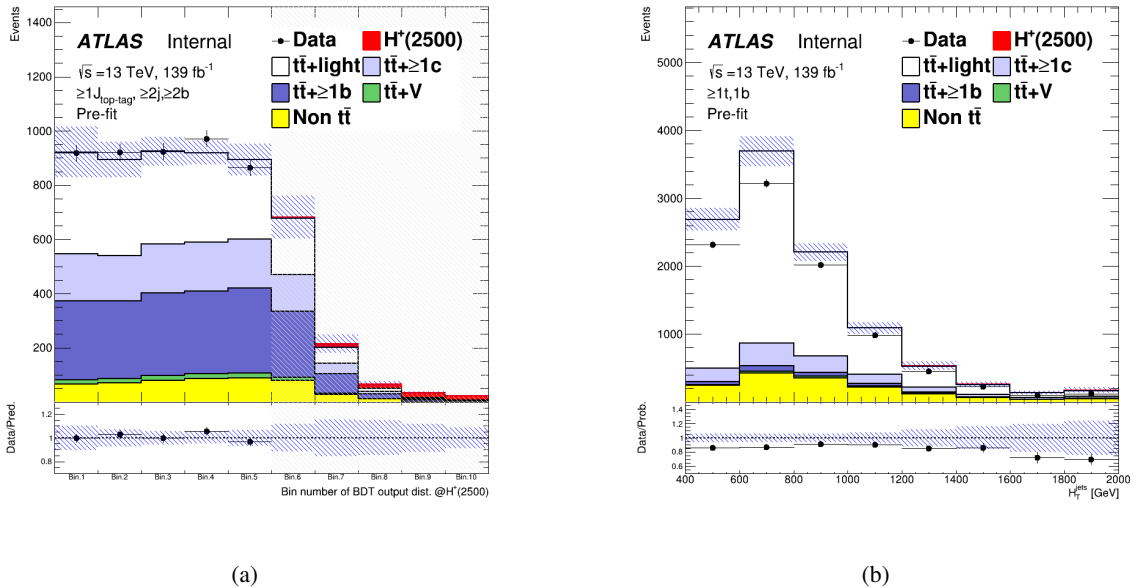


Figure 24: Pre-fit distribution of BDT output in the SR (a) and H_T^{jets} in the CR for the 2500 GeV H^+ mass hypotheses.

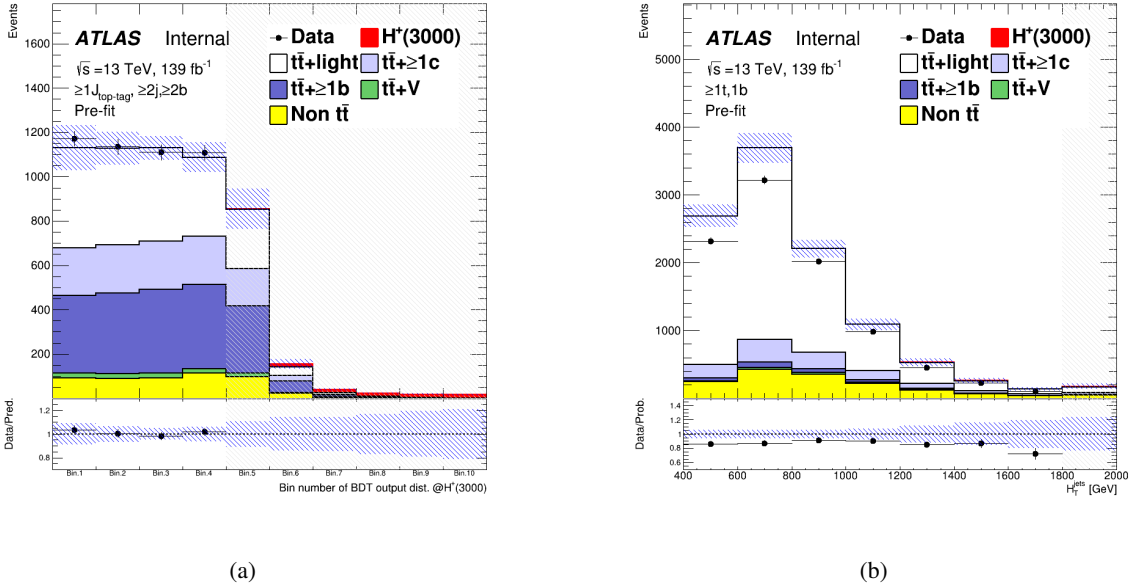


Figure 25: Pre-fit distribution of BDT output in the SR (a) and H_T^{jets} in the CR for the 3000 GeV H^+ mass hypotheses.

494 5.4 Reweighting technique

495 It is known that the $t\bar{t}$ Powheg+Pythia generator does not properly model data. Actually, BDT output
 496 distributions in the high score region are different between data and MC as shown in Figure 18 to 25. To
 497 improve the data/MC agreement, data-based corrections are applied to the MC prediction. Reweighting
 498 factors are derived by comparing the data and MC prediction in the SR. For deriving reweighting factors,
 499 events in the only low BDT score region are selected to avoid being reweighted signal events. These events
 500 are required to pass all BDT cuts under different mass hypotheses as shown in Table 14. The reweighting
 501 factors can be expressed as:

$$R(x) = \frac{\text{Data}(x) - \text{MC}^{\text{non-}t\bar{t}+\text{jets}}(x)}{\text{MC}^{t\bar{t}+\text{jets}}(x)} \quad (1)$$

502 where x is the variable mismodelled by the MC simulation. $t\bar{t} + \text{jets}$ includes the $t\bar{t} + \text{light}$, $t\bar{t}+ \geq 1c$ and
 503 $t\bar{t}+ \geq 1b$. Weights are calculated from the H_T^{jets} distribution in the SR region. Figure 26(a) shows the
 504 distribution of H_T^{jets} with BDT score cuts applied as shown in Table 14. Figure 26(b) shows the distribution
 505 of the weights derived from the H_T^{jets} distribution and a quadratic function form ($\omega = a + bx + cx^2$) obtained
 506 by fitting to the weight distribution. The function values are applied to $t\bar{t} + \text{light}$, $t\bar{t}+ \geq 1c$ and $t\bar{t}+ \geq 1b$.
 507 Table 15 includes the fitted values for all the parameters. The statistical errors of fitted parameters are
 508 included as systematic uncertainties in the profile likelihood. The weight values in $H_T^{\text{jets}} > 2057$ GeV
 509 region are extrapolated the value at $H_T^{\text{jets}} = 2057$ GeV, because the weight value of -1σ is negative at the
 510 point.

Mass point [GeV]	BDT score cut
1000	< 0.5
1200	< 0.5
1400	< 0.5
1600	< 0.5
1800	< 0.5
2000	< 0.5
2500	< 0.5
3000	< -0.2
4000	< -0.2
5000	< -0.2

Table 14: Events used for deriving weight factors are selected by cutting with BDT score under different mass hypotheses according to criterias in this tables. After the selection, S/B value at each bin is <0.05 for each BDT output distribution as shown in Figure 69

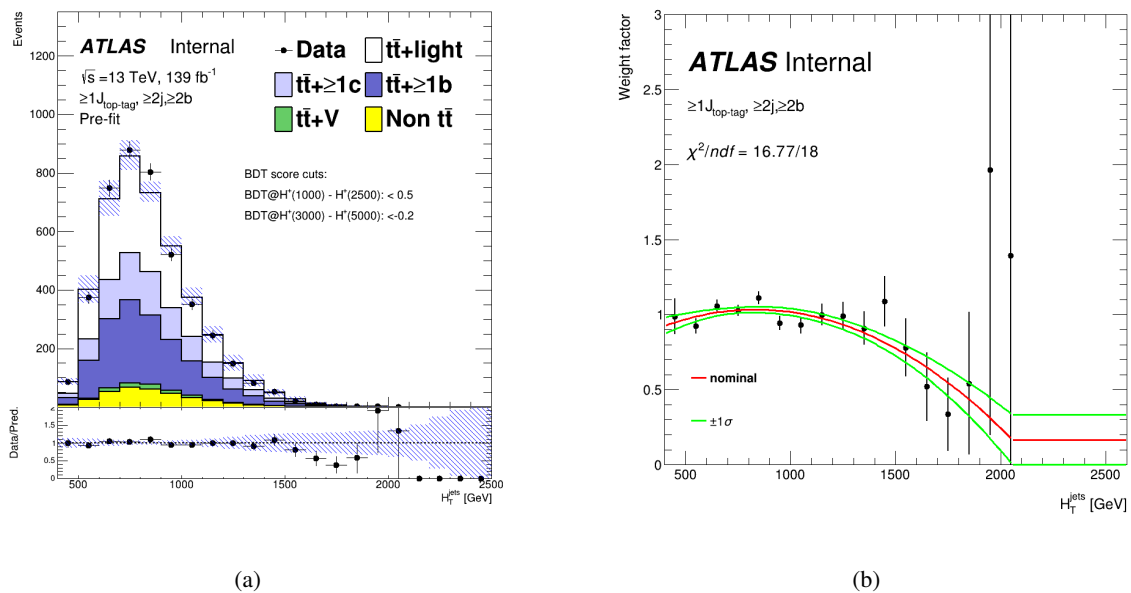


Figure 26: The H_T^{jets} distribution with BDT score cuts applied (left) and the weight distribution derived from the H_T^{jets} distribution (right) are shown. The red plot in the weight distribution is the quadratic function obtained by fitting to the weight distribution ($\omega = a + bx + cx^2$). The green ones are $\pm 1\sigma$ of the red function from the statistical errors of fitted parameters. These statistical errors are included as systematic uncertainties in the profile likelihood fit.

Parameter	Value
a	$(6.33 \pm 1.50) \times 10^{-1}$
b	$(9.63 \pm 3.04) \times 10^{-4}$
c	$(-5.78 \pm 1.46) \times 10^{-7}$

Table 15: Summary of parameters obtained by fitting to the weight distribution with a quadratic function ($\omega = a + bx + cx^2$). Error of each parameter is from statistical uncertainty.

Figure 27 to Figure 34 show the effect of the reweighting in BDT output distributions in the SR region. The data/MC improved after the reweighting for each H^+ mass hypothesis.

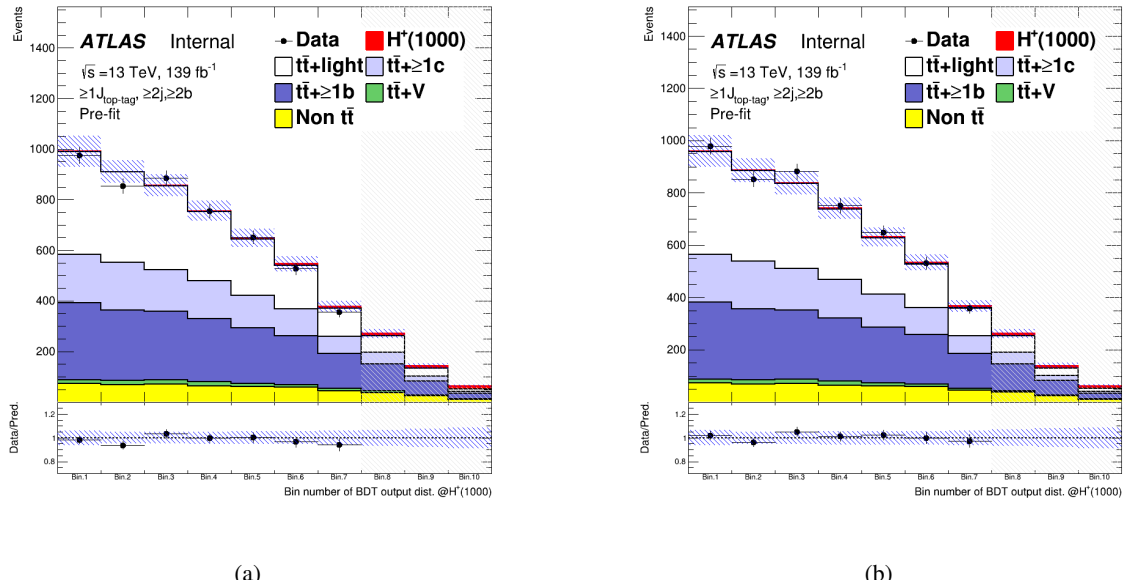


Figure 27: BDT output distribution for the 1000 GeV H^+ mass hypothesis before (left) and after (right) the reweighting.

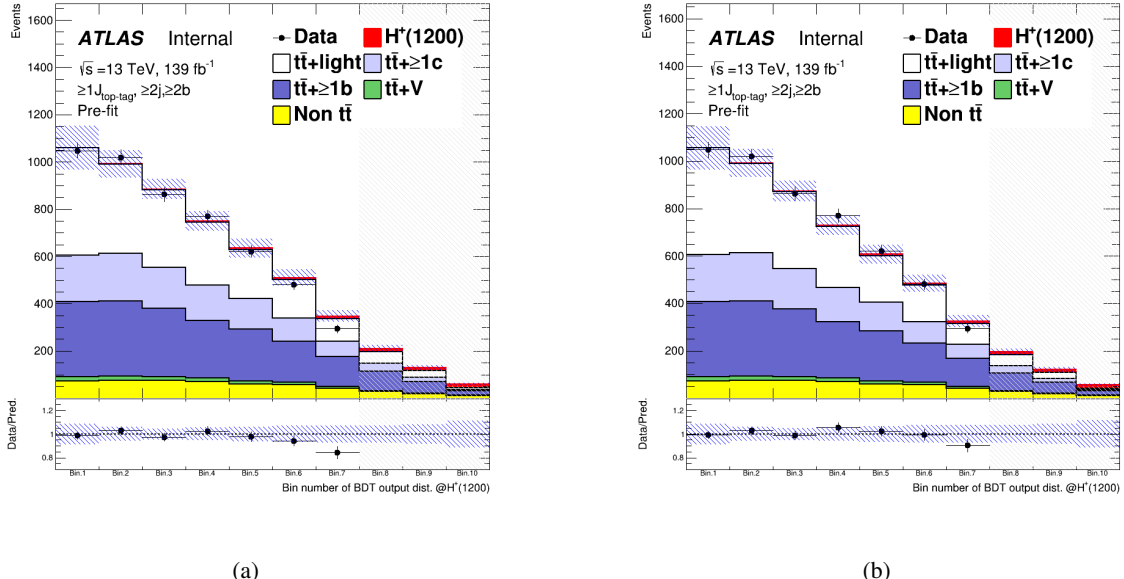


Figure 28: BDT output distribution for the 1200 GeV H^+ mass hypothesis before (left) and after (right) the reweighting.

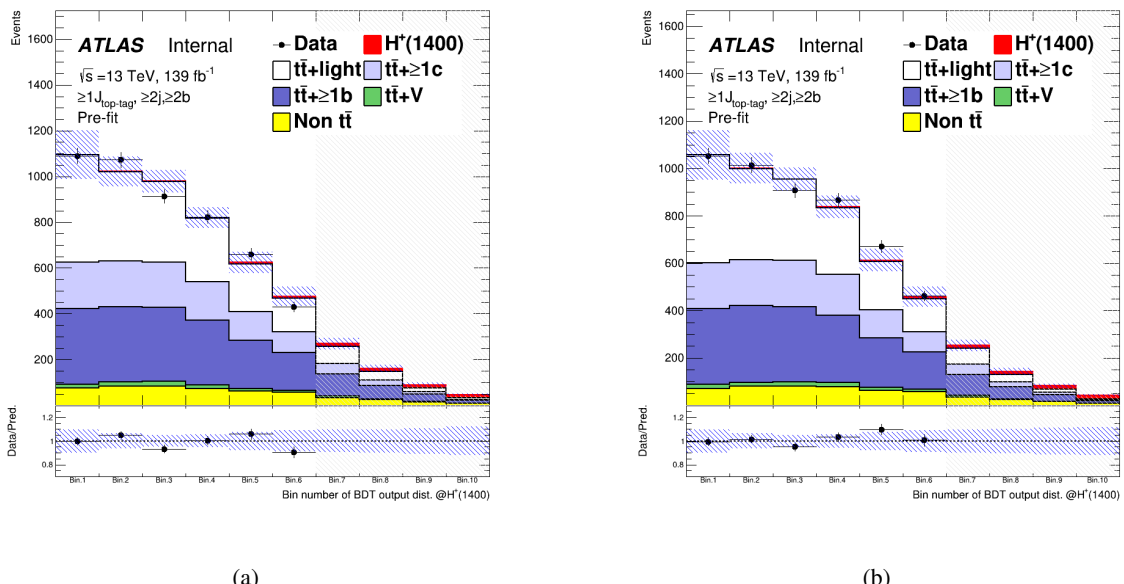


Figure 29: BDT output distribution for the 1400 GeV H^+ mass hypothesis before (left) and after (right) the reweighting.

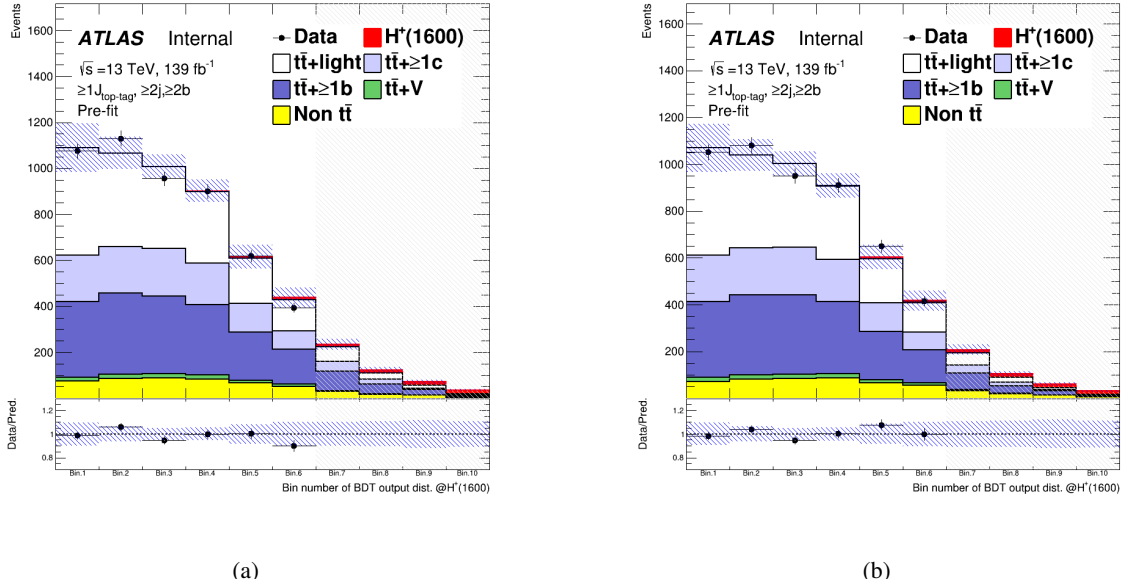


Figure 30: BDT output distribution for the 1600 GeV H^+ mass hypothesis before (left) and after (right) the reweighting.

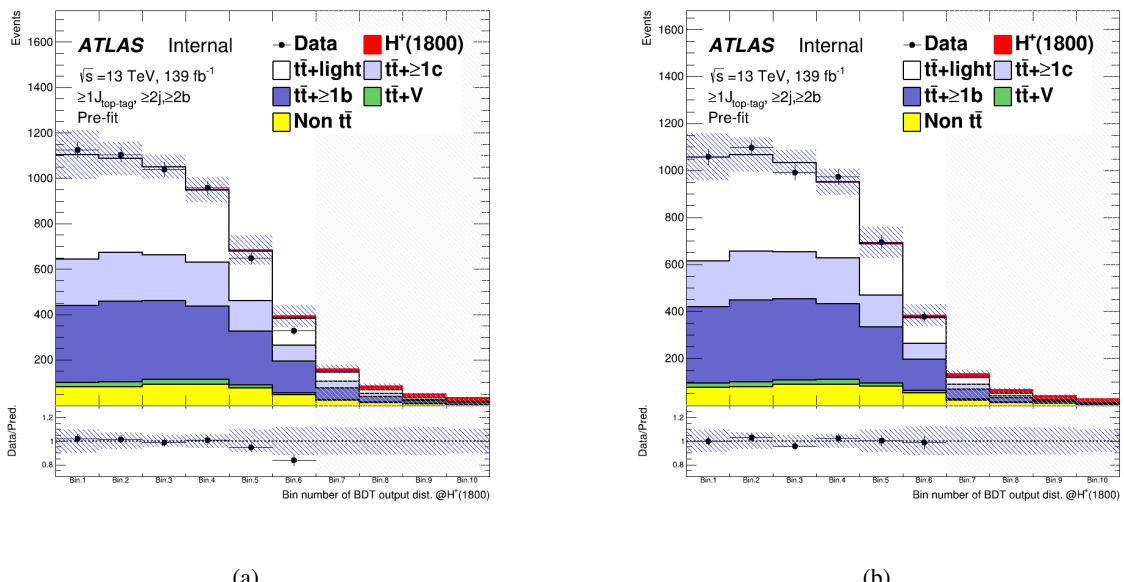


Figure 31: BDT output distribution for the 1800 GeV H^+ mass hypothesis before (left) and after (right) the reweighting.

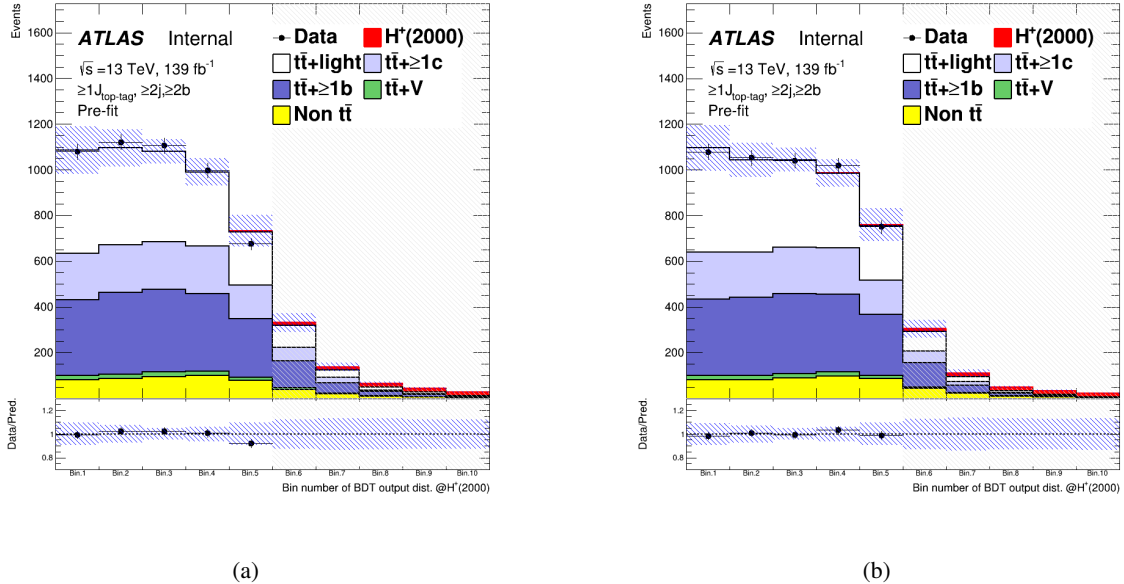


Figure 32: BDT output distribution for the 2000 GeV H^+ mass hypothesis before (left) and after (right) the reweighting.

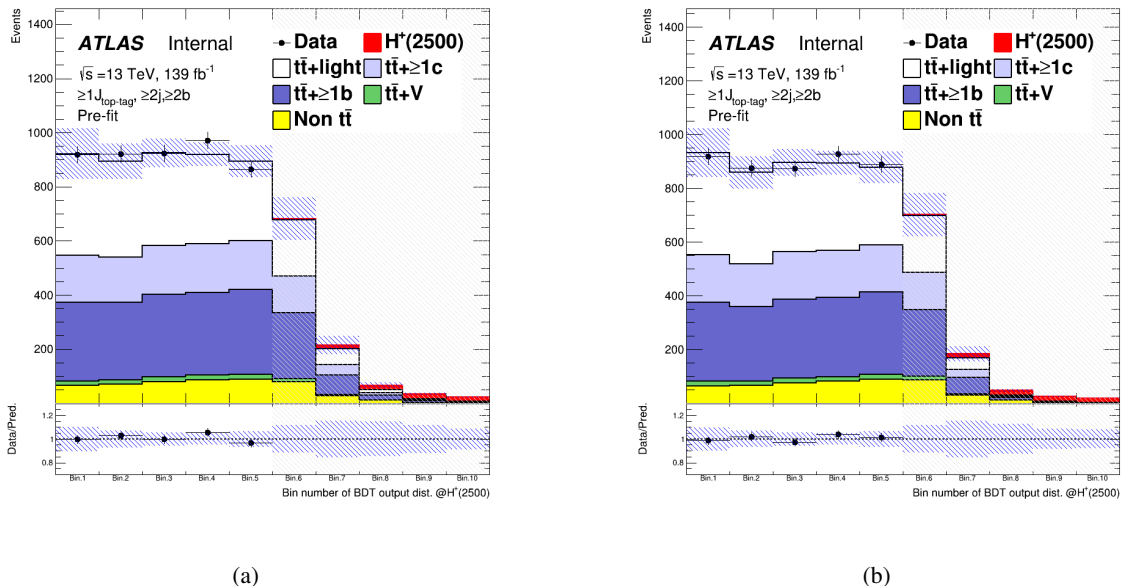


Figure 33: BDT output distribution for the 2500 GeV H^+ mass hypothesis before (left) and after (right) the reweighting.

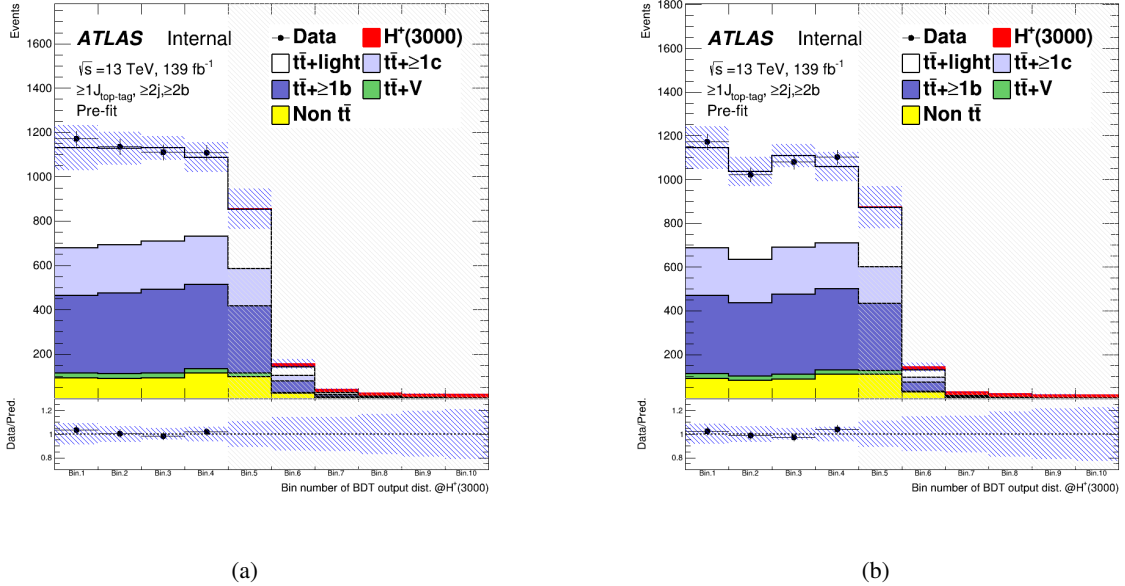


Figure 34: BDT output distribution for the 3000 GeV H^+ mass hypothesis before (left) and after (right) the reweighting.

513 6 Systematics Uncertainties

514 The uncertainties considered in the following may affect the overall normalization of the process, the shapes
 515 of the BDT and H_T^{jets} , or both. All the experimental uncertainties considered, with the exception of that in
 516 the luminosity, affect both normalization and shape in all the simulated samples. Uncertainties related
 517 to the modeling of the signal and background affect both normalization and shape, with the exception of
 518 cross-section and $t\bar{t}$ modeling uncertainties. The former only affect the normalization of the considered
 519 sample, while the latter only affect the shape of $t\bar{t}$ samples. Nevertheless, the noramlisation uncertainties
 520 modify the relative fractions of the different samples, leading to a shape uncertainty in the final BDT and
 521 H_T^{jets} distributions.

522 A single independet nuisance parameter is assigned to each source of systematic uncertainty in the statistical
 523 analysis. Some of the systematic uncertainties, in particular most of the experimental ones, are decomposed
 524 into several independent sources, as specified in the following. Each individual source then has a correlated
 525 effect across all analysis regions and signal and background samples. Table 16 presents a list of all
 526 systematic uncertainties considered and indicates for each category the number of independent components
 527 and whether they affect normalisaion of shape.

528 6.1 Luminosity and pile-up modeling

529 6.1.1 Luminosity

530 The uncertainty on the integrated luminosity for the full Run-2 data-set is 1.7% [30], obtained using
 531 LUCID-2 detector [94] for the primary luminosity measurement.

532 6.1.2 Pile-up modeling

533 A variation in the pile-up reweighting of the simulated events is included to cover the uncertainties in the
 534 ratio of the predicted and measured inelastic cross-sections in the fiducial volume defined by $M_X > 13$
 535 GeV, where M_X is the mass of the hadronic system [95].

536 cdi

537 6.2 Reconstructed objects

538 6.2.1 Charged leptons

539 Uncertainties associated with charged leptons arise from the trigger selection, the object reconstruction,
 540 identification and isolation criteria, as well as the lepton momentum scale and resolution. The reconstruction,
 541 identification and isolation efficiency of electrons and muons, as well as efficiency of the trigger used
 542 to record the events, differ slightly between data and simulation, which is compensated for by dedicated
 543 scale factors (SFs). Efficiency SFs are measured using tag-and-probe techniques on $Z \rightarrow l^+l^-$ data and
 544 simulated samples [73, 96], and are applied to the simulation to correct for the differences. The effect of
 545 these SFs as well as of their uncertainties are propagated as corrections to the MC event weight. In total,
 546 four independent components are considered for electrons and ten for muons.

Systematics uncertainty	Type	Components
Experimental uncertainties		
Luminosity	N	1
Pileup modeling	SN	1
<i>Physics objects</i>		
Electrons	SN	7
Muons	SN	15
Small-R jet energy scale	SN	31
Small-R jet energy resolution	SN	9
Small-R jet mass scale	SN	8
Large-R jet energy scale	SN	24
Large-R jet energy resolution	SN	12
Large-R jet mass scale	SN	18
Large-R jet mass resolution	SN	10
Jet vertex tagger	SN	1
<i>b</i> -tagging		
Efficiency	SN	45
Mis-tag rate (c)	SN	20
Mis-tag rate (light)	SN	20
<i>top</i> -tagging		
Signal efficiency	SN	9
p_T extrapolation signal efficiency	SN	1
background efficiency	SN	5
inefficiency	SN	3
Signal and background modeling		
<i>Signal</i>		
PDF variations	SN	30
Scales	SN	2
<i>t</i> \bar{t} background		
PDF variations	SN	90
$t\bar{t} + \geq 1c$ and $t\bar{t} + \geq 1b$ normalization	N (free floating)	1
$t\bar{t} +$ light normalization	N (free floating)	1
$t\bar{t} +$ light modeling	S	6
$t\bar{t} + \geq 1c$ modeling	S	6
$t\bar{t} + \geq 1b$ modeling	S	6
$t\bar{t} +$ jets reweighting	SN	1
<i>Other backgrounds</i>		
$t\bar{t}W$ cross-section	N	2
$t\bar{t}Z$ cross-section	N	2
$t\bar{t}W$ modeling	SN	1
$t\bar{t}Z$ modeling	SN	1
Single top cross-section	N	3
Single top modeling	SN	6
W+jets normalization	N	3
Z+jets normalization	N	1
Diboson normalization	N	1
$t\bar{t}t\bar{t}$ cross-section	N	3

Table 16: List of systematic uncertainties included in the analysis.

547 Additional sources of uncertainty originate from the corrections applied to adjust the lepton momentum
 548 scale and resolution in the simulation to match those in data, measured using reconstructed distributions of
 549 the $Z \rightarrow l^+l^-$ and $J/\psi \rightarrow l^+l^-$ masses, as well as the E/p ratio measured in $W \rightarrow e\nu$ events, where E and p
 550 are the electron energy and momentum measured by the calorimeter and the tracker, respectively [73, 97].
 551 To evaluate the effect of momentum scale uncertainties, the event selection is redone with the lepton energy
 552 or momentum varied by $\pm 1\sigma$. For the momentum resolution uncertainties, the event selection is redone
 553 by smearing the lepton energy or momentum. In total, three independent components are considered for
 554 electrons and five for muons.

555 6.2.2 Small- R jets, Large- R jets

556 Uncertainties associated with jets arise from the efficiency of pile-up rejection by the JVT, from the jet
 557 energy scale (JES) and resolution (JER), from the jet mass scale (JMS) and resolution (JMR), and from b -
 558 and top-tagging.

559 Jet vertex tagging:

560 Scale factors are applied to correct for discrepancies between data and MC for JVT efficiencies.
 561 These SFs are estimated using $Z \rightarrow \mu^+\mu^-$ with tag-and-probe techniques similar to those in Ref.[78],
 562 and the effect of these SFs as well as of their uncertainties are propagated as corrections to the MC
 563 event weight.

564 Small- R jet:

565 The *R4_CategoryReduction_FullJER.config* jet uncertainties configuration is used. The JES and
 566 its uncertainty for small- R jets are derived by combining information from test-beam data, LHC
 567 collision data and simulation [98]. The uncertainties from these measurements are factorized into
 568 several independent sources. Additional uncertainties are considered, related to jet flavor (using the
 569 conservative default value of $50 \pm 50\%$ for the quark/gluon fraction for all MC samples), pile-up
 570 corrections, η dependence, high- p_T jets, and differences between full and fast simulation, yielding a
 571 total of 31 independence sources.

572 The JER was measured in Run-2 data and simulation as a function of jet p_T and rapidity using dijet
 573 events, using a similar method as that in Ref. [99]. The combined uncertainty is propagated by
 574 smearing the jet p_T in MC, yielding to nine independent sources.

575 The JMS uncertainties for small- R jets are derived using the RTrk uncertainties that compares the
 576 ratio of the jet mass for calorimeter jets to the jet mass of track-based jets in data and MC simulation
 577 [100]. The six NPs are provided related with baseline, modeling, tracking and total statistics. The
 578 technique takes advantage of two independent measures of the jets mass (in the calorimeter and
 579 using the ID), however this assumption breaks in the case of particle flow jets which uses both
 580 calorimeter and tracking information. For PFlow jets, the uncertainties derived for EMTopo jets are
 581 used and two additional uncertainties are provided. These uncertainties are derived by comparing
 582 the jet mass of EMTopo and PFlow jets in data and MC. Two NPs are provided similarly to the RTrk
 583 uncertainties related with baseline and modeling. The JMS uncertainties are intentionally derived
 584 after the application of the JES and JER smearing. This is different compared to large- R jets where
 585 no nominal JER smearing is applied. The JES corrects the overall energy scale, which impacts the
 586 mass as it is applied to the full four-vector. The JMS correction and uncertainties are then a residual

587 correction accounting for the distribution of energy within the jet. For this reason, the JES and JMS
 588 uncertainties are to first order uncorrelated effects.

589 **Large- R jet:**

590 The *R10_CategoryJES_FullJER_FullJMS.config* jet uncertainties configuration is used for JES, JER
 591 and JMS variation. JES uncertainties for large- R jets are derived using a similar approach as for
 592 small- R jets [100]. Correlation between these two objects are taken into account in uncertainty
 593 evaluation. Additional uncertainties related with a topology of an event are included.

594 The JER uncertainties for large- R jets are derived in the same way as the small- R jets uncertainties.
 595 The dijet balance asymmetry is used to evaluate the JER, which is sufficient to cover the fully
 596 supported kinematic regime for large- R jet usage. The nominal data/MC difference is found to
 597 be consistent with 1 within uncertainty. For this reason, no nominal JER smearing is applied.
 598 Instead, the nominal data/MC difference from 1 is taken as an additional uncertainty on top of the
 599 uncertainties related with limited statistics, detector effects, or modeling. The FullJER model with
 600 12 NPs is used. Both data and MC events are smeared to cover properly the correlations between jets
 601 different regions of the detector.

602 The JMS uncertainties for large- R jets are derived from the forward folding technique (FF) in the
 603 limited region of $200 \text{ GeV} < p_T < 1000 \text{ GeV}$ around the W and top mass peaks [100, 101]. The
 604 Rtrk technique is used to extend this region to $200 \text{ GeV} < p_T < 3000 \text{ GeV}$, $m < 600 \text{ GeV}$ and
 605 $|\eta| < 2.0$. The forward folding method is used to fit the W and top mass peaks in $t\bar{t}$ semileptonic
 606 events. The Rtrk method uses the double ratio of data/MC for calorimeter only quantities and
 607 track-only quantities. This technique can cover wider range in p_T , η and mass. However, forward
 608 folding technique is more precise in the lower p_T region and the mass around the top and W masses.
 609 The uncertainties from the two approaches are combined and fitted as a function p_T in a given mass
 610 bin. Interpolation between mass bins is used to provide smooth uncertainties. The full set of JMS
 611 NPs is used in the analysis in order to allow possible combinations with other measurements. The
 612 NPs are related with limited statistics of measurements, detector effects, modeling and selections. In
 613 addition, uncertainties related with interpolation between mass bins and uncertainties related with a
 614 difference between QCD and hadronic decay jet mass response are included.

615 Measurements of the JMR in the $t\bar{t}$ semileptonic events are also used to constrain the JMR uncertainties
 616 by using the forward folding method [100, 101]. Measurements are performed in two mass regions
 617 to cover W boson and top quark mass peaks. The W boson mass peak is fitted in a region of
 618 $50 \text{ GeV} < m_{\text{jet}} < 120 \text{ GeV}$ and $200 \text{ GeV} < p_{T,\text{jet}} < 350 \text{ GeV}$. The top mass peak is fitted in a region
 619 of $120 \text{ GeV} < m_{\text{jet}} < 300 \text{ GeV}$ and $350 \text{ GeV} < p_{T,\text{jet}} < 1000 \text{ GeV}$. Relative JMR uncertainty of 20%
 620 is used outside these regions. FullJMR uncertainty model with 10 nuisance parameters is used to
 621 cover uncertainties related with measurement of JMR using FF method, interpolation between bins
 622 and comparison between different MC models for events outside the two gions. This measurement is
 623 within top mass interval. However, $p_{T,\text{jet}}$ exceeds the p_T range provided by the FF method.

624 **b -tagging:**

625 b -tagging efficiencies in simulated samples are corrected to match efficiencies in data. Scale factors
 626 are derived as a function of p_T for jets containing b -jets, c -jets and for jets containing neither b -
 627 nor c -hadrons (light-jets) separately, in dedicated calibration analysis. For b -jets efficiencies, $t\bar{t}$
 628 events in the dilepton topology are used, exploiting the very pure sample of b -jets arising from the
 629 decays of the top quarks [79]. For c -jet mistag rates, $t\bar{t}$ events in signle-lepton topology are used,
 630 exploiting the c -jets from the hadronically decaying W bosons, using techniques similar as those in

Ref. [102]. For light-jets mistag rates, the so-called negative-tag method similar as that in Ref. [103] is used, but using $Z + \text{jets}$ events instead of di-jet events. In the three calibration analyses, a large number of uncertainty components are considered, and a principal component analysis is performed, yielding in 45, 20 and 20 eigenvariations, respectively, for b -, c and light-jets, which are taken as uncorrelated sources of uncertainties. The number of these eigenvariations correspond to the number of p_T bins, (9, 4 and 4, respectively, for b -, c - and light-jets) multiplied by the number of the tag weight bins ($\varepsilon \in [0\%, 60\%], [60\%, 70\%], [70\%, 77\%], [77\%, 85\%], [85\%, 100\%]$). The calibration used in this analysis is stored in following "CDI file":

`/cvmfs/atlas.cern.ch/repo/sw/database/GroupData/xAODTaggingEfficiency/13TeV/2020-21-13TeV-MC16-CDI-2021-04-16_v1.root.`

Top-tagging:

Uncertainties related with the top-tagging calibration are provided for the signal and the background jets [85, 104]. Jets are called signal if they passed contained top criteria. Otherwise, they are called background jet. Uncertainties for back ground jets are measured in two phase-spaces containing QCD multijet and gamma+jet processes. The signal jets uncertainties are measured in the boosted $t\bar{t}$ lepton+jets channel in the range of leading large-R jet $p_T \leq 1$ TeV, because there are too few $t\bar{t}$ events to extract scale factors for $p_T \geq 1$ TeV. Therefore, additional uncertainties are assigned to cover signal modeling effects and extrapolation beyond the phase-spaces. These uncertainties were released as part of the consolidated large- R jet uncertainties.

6.3 Signal modeling

6.3.1 H^+ signal

The H^+ signal uncertainty is modeled in two way: by using the PDF uncertainties and through the variation of μ_f and μ_r . The uncertainties from the modeling of the PDF, which is done with the NNPDF2.3 (3.0) PDF set for datasets simulated at ≤ 3.0 (≥ 4.0) TeV, is made using a symmetrized Hessian set, PDF4LHC15_nlo_30, following the PDF4LHC recommendations for LHC Run II [105]. The signal scale uncertainty is modeled by varying μ_f and μ_r up (and down) by a factor 2 (or 0.5).

6.4 Background modeling

6.4.1 $t\bar{t}+\text{jets}$

$t\bar{t} + \text{heavy flavor classification}$

The $t\bar{t} + \text{jets}$ background is categorized according to the flavor of additional jets in the event, using the same procedure as described in Ref. [23]. Generator-level particle jets are reconstructed from stable particles (mean lifetime $\tau > 3 \times 10^{-11}$ seconds) using the anti- k_t algorithm with a radius parameter $R = 0.4$, and are required to have $p_T > 15$ GeV and $|\eta| < 2.5$. The flavor of a jet is determined by counting the number of b - or c -hadrons within $\Delta R < 0.4$ of the jet axis. Jets matched to exactly one b -hadron, with p_T above 5 GeV, are labeled single- b -jets, while those matched to two or more b -hadrons are labeled b -jets (with no p_T requirement on the second hadron); single- c - and c -jets are defined analogously, only considering jets not already defined as single- b - or b -jets. Events that have at least one single- b - or b -jet, not counting heavy-flavor jets from top-quark or W -boson decays, are

669 labeled as $t\bar{t} + \geq 1b$; those with no single- b - or b -jet but at least one single- c - or c -jet are labeled
 670 as $t\bar{t} + \geq 1c$. Finally, events not containing any heavy-flavor jets aside from those from top-quark
 671 or W -boson decays are labeled as $t\bar{t}$ + light. This classification is used to define the background
 672 categories in the likelihood fit.

673 Systematic uncertainties

674 The systematic uncertainties affecting the $t\bar{t}$ + jets background modeling are summarized in Table 17.

675 The normalization of $t\bar{t}$ + light, $t\bar{t} + \geq 1c$ and $t\bar{t} + \geq 1b$ are allowed to vary freely in the fit. The
 676 normalization factors of $t\bar{t} + \geq 1c$ and $t\bar{t} + \geq 1b$ are estimated with a common parameter in the fit,
 677 because these shape are similar for each other as shown in Figure 35. Besides normalization, the
 678 $t\bar{t}$ + light, $t\bar{t} + \geq 1c$ and $t\bar{t} + \geq 1b$ processes are affected by different types of uncertainties: $t\bar{t}$ + light
 679 has additional diagrams and profits from relatively precise measurements in data; $t\bar{t} + \geq 1c$ and
 680 $t\bar{t} + \geq 1b$ can have similar or different diagrams depending on the flavor scheme used for the PDF,
 681 and different mass of the c - and b -quark contribute to additional differences between these two
 682 processes. For these reasons, all uncertainties in the $t\bar{t}$ + jets background modeling are assigned
 683 independent nuisance parameters for the $t\bar{t}$ + light, $t\bar{t} + \geq 1c$ and $t\bar{t} + \geq 1b$ processes.

684 The weights derived in Section 5.4 are varied within their statistical uncertainties. The difference
 685 between the BDT output distribution reweighted with the nominal weight factor and the one weighted
 686 with $\pm 1\sigma$ weight factor is included in the fit for each $t\bar{t}$ + jets. Therefore, 3 NPs are included as the
 687 reweighting systematics in total.

688 Systematic uncertainties on the acceptance and shapes are extracted from the comparison between
 689 the nominal and different MC samples and settings. For ISR and FSR the settings of the nominal
 690 Powheg+Pythia sample are varied, resulting in different event weight; the uncertainty due to ISR is
 691 estimated by changing μ_r and μ_f in the ME and α_S^{ISR} in the PS, while the uncertainty due to FSR is
 692 estimated by changing α_S^{FSR} in the PS. For the ISR, the amount of radiation is increased (decreased)
 693 by scaling μ_r and μ_f by a factor 0.5 (2.0) and by using the Var3cUp (Var3cDown) variation from the
 694 A14 tune [38], corresponding to $\alpha_S^{\text{ISR}} = 0.140(0.115)$ instead of the nominal $\alpha_S^{\text{ISR}} = 0.127$. For the
 695 FSR, the amount of radiation is increased (decreased) varying μ_r for QCD emission in the FSR by a
 696 factor of 0.5 (2.0), corresponding to $\alpha_S^{\text{FSR}} = 0.1423(0.1147)$ instead of the nominal $\alpha_S^{\text{FSR}} = 0.127$.
 697 The nominal Powheg+Pythia sample is compared to the Powheg+Herwig sample to access the effect
 698 of the PS and hadronisation models, and to the MG5_aMC sample to access the effect of the NLO
 699 matching technique.

Uncertainty source	Description	Components
$t\bar{t}$ + light normalization	Free-floating	$t\bar{t}$ + light
$t\bar{t}+ \geq 1c/b$ normalization	Free-floating	$t\bar{t}+ \geq 1c$ and $t\bar{t}+ \geq 1b$
$t\bar{t}$ + jets reweighting	Statistical uncertainties of weights	All $t\bar{t}$ + jets
NLO matching	MG5_aMC+Pythia	vs. Powheg+Pythia
PS & hadronisation	Powheg+Herwig	vs. Powheg+Pythia
α_S^{ISR}	$Var3cUp$ ($Var3cDown$)	in Powheg+Pythia
μ_f	scaling by 0.5 (2.0)	in Powheg+Pythia
μ_r	scaling by 0.5 (2.0)	in Powheg+Pythia
FSR	Varying α_S^{FSR} (PS)	in Powheg+Pythia

Table 17: Summary of the sources of systematic uncertainty for $t\bar{t}$ + jets modeling. The systematic uncertainties listed in the second section of the table are evaluated in such a way to have no impact on the normalization of the three, $t\bar{t}$ + light, $t\bar{t}+ \geq 1c$ and $t\bar{t}+ \geq 1b$ components in the phase-space selected in the analysis. The last column of the table indicates the $t\bar{t}$ + jets components to which a systematic uncertainty is assigned. All systematic uncertainty sources are treated as uncorrelated across the three components.

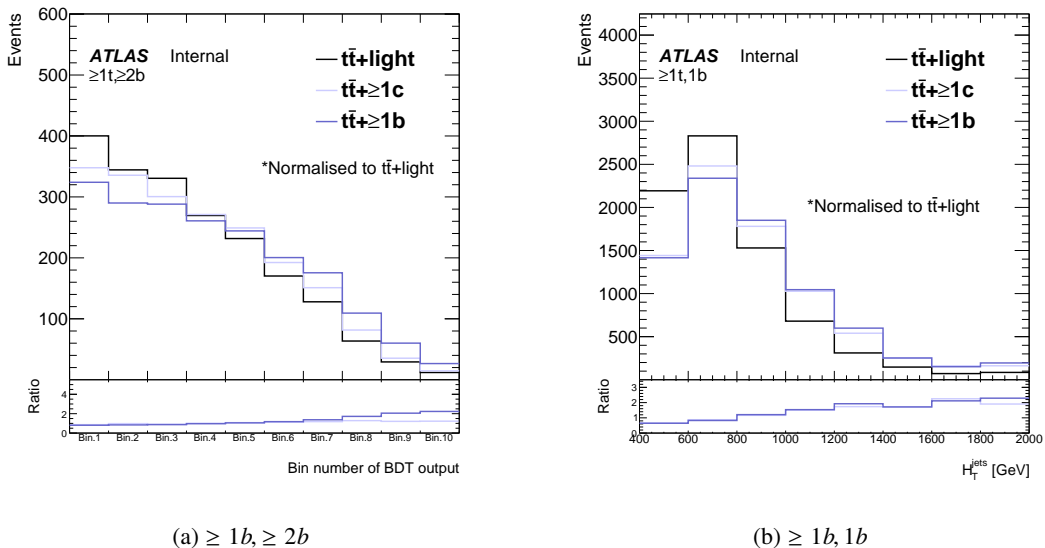


Figure 35: BDT output distribution in SR for the 1000 GeV H^+ mass hypothesis (left) and H_T^{jets} distribution in CR (right). Distributions of $t\bar{t}+ \geq 1b$ and $t\bar{t}+ \geq 1b$ are normalized to $t\bar{t}$ + light. And the ratio to $t\bar{t}$ + light are computed for $t\bar{t}+ \geq 1b$ and $t\bar{t}+ \geq 1b$.

700 6.4.2 Other backgrounds

701 The predicted $t\bar{t}H$ signal cross-section uncertainty is $^{+5.8\%}_{-9.2\%}$ (QCD scale) $\pm 3.6\%$ (PDF + α_S) [106–111].
 702 These two components are treated as uncorrelated in the fit. The effect of QCD scale and PDF variations
 703 on the shape of the distributions is found to be negligible. Uncertainties in the Higgs-boson branching
 704 fractions are also considered; these amount to 2.2% for the $b\bar{b}$ decay mode [106]. Uncertainties associated
 705 to the modeling of $t\bar{t}H$ by the Powheg+Pythia sample are also considered, for a total of four independent

706 components. The uncertainty due to ISR is estimated by simultaneously changing μ_f and μ_r in the ME and
 707 α_S^{ISR} in the PS, while the uncertainty due to ISR is estimated by changing α_S^{FSR} in the PS. For the ISR and
 708 FSR, the amount of radiation is varied following the same procedure as for $t\bar{t}$. The nominal Powheg+Pythia
 709 sample is compared to the Powheg+Herwig sample to access the uncertainty due to PS and hadronization,
 710 and to the MG5_aMC+Phythia sample for the uncertainty due to the NLO matching.

711 A $\pm 5\%$ uncertainty is considered for the cross-sections of the three single-top production modes [112–116].
 712 Uncertainties associated with the PS and hadronisation model, and with the NLO matching scheme are
 713 evaluated by comparing, for each process, the nominal Powheg+Pythia sample to a sample produced using
 714 Powheg+Herwig and MG5_aMC+Pythia, respectively. The uncertainty associated to the interference
 715 between Wt and $t\bar{t}$ production at NLO [58] is assessed by comparing the nominal Powheg+Pythia sample
 716 produced using the "diagram removal" scheme to an alternative sample produced with the same generator
 717 but using the "diagram subtraction" scheme.

718 The uncertainty of the $t\bar{t}V$ NLO cross-section prediction is 15% [117, 118], split into PDF and scale
 719 uncertainties as for $t\bar{t}H$. An additional $t\bar{t}V$ modeling uncertainty, related to the choice of PS and
 720 hadronisation model and NLO matching scheme is assessed by comparing the nominal MG5_aMC+Pythia
 721 samples with alternative ones generated with Sherpa.

722 A total 50% normalization uncertainty is considered for the 4 tops background, covering effects from
 723 varying μ_f and μ_r , PDFs and α_S [34, 119]. The small backgrounds from tZq and tWH are each assigned
 724 cross-section uncertainties: $\pm 7.9\%$ and $\pm 0.9\%$ for tZq , accounting for μ_f and μ_r variations, and for PDFs,
 725 respectively, and $\pm 50\%$ for tWZ [34].

726 An uncertainty of 40% is assumed for the $W +$ jets cross-section, with an additional 30% normalization
 727 uncertainty used for $W +$ heavy-flavor jets, taken as uncorrelated between events with two and more than
 728 two heavy-flavor jets. These uncertainties are based on variations of the μ_f and μ_r and of the matching
 729 parameters in the Sherpa samples. An uncertainty of 35% is then applied to the $Z +$ jets normalization,
 730 uncorrelated across jet bins, to account for both the variations of the scales and matching parameters in the
 731 Sherpa samples and the uncertainty in the extraction from data of the correction factor for the heavy-flavor
 732 component. Finally, a total 50% normalization uncertainty in the diboson background is assumed, which
 733 includes uncertainties in the inclusive cross-section and additional jet production [120].

7 Profile Likelihood Fit (Without reweighting)

7.1 Method

In order to test for the presence of an $H^+ \rightarrow tb$ ($W' \rightarrow tb$) signal, a binned maximum-likelihood fit to the data is performed simultaneously in all analysis regions, and each mass hypothesis is tested separately. The input to the fit is the BDT distribution for the SR and H_T^{jets} distribution for the CR. Two initially unconstrained fit parameters are used to model the normalization of the $t\bar{t}$ + light and $t\bar{t} + \geq 1$ HF jets background. The procedures used to quantify the level of agreement with the background-only or background-plus-signal hypothesis, and to determine exclusion limits, are based on the profile likelihood ratio test and the CL_s method. The parameter of interest is the signal strength, μ .

To estimate the signal strength, a likelihood function, $\mathcal{L}(\mu, \theta)$, is constructed as the product of Poisson probability terms. One Poisson term is included for every bin of the BDT and H_T^{jets} distribution in the analysis regions. Binning of BDT output distribution is defined by an automatic binning algorithm, *TransfoD*, implemented in TRexFitter [93]. The expected number of events in the Poisson terms is a function of μ , and a set of nuisance parameters, θ . The nuisance parameters encode effects from the normalization of backgrounds, including two free normalization factors for the $t\bar{t}$ + light and $t\bar{t} + \geq 1$ HF jets backgrounds, the systematic uncertainties and one parameter per bin to model statistical uncertainties in the simulated samples. All nuisance parameters are constrained with Gaussian or log-normal terms. There are about 400 nuisance parameters considered in the fit, the number varying slightly across the range of mass hypotheses.

To extract the exclusion limit on μ , the following test statistic is used:

$$\tilde{t}_\mu = \begin{cases} -2 \ln \frac{\mathcal{L}(\mu, \hat{\theta}(\mu))}{\mathcal{L}(0, \hat{\theta}(0))} & \mu < 0 \\ -2 \ln \frac{\mathcal{L}(\mu, \hat{\theta}(\mu))}{\mathcal{L}(\hat{\mu}, \hat{\theta})} & \mu \geq 0 \end{cases} \quad (2)$$

The values of the signal strength and nuisance parameters that maximize the likelihood function are represented by $\hat{\mu}$ and $\hat{\theta}$, respectively. For a given value of μ , the values of the nuisance parameters that maximize the likelihood function are represented by $\hat{\theta}(\mu)$.

7.2 Pruning and smoothing of systematic uncertainties

In the fits, pruning is applied at the threshold of 1%, meaning that if the effect of a nuisance parameter is smaller than 1% before fitting (separately for shape and normalisation) it is excluded from the fit. This pruning procedure reduces the CPU time and helps the fit to converge. Appendix C shows the systematic uncertainties that are pruned in Asimov fits.

Smoothing is applied for systematics uncertainties on $t\bar{t}$ modeling by *MaxVariation* algorithm implemented in TRexFitter, because these uncertainties are typically computed by comparing two different MC samples, or by applying MC generator weights on a MC sample, which dilutes the MC statistics and increases the fluctuations. No smoothing is applied for modeling systematic uncertainties on small backgrounds — given their small impact on the final result — or for experimental systematics — which are obtained either by

767 applying SFs typically close to unity (e.g. b -tagging), or by using the same simulated events but with
768 different calibrations of the objects (e.g. JES).

769 **7.3 Asimov fit results**

770 In the following, the results of fits to Asimov datasets generated from simulated samples are presented.
771 Figures 36 to 51 show the nuisance parameters, normalization factors, correlation matrices, the effect of
772 the different nuisance parameters before and after the fit and post-fit plots from the fits under each H^+ mass
773 hypotheses.

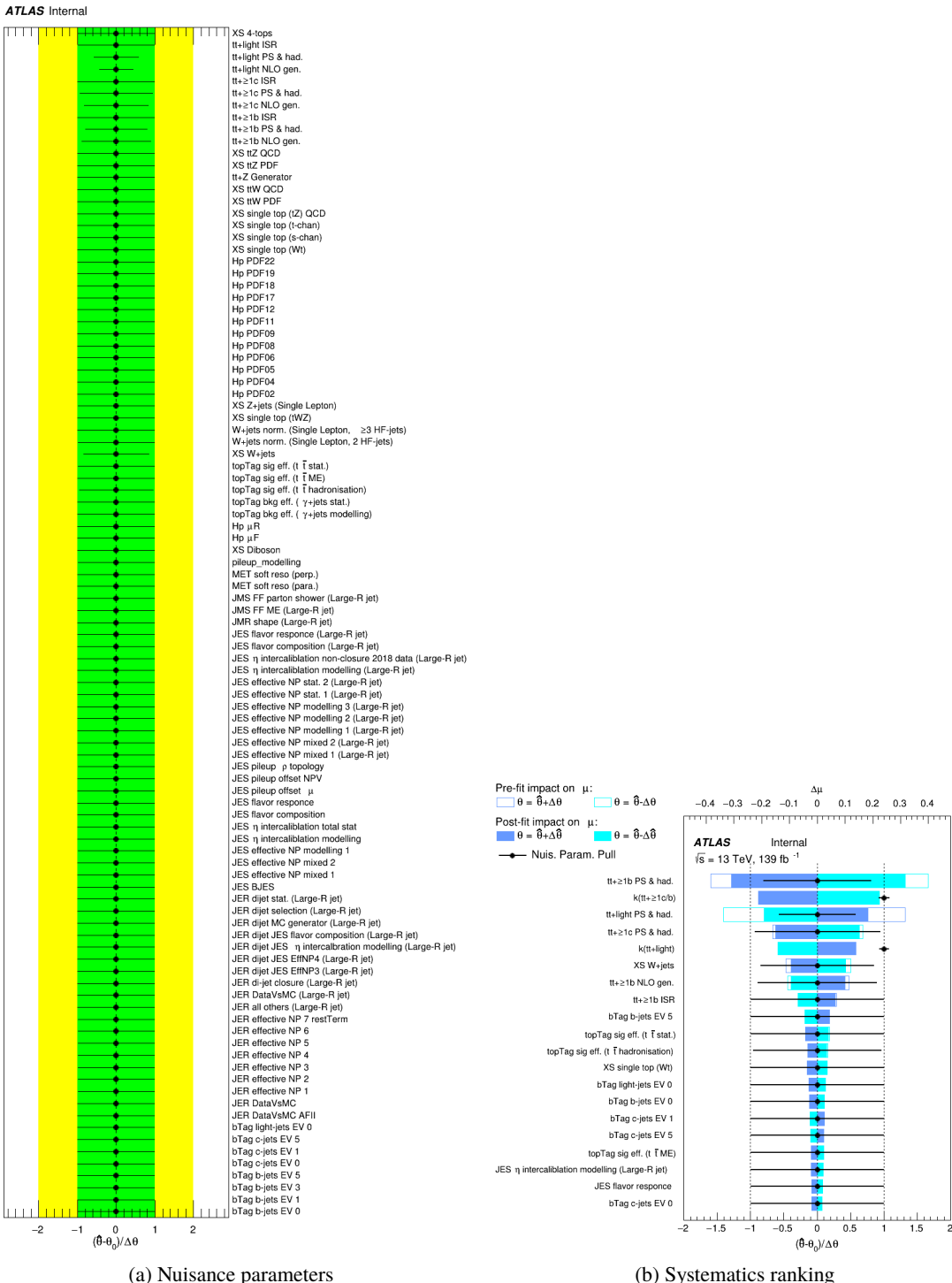


Figure 36: Nuisance parameters (left) and ranking plot (right) of the effect of various nuisance parameters before and after the fit for the 1000 GeV H^+ mass hypotheses.

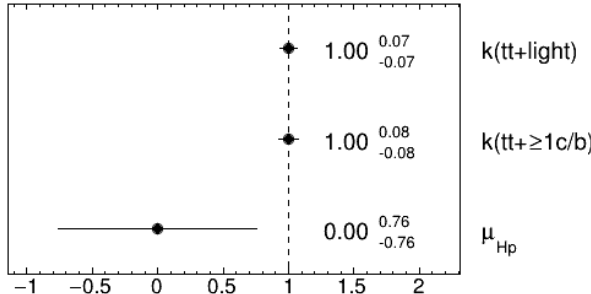
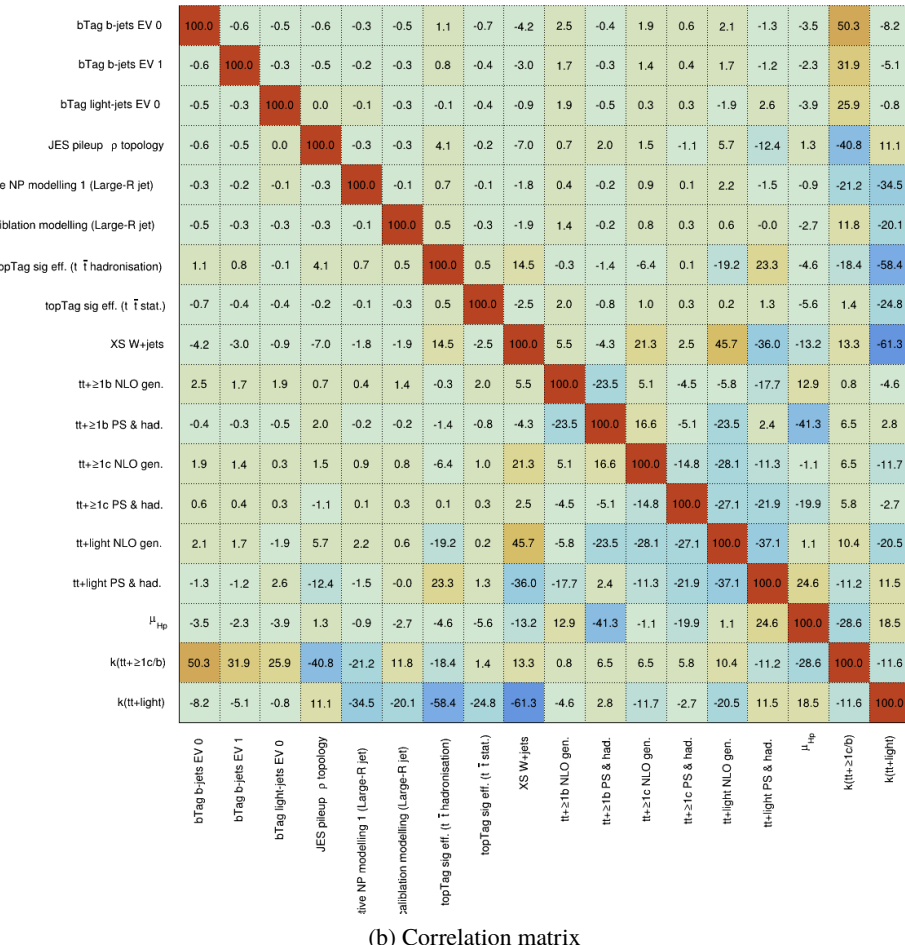
ATLAS Internal**ATLAS Internal**

Figure 37: Signal strength and normalization factors (top) and correlation matrix (bottom) for the 1000 GeV H^+ mass hypotheses.

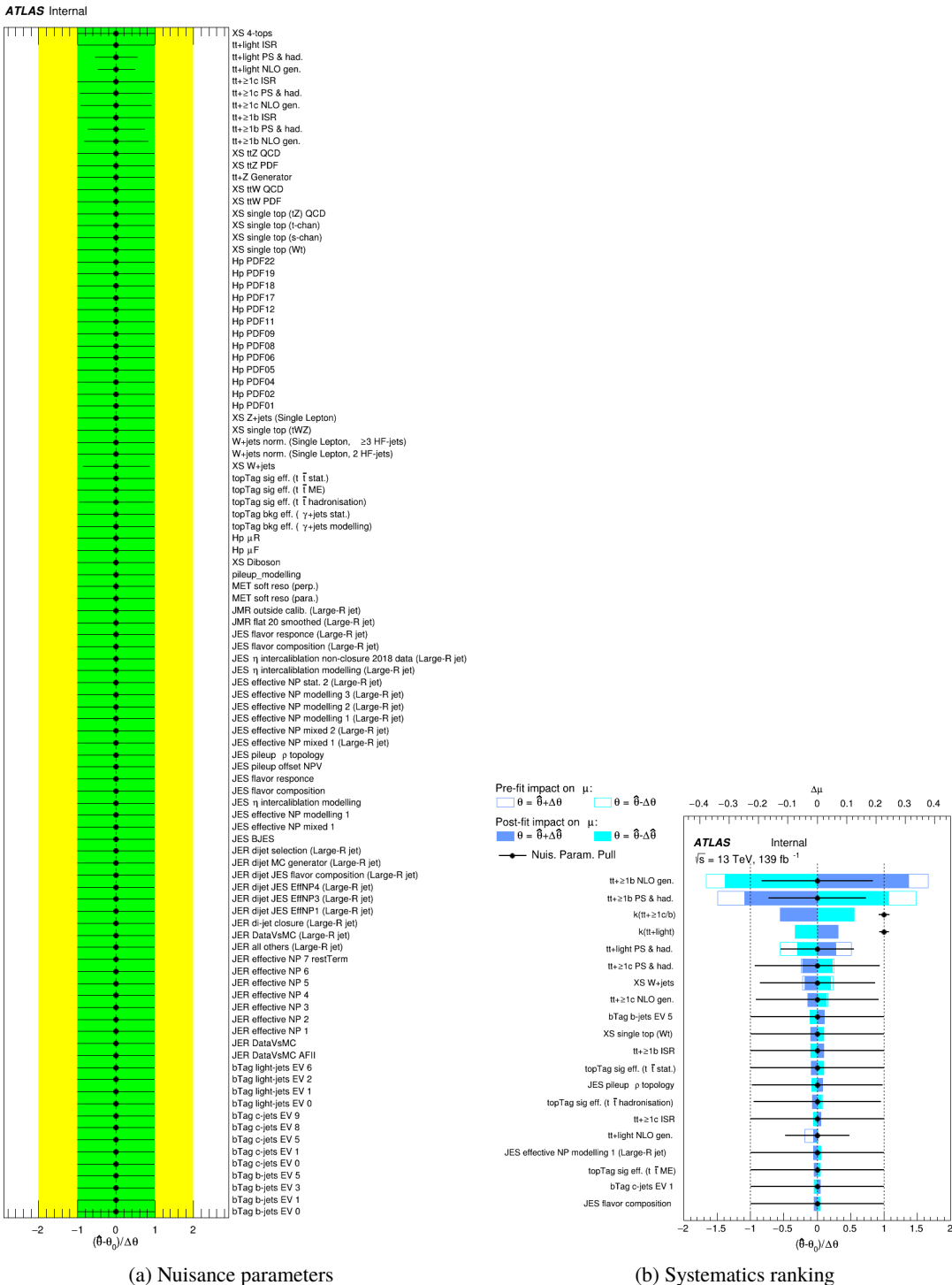
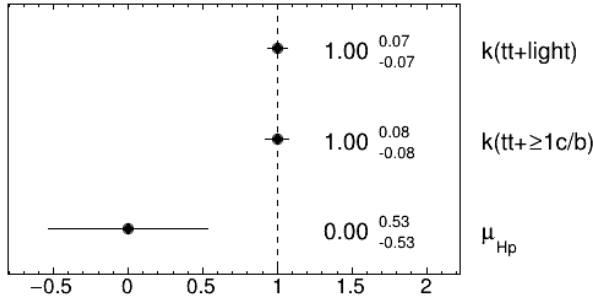


Figure 38: Nuisance parameters (left) and ranking plot (right) of the effect of various nuisance parameters before and after the fit for the 1200 GeV H^+ mass hypotheses.

ATLAS Internal

(a) Norm. factors

ATLAS Internal

	bTag b-jets EV 0	-0.4	0.0	-0.5	-0.3	-0.3	0.1	1.6	-0.4	-3.5	2.5	1.7	1.0	0.5	2.6	-2.6	-2.0	50.6	-9.0
bTag b-jets EV 1	-0.4	100.0	0.0	-0.4	-0.2	-0.2	0.0	1.1	-0.2	-2.5	1.6	1.0	0.7	0.4	2.2	-2.2	-1.1	32.1	-5.6
bTag light-jets EV 0	0.0	0.0	100.0	0.0	0.0	0.0	0.0	-0.1	0.0	0.5	0.3	1.6	0.6	0.0	-0.6	-1.2	1.6	25.7	-2.0
JES pileup p topology	-0.5	-0.4	0.0	100.0	-0.3	-0.2	-0.2	4.4	-0.1	-6.8	-0.3	0.6	1.6	-0.1	4.9	-12.3	3.3	-41.2	10.7
active NP modelling 1 (Large-R jet)	-0.3	-0.2	0.0	-0.3	100.0	-0.1	0.0	0.9	-0.1	-1.8	0.8	0.3	0.3	0.2	2.1	-1.2	-2.2	-21.0	-34.3
calibration modelling (Large-R jet)	-0.3	-0.2	0.0	-0.2	-0.1	100.0	0.0	0.8	-0.2	-1.5	1.4	1.0	0.4	0.2	0.9	-0.8	-1.9	11.9	-20.4
topTag bkg eff. (γ +jets modelling)	0.1	0.0	0.0	-0.2	0.0	0.0	100.0	0.2	0.1	-0.3	-0.3	-0.0	-0.4	-0.3	-1.8	-2.2	1.8	-20.1	-1.4
topTag sig eff. ($t\bar{t}$ hadronisation)	1.6	1.1	-0.1	4.4	0.9	0.8	0.2	100.0	0.9	14.1	-8.0	-10.0	-4.9	-1.5	-15.5	16.4	-3.1	-18.5	-57.7
topTag sig eff. ($t\bar{t}$ stat.)	-0.4	-0.2	0.0	-0.1	-0.1	-0.2	0.1	0.9	100.0	-1.7	2.0	1.3	0.3	0.2	0.9	-0.0	-4.1	1.4	-25.4
XS W+jets	-3.5	-2.5	0.5	-6.8	-1.8	-1.5	-0.3	14.1	-1.7	100.0	3.1	-2.9	7.5	2.7	51.1	-38.0	-8.5	13.9	-62.2
$t\bar{t}+\geq 1$ b NLO gen.	2.5	1.6	0.3	-0.3	0.8	1.4	-0.3	-8.0	2.0	3.1	100.0	-53.6	-8.7	-4.0	4.9	-24.3	59.0	-7.0	1.8
$t\bar{t}+\geq 1$ b PS & had.	1.7	1.0	1.6	0.6	0.3	1.0	-0.0	-10.0	1.3	-2.9	-53.6	100.0	-17.0	-0.4	2.4	-10.7	-46.3	12.6	4.0
$t\bar{t}+\geq 1$ c NLO gen.	1.0	0.7	0.6	1.6	0.3	0.4	-0.4	-4.9	0.3	7.5	-8.7	-17.0	100.0	-9.0	-41.8	-11.2	-5.9	4.1	-3.0
$t\bar{t}+\geq 1$ c PS & had.	0.5	0.4	0.0	-0.1	0.2	0.2	-0.3	-1.5	0.2	2.7	-4.0	-0.4	-9.0	100.0	-27.0	-28.9	-9.8	3.2	-1.6
$t\bar{t}$ +light NLO gen.	2.6	2.2	-0.6	4.9	2.1	0.9	-1.8	-15.5	0.9	51.1	4.9	2.4	-41.8	-27.0	100.0	-29.0	-1.7	12.7	-26.8
$t\bar{t}$ +light PS & had.	-2.6	-2.2	-1.2	-12.3	-1.2	-0.8	-2.2	16.4	-0.0	-38.0	-24.3	-10.7	-11.2	-28.9	-29.0	100.0	12.5	-10.5	17.1
μ_{H_p}	-2.0	-1.1	1.6	3.3	-2.2	-1.9	1.8	-3.1	-4.1	-8.5	59.0	-46.3	-5.9	-9.8	-1.7	12.5	100.0	-23.8	14.0
$k(t\bar{t}+\geq 1$ c/b)	50.6	32.1	25.7	-41.2	-21.0	11.9	-20.1	-18.5	1.4	13.9	-7.0	12.6	4.1	3.2	12.7	-10.5	-23.8	100.0	-12.0
$k(t\bar{t}$ +light)	-9.0	-5.6	-2.0	10.7	-34.3	-20.4	-1.4	-57.7	-25.4	-62.2	1.8	4.0	-3.0	-1.6	-26.8	17.1	14.0	-12.0	100.0

(b) Correlation matrix

Figure 39: Signal strength and normalization factors (top) and correlation matrix (bottom) for the 1200 GeV H^+ mass hypotheses.

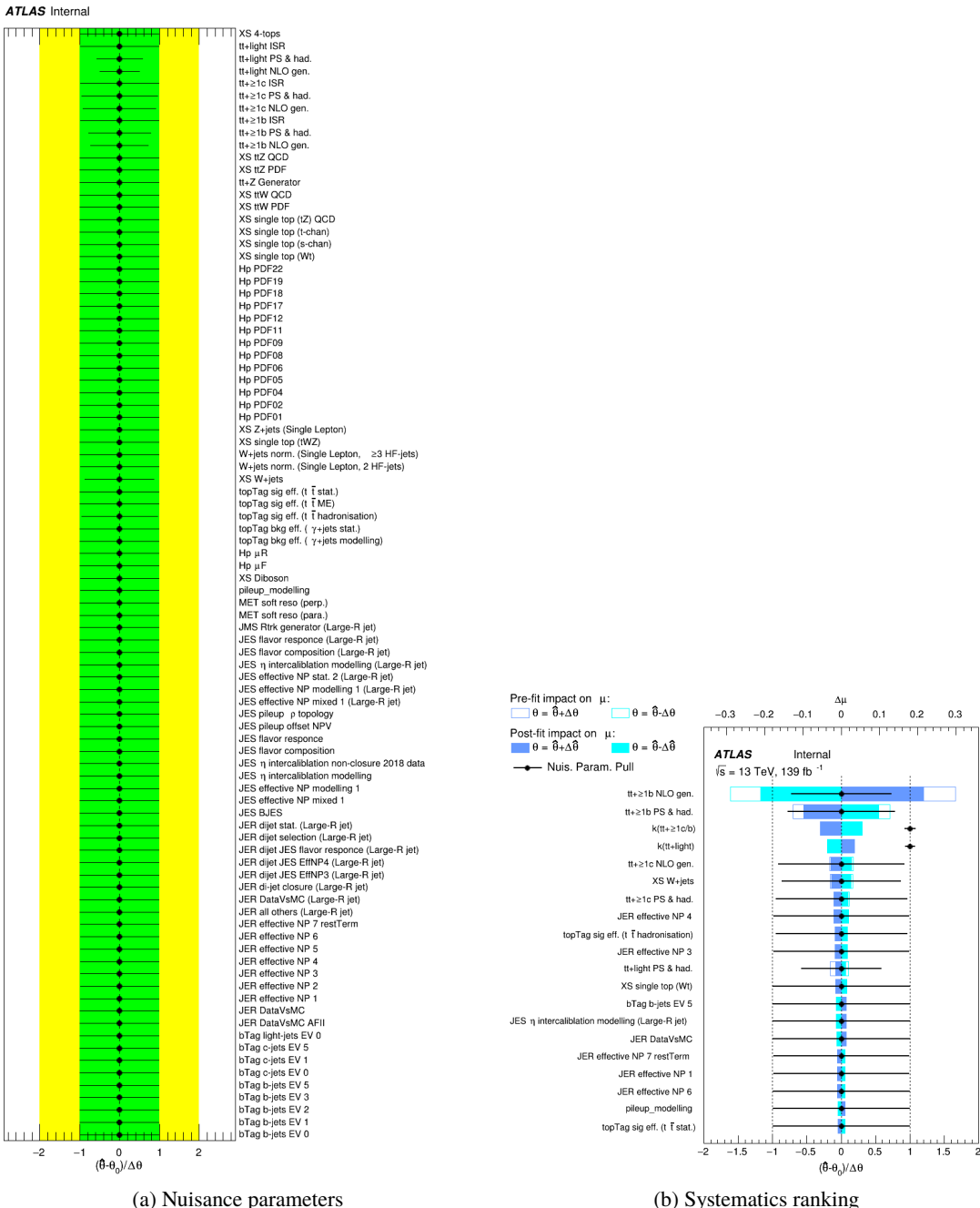
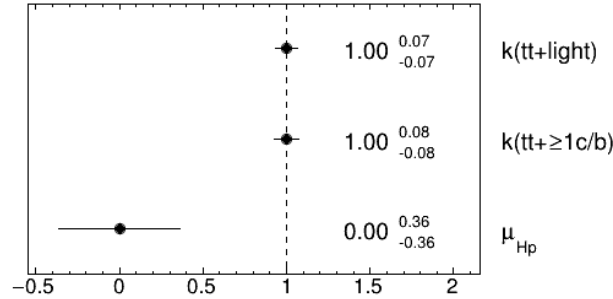


Figure 40: Nuisance parameters (left) and ranking plot (right) of the effect of various nuisance parameters before and after the fit for the 1400 GeV H^+ mass hypotheses.

ATLAS Internal

(a) Norm. factors

ATLAS Internal

	bTag b-jets EV 0	-0.2	-0.0	-0.5	-0.2	-0.1	0.1	1.3	-0.2	-2.5	2.7	1.6	1.0	0.1	3.6	-4.5	-0.4	51.4	-9.5
bTag b-jets EV 1	-0.2	100.0	-0.0	-0.4	-0.1	-0.1	0.0	1.0	-0.1	-1.9	1.7	1.0	0.7	0.1	2.8	-3.3	0.1	32.6	-6.0
bTag light-jets EV 0	-0.0	-0.0	100.0	0.1	0.0	-0.1	-0.1	-0.2	0.0	0.5	-0.5	1.0	0.5	0.0	-0.3	-1.2	0.7	26.2	-1.9
JES pileup p topology	-0.5	-0.4	0.1	100.0	-0.3	-0.2	-0.1	4.3	-0.2	-7.3	-1.2	-0.8	0.3	-0.9	5.4	-11.1	1.3	-41.4	11.0
active NP modelling 1 (Large-R jet)	-0.2	-0.1	0.0	-0.3	100.0	-0.0	0.0	0.7	-0.1	-1.5	0.9	0.1	0.3	-0.1	2.4	-1.9	-1.6	-21.4	-34.3
calibration modelling (Large-R jet)	-0.1	-0.1	-0.1	-0.2	-0.0	100.0	-0.0	0.8	-0.0	-0.4	1.4	3.3	0.9	0.3	1.4	-1.4	3.5	11.5	-21.0
topTag bkg eff. (γ +jets modelling)	0.1	0.0	-0.1	-0.1	0.0	-0.0	100.0	-0.2	0.1	-0.2	-3.4	-0.7	-0.2	-0.6	-1.1	-3.5	2.2	-20.3	-1.3
topTag sig eff. ($t\bar{t}$ hadronisation)	1.3	1.0	-0.2	4.3	0.7	0.8	-0.2	100.0	0.7	13.0	-9.2	-7.9	-3.4	-0.4	-17.4	17.4	-4.3	-19.1	-56.7
topTag sig eff. ($t\bar{t}$ stat.)	-0.2	-0.1	0.0	-0.2	-0.1	-0.0	0.1	0.7	100.0	-1.1	2.7	1.0	0.4	-0.0	1.4	-1.4	-2.5	1.3	-25.6
XS W+jets	-2.5	-1.9	0.5	-7.3	-1.5	-0.4	-0.2	13.0	-1.1	100.0	-0.2	-5.5	6.2	-0.2	52.0	-42.4	-7.2	14.9	-62.7
tt+≥1b NLO gen.	2.7	1.7	-0.5	-1.2	0.9	1.4	-3.4	-9.2	2.7	-0.2	100.0	-52.6	-7.6	-5.6	3.1	-25.4	59.0	-3.1	3.3
tt+≥1b PS & had.	1.6	1.0	1.0	-0.8	0.1	3.3	-0.7	-7.9	1.0	-5.5	-52.6	100.0	-14.7	-4.8	-4.0	-5.9	-27.2	7.3	5.1
tt+≥1c NLO gen.	1.0	0.7	0.5	0.3	0.3	0.9	-0.2	-3.4	0.4	6.2	-7.6	-14.7	100.0	-7.1	-43.0	-5.0	-7.7	4.1	-3.2
tt+≥1c PS & had.	0.1	0.1	0.0	-0.9	-0.1	0.3	-0.6	-0.4	-0.0	-0.2	-5.6	-4.8	-7.1	100.0	-30.5	-21.3	-5.4	1.4	0.1
tt+light NLO gen.	3.6	2.8	-0.3	5.4	2.4	1.4	-1.1	-17.4	1.4	52.0	3.1	-4.0	-43.0	-30.5	100.0	-38.9	-1.6	13.9	-27.1
tt+light PS & had.	-4.5	-3.3	-1.2	-11.1	-1.9	-1.4	-3.5	17.4	-1.4	-42.4	-25.4	-5.9	-5.0	-21.3	-38.9	100.0	-3.7	-10.5	20.5
μ_{H_p}	-0.4	0.1	0.7	1.3	-1.6	3.5	2.2	-4.3	-2.5	-7.2	59.0	-27.2	-7.7	-5.4	-1.6	-3.7	100.0	-15.3	9.9
$k(\text{tt+}\geq 1\text{c/b})$	51.4	32.6	26.2	-41.4	-21.4	11.5	-20.3	-19.1	1.3	14.9	-3.1	7.3	4.1	1.4	13.9	-10.5	-15.3	100.0	-11.8
$k(\text{tt+light})$	-9.5	-6.0	-1.9	11.0	-34.3	-21.0	-1.3	-66.7	-25.6	-62.7	3.3	5.1	-3.2	0.1	-27.1	20.5	9.9	-11.8	100.0

(b) Correlation matrix

Figure 41: Signal strength and normalization factors (top) and correlation matrix (bottom) for the 1400 GeV H^+ mass hypotheses.

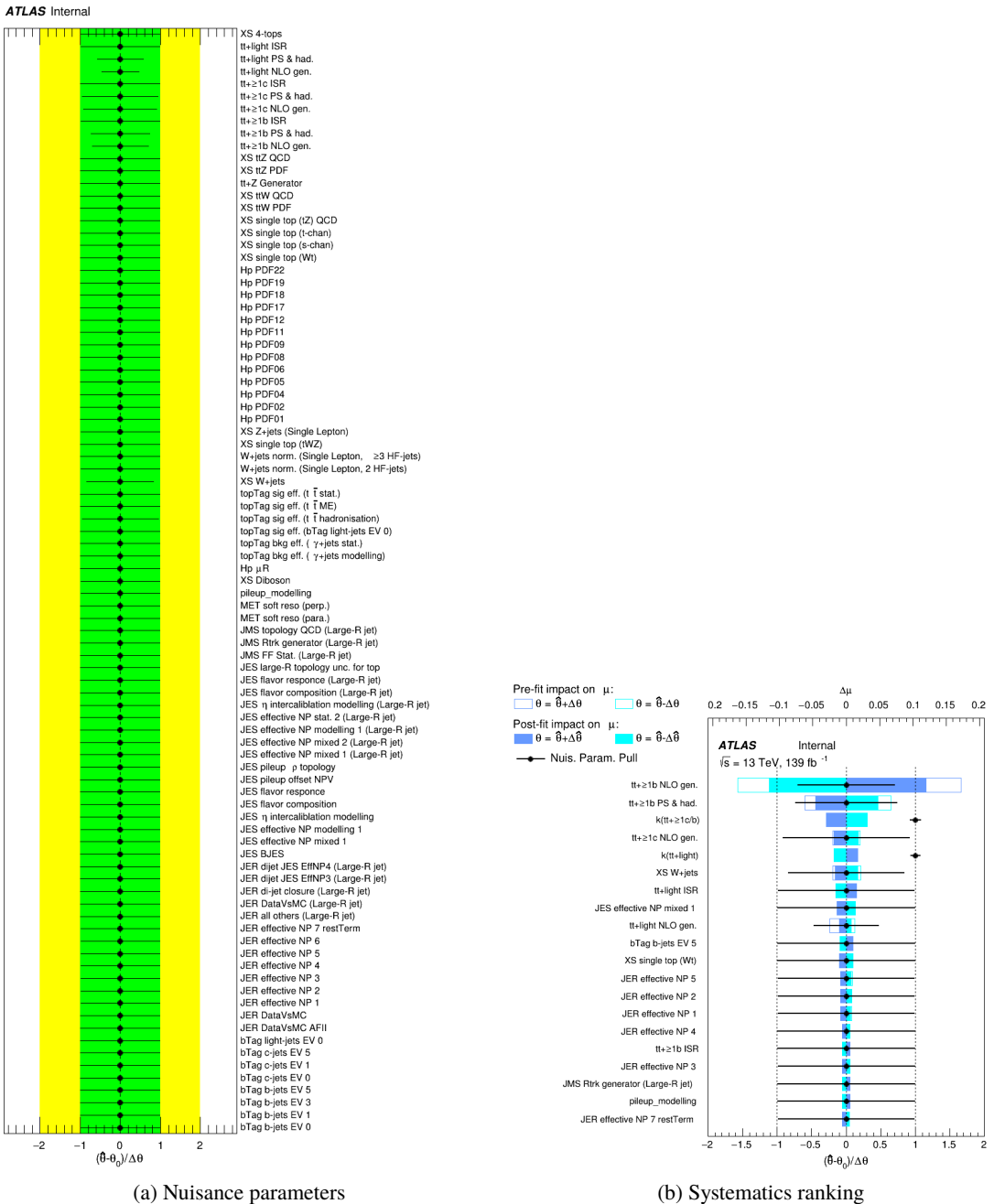


Figure 42: Nuisance parameters (left) and ranking plot (right) of the effect of various nuisance parameters before and after the fit for the 1600 GeV H^+ mass hypotheses.

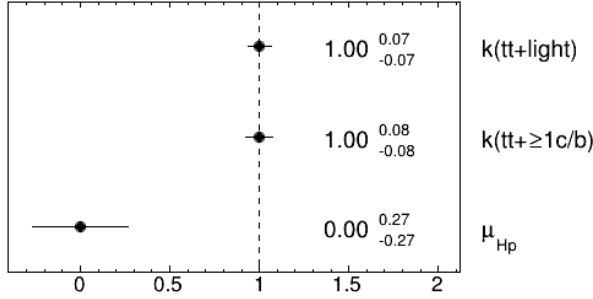
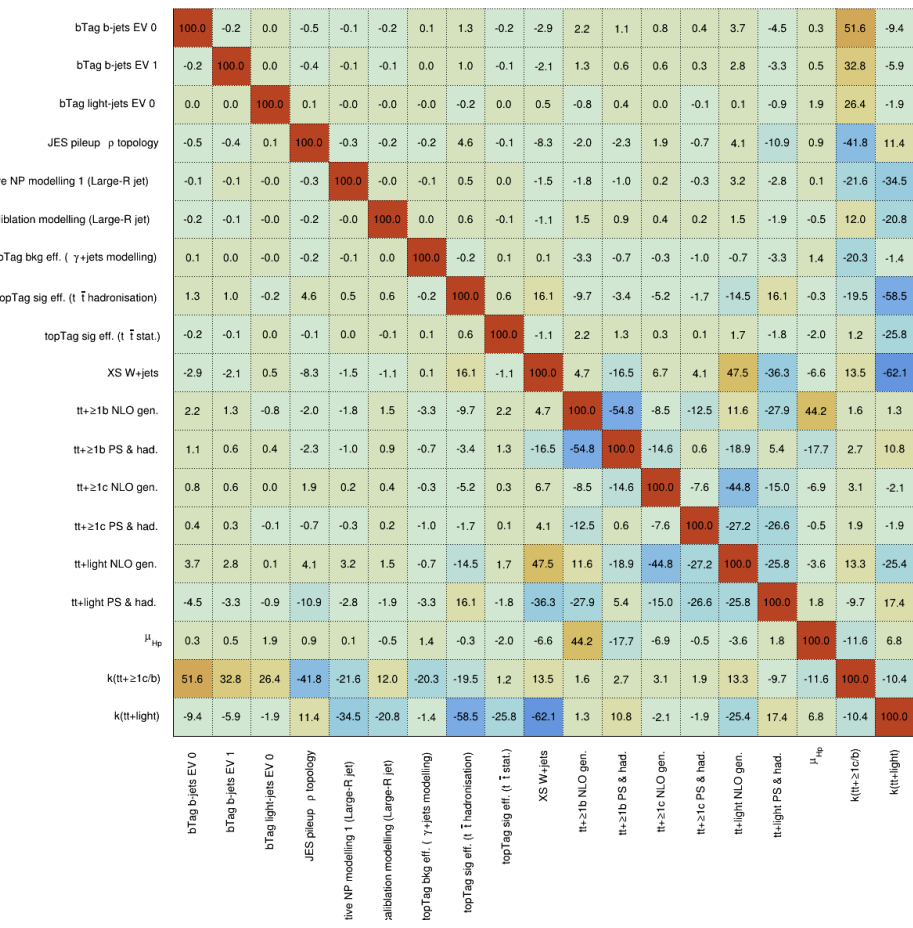
ATLAS Internal**ATLAS Internal****(b) Correlation matrix**

Figure 43: Signal strength and normalization factors (top) and correlation matrix (bottom) for the 1600 GeV H^+ mass hypotheses.

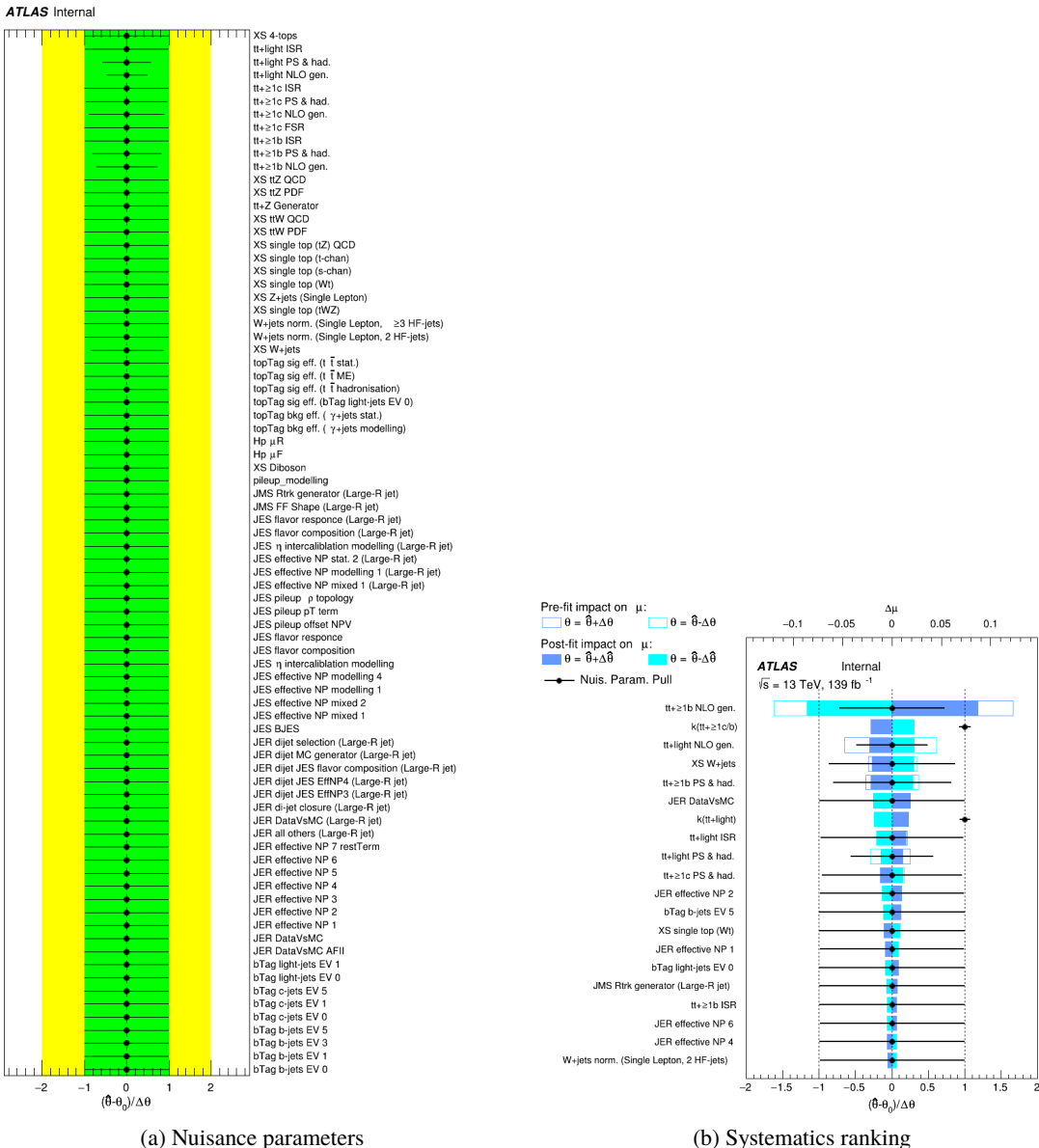
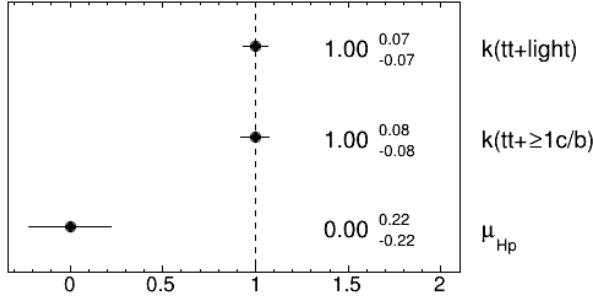
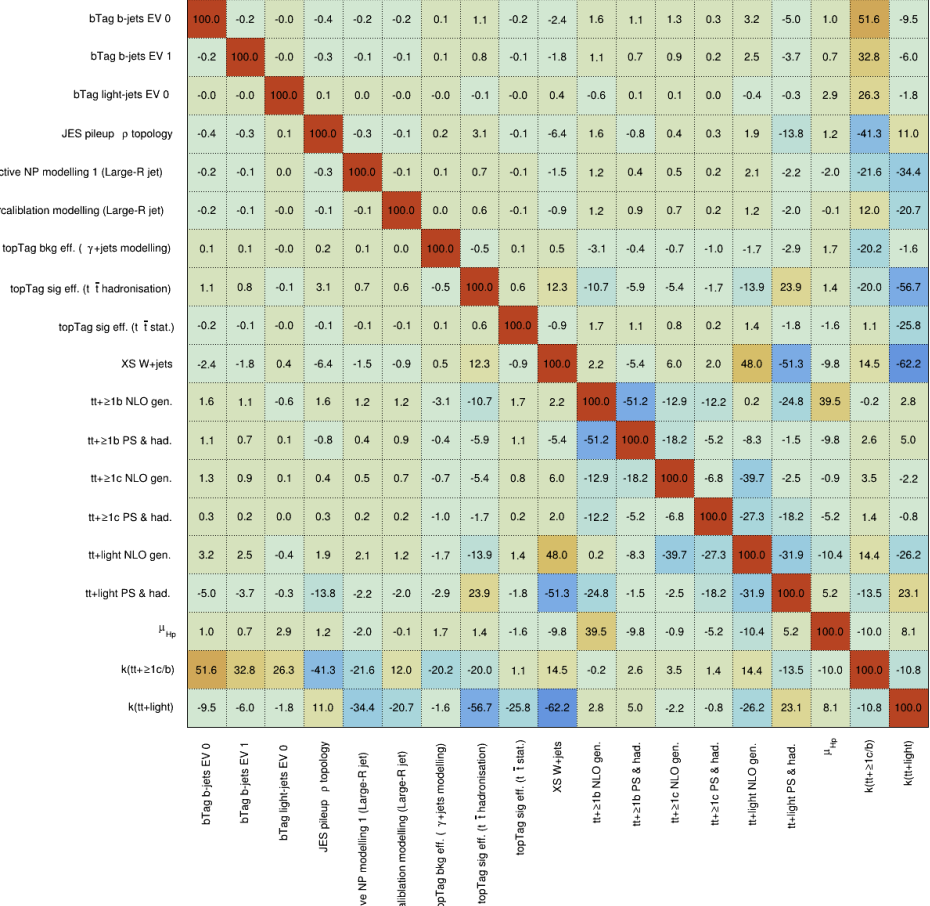


Figure 44: Nuisance parameters (left) and ranking plot (right) of the effect of various nuisance parameters before and after the fit for the 1800 GeV H^+ mass hypotheses.

ATLAS Internal

(a) Norm. factors

ATLAS Internal

(b) Correlation matrix

Figure 45: Signal strength and normalization factors (top) and correlation matrix (bottom) for the 1800 GeV H^+ mass hypotheses.

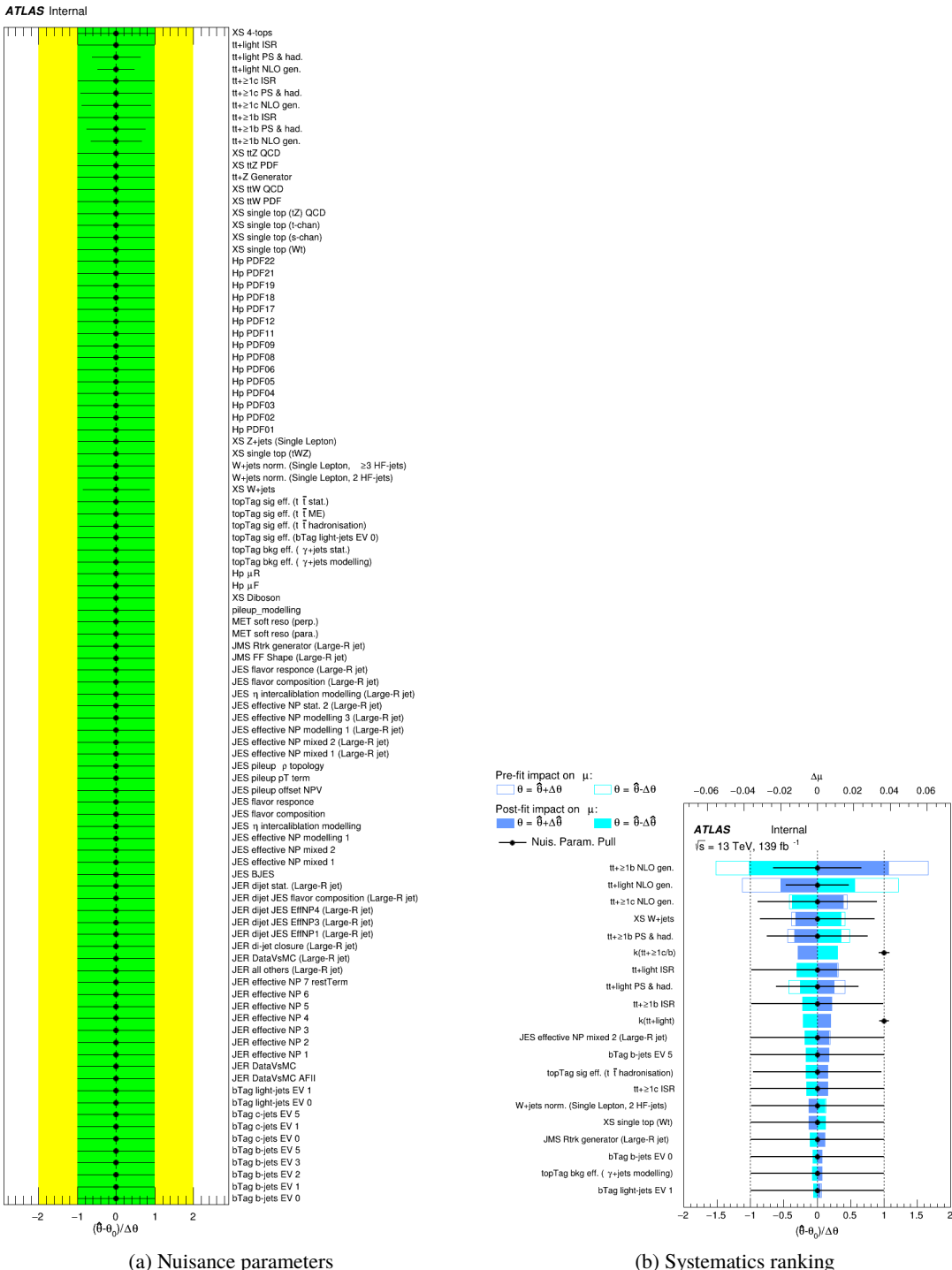
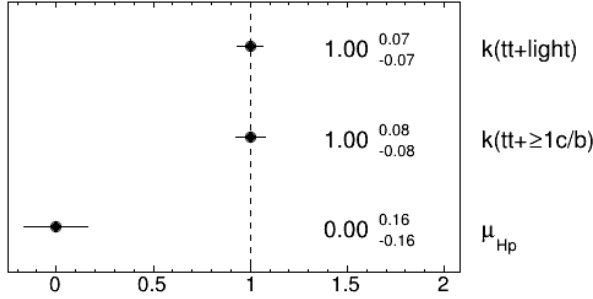


Figure 46: Nuisance parameters (left) and ranking plot (right) of the effect of various nuisance parameters before and after the fit for the 2000 GeV H^+ mass hypotheses.

ATLAS Internal

(a) Norm. factors

ATLAS Internal

	bTag b-jets EV 0	-0.2	-0.1	-0.5	-0.1	-0.1	-0.0	1.2	-0.2	-2.5	0.7	1.3	1.0	0.1	4.2	-4.6	1.5	51.8	-9.5
bTag b-jets EV 1	-0.2	100.0	-0.0	-0.4	-0.1	-0.1	-0.0	0.9	-0.1	-1.9	0.5	0.7	0.7	0.1	3.2	-3.3	0.9	32.9	-6.0
bTag light-jets EV 0	-0.1	-0.0	100.0	0.2	0.0	-0.0	0.0	-0.1	-0.1	0.6	1.3	2.1	-0.1	-0.1	-0.1	-0.3	0.8	26.5	-2.0
JES pileup p topology	-0.5	-0.4	0.2	100.0	-0.3	-0.2	-0.0	4.3	-0.2	-8.0	-0.0	-2.1	1.7	-0.8	4.3	-11.0	-1.0	-41.7	11.5
active NP modelling 1 (Large-R jet)	-0.1	-0.1	0.0	-0.3	100.0	-0.0	0.0	0.7	-0.0	-1.6	0.6	-0.1	0.7	0.1	2.3	-2.0	-1.1	-21.7	-34.4
calibration modelling (Large-R jet)	-0.1	-0.1	-0.0	-0.2	-0.0	100.0	0.0	0.5	-0.1	-1.0	0.9	0.9	0.5	0.1	1.6	-1.9	0.0	12.0	-20.7
topTag bkg eff. (γ+jets modelling)	-0.0	-0.0	0.0	-0.0	0.0	0.0	100.0	0.0	0.0	-0.2	-3.1	-0.2	-1.4	-1.2	-0.4	-2.6	1.6	-20.5	-1.4
topTag sig eff. (t̄hadronisation)	1.2	0.9	-0.1	4.3	0.7	0.5	0.0	100.0	0.6	13.8	-6.4	-3.8	-3.6	1.0	-19.1	19.4	3.6	-20.3	-57.3
topTag sig eff. (t̄stat.)	-0.2	-0.1	-0.1	-0.2	-0.0	-0.1	0.0	0.6	100.0	-0.9	1.4	1.2	0.5	-0.0	1.8	-1.8	-1.1	1.1	-25.8
XS W+jets	-2.5	-1.9	0.6	-8.0	-1.6	-1.0	-0.2	13.8	-0.9	100.0	-3.4	-11.7	11.4	2.0	50.1	-40.6	-7.8	14.4	-62.3
tt+≥1b NLO gen.	0.7	0.5	1.3	-0.0	0.6	0.9	-3.1	-6.4	1.4	-3.4	100.0	-63.3	-18.3	-7.0	7.2	-20.1	23.4	0.5	4.4
tt+≥1b PS & had.	1.3	0.7	2.1	-2.1	-0.1	0.9	-0.2	-3.8	1.2	-11.7	-63.3	100.0	-0.4	4.6	-22.9	-1.6	-7.9	2.0	8.1
tt+≥1c NLO gen.	1.0	0.7	-0.1	1.7	0.7	0.5	-1.4	-3.6	0.5	11.4	-18.3	-0.4	100.0	-15.4	-36.3	-8.9	8.6	2.5	-6.1
tt+≥1c PS & had.	0.1	0.1	-0.1	-0.8	0.1	0.1	-1.2	1.0	-0.0	2.0	-7.0	4.6	-15.4	100.0	-26.3	-17.2	-0.5	0.6	-1.9
tt+light NLO gen.	4.2	3.2	-0.1	4.3	2.3	1.6	-0.4	-19.1	1.8	50.1	7.2	-22.9	-36.3	-26.3	100.0	-39.6	-12.4	15.7	-25.2
tt+light PS & had.	-4.6	-3.3	-0.3	-11.0	-2.0	-1.9	-2.6	19.4	-1.8	-40.6	-20.1	-1.6	-8.9	-17.2	-39.6	100.0	5.8	-11.4	18.5
μ_{H_p}	1.5	0.9	0.8	-1.0	-1.1	0.0	1.6	3.6	-1.1	-7.8	23.4	-7.9	8.6	-0.5	-12.4	5.8	100.0	-6.7	4.7
$k(\text{tt+}\geq 1\text{c/b})$	51.8	32.9	26.5	-41.7	-21.7	12.0	-20.5	-20.3	1.1	14.4	0.5	2.0	2.5	0.6	15.7	-11.4	-6.7	100.0	-10.5
$k(\text{tt+light})$	-9.5	-6.0	-2.0	11.5	-34.4	-20.7	-1.4	-57.3	-25.8	-62.3	4.4	8.1	-6.1	-1.9	-25.2	18.5	4.7	-10.5	100.0

(b) Correlation matrix

Figure 47: Signal strength and normalization factors (top) and correlation matrix (bottom) for the 2000 GeV H^+ mass hypotheses.

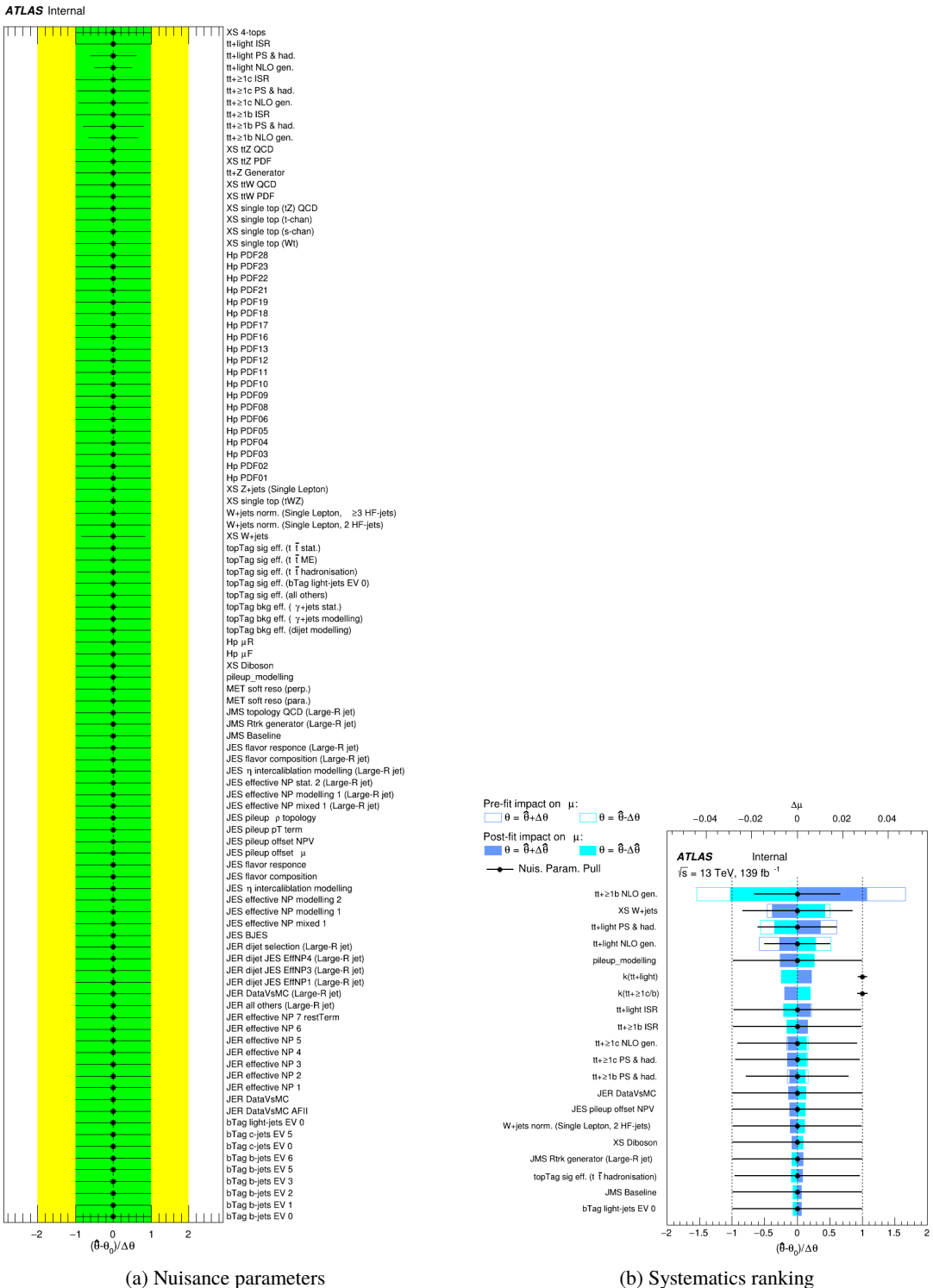
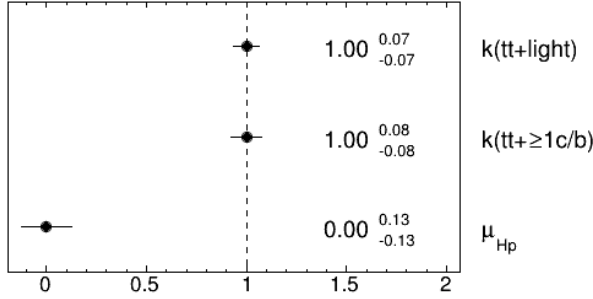


Figure 48: Nuisance parameters (left) and ranking plot (right) of the effect of various nuisance parameters before and after the fit for the 2500 GeV H^+ mass hypotheses.

ATLAS Internal**ATLAS Internal**

	bTag b-jets EV 0	-0.2	-0.1	-0.6	-0.2	-0.1	-0.0	1.2	-0.1	-2.7	0.2	0.4	0.9	0.2	4.0	-4.5	1.1	51.9	-9.5
bTag b-jets EV 1	-0.2	100.0	-0.0	-0.5	-0.1	-0.1	-0.0	0.9	-0.1	-2.0	0.1	0.2	0.6	0.1	3.0	-3.2	0.6	33.0	-6.0
bTag light-jets EV 0	-0.1	-0.0	100.0	0.0	-0.0	-0.0	0.0	-0.1	-0.0	0.1	-0.9	-0.4	0.0	0.2	-0.4	-0.5	1.4	26.5	-1.7
JES pileup p topology	-0.6	-0.5	0.0	100.0	-0.4	-0.2	-0.0	4.2	-0.2	-8.5	-0.3	-2.1	0.7	-1.5	4.6	-10.5	-1.4	-41.9	11.9
active NP modelling 1 (Large-R jet)	-0.2	-0.1	-0.0	-0.4	100.0	-0.0	0.0	0.7	-0.0	-2.1	-0.7	-1.4	0.0	-0.0	2.3	-1.6	-0.0	-21.9	-34.2
calibration modelling (Large-R jet)	-0.1	-0.1	-0.0	-0.2	-0.0	100.0	0.0	0.5	-0.1	-1.0	0.6	0.6	0.5	0.1	1.6	-1.9	0.2	12.1	-20.8
topTag bkg eff. (γ+jets modelling)	-0.0	-0.0	0.0	-0.0	0.0	0.0	100.0	0.1	0.0	-0.1	-2.5	-0.1	-0.5	-0.6	-1.1	-2.6	1.0	-20.4	-1.5
topTag sig eff. (t̄hadronisation)	1.2	0.9	-0.1	4.2	0.7	0.5	0.1	100.0	0.5	13.9	-3.7	-2.6	-3.7	0.9	-18.3	20.4	1.9	-20.2	-57.8
topTag sig eff. (t̄stat.)	-0.1	-0.1	-0.0	-0.2	-0.0	-0.1	0.0	0.5	100.0	-1.0	1.1	0.9	0.5	0.0	1.8	-1.8	-0.3	1.1	-25.9
XS W+jets	-2.7	-2.0	0.1	-8.5	-2.1	-1.0	-0.1	13.9	-1.0	100.0	-4.8	-13.2	4.5	-0.8	50.2	-37.6	-9.2	14.0	-61.6
tt+≥1b NLO gen.	0.2	0.1	-0.9	-0.3	-0.7	0.6	-2.5	-3.7	1.1	-4.8	100.0	-61.7	-18.6	-1.0	2.1	-15.6	23.7	-0.6	4.5
tt+≥1b PS & had.	0.4	0.2	-0.4	-2.1	-1.4	0.6	-0.1	-2.6	0.9	-13.2	-61.7	100.0	-16.9	-1.8	-12.7	9.2	-2.9	-0.1	9.2
tt+≥1c NLO gen.	0.9	0.6	0.0	0.7	0.0	0.5	-0.5	-3.7	0.5	4.5	-18.6	-16.9	100.0	-7.7	-43.9	-8.5	-3.3	2.5	-1.6
tt+≥1c PS & had.	0.2	0.1	0.2	-1.5	-0.0	0.1	-0.6	0.9	0.0	-0.8	-1.0	-1.8	-7.7	100.0	-32.3	-15.7	-3.3	0.8	-0.1
tt+light NLO gen.	4.0	3.0	-0.4	4.6	2.3	1.6	-1.1	-18.3	1.8	50.2	2.1	-12.7	-43.9	-32.3	100.0	-36.6	-6.3	14.6	-25.2
tt+light PS & had.	-4.5	-3.2	-0.5	-10.5	-1.6	-1.9	-2.6	20.4	-1.8	-37.6	-15.6	9.2	-8.5	-15.7	-36.6	100.0	8.0	-11.1	15.7
μ_{H_p}	1.1	0.6	1.4	-1.4	-0.0	0.2	1.0	1.9	-0.3	-9.2	23.7	-2.9	-3.3	-3.3	-6.3	8.0	100.0	-4.5	5.3
$k(t t+ \geq 1 c/b)$	51.9	33.0	26.5	-41.9	-21.9	12.1	-20.4	-20.2	1.1	14.0	-0.6	-0.1	2.5	0.8	14.6	-11.1	-4.5	100.0	-10.2
$k(t t+ light)$	-9.5	-6.0	-1.7	11.9	-34.2	-20.8	-1.5	-57.8	-25.9	-61.6	4.5	9.2	-1.6	-0.1	-25.2	15.7	5.3	-10.2	100.0

(b) Correlation matrix

Figure 49: Signal strength and normalization factors (top) and correlation matrix (bottom) for the 2500 GeV H^+ mass hypotheses.

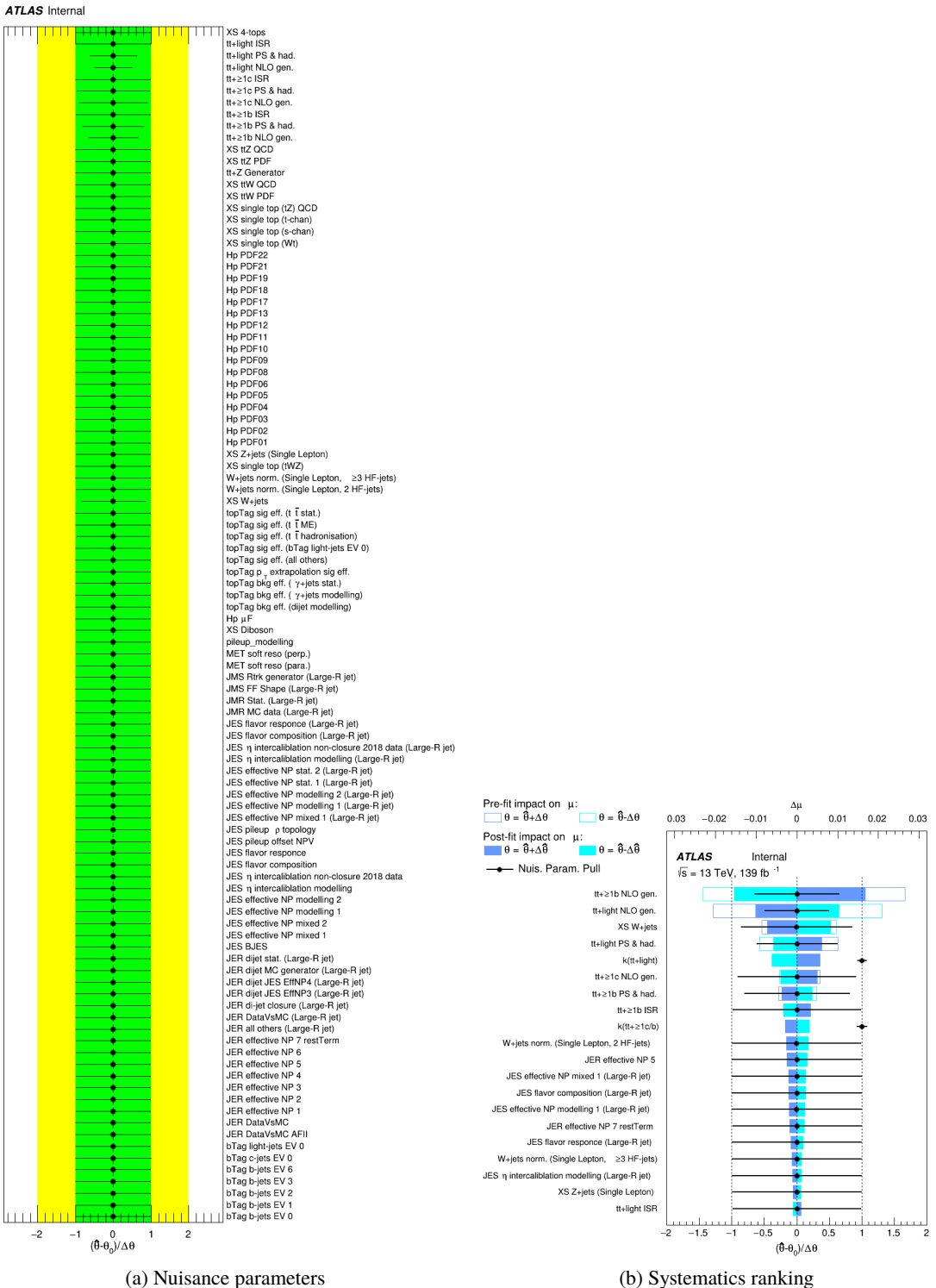
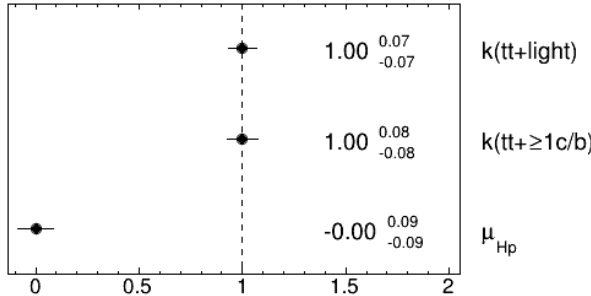


Figure 50: Nuisance parameters (left) and ranking plot (right) of the effect of various nuisance parameters before and after the fit for the 3000 GeV H^+ mass hypotheses.

ATLAS Internal

(a) Norm. factors

ATLAS Internal

	bTag b-jets EV 0	-0.2	-0.1	-0.5	-0.1	-0.1	-0.0	1.1	-0.1	-2.5	-0.8	0.6	0.8	0.3	4.1	-5.0	52.0	-9.5
bTag b-jets EV 1	-0.2	100.0	-0.0	-0.4	-0.1	-0.1	-0.0	0.9	-0.1	-2.0	-0.6	0.3	0.6	0.2	3.1	-3.5	33.0	-6.0
bTag light-jets EV 0	-0.1	-0.0	100.0	-0.0	0.0	0.0	-0.0	-0.0	-0.5	-3.5	-1.6	-0.6	0.2	-0.4	-0.6	26.5	-1.4	
JES pileup p topology	-0.5	-0.4	-0.0	100.0	-0.4	-0.2	-0.2	4.4	-0.2	-8.8	-2.7	-3.3	1.2	-1.4	4.2	-10.2	-42.0	11.9
active NP modelling 1 (Large-R jet)	-0.1	-0.1	0.0	-0.4	100.0	-0.1	-0.0	0.7	-0.1	-1.7	0.6	-0.1	0.3	-0.1	2.3	-1.8	-21.8	-34.3
calibration modelling (Large-R jet)	-0.1	-0.1	0.0	-0.2	-0.1	100.0	0.0	0.5	-0.1	-0.9	1.7	1.3	0.5	0.1	1.6	-2.0	12.2	-20.7
topTag bkg eff. ($\gamma + \text{jets}$ modelling)	-0.0	-0.0	-0.0	-0.2	-0.0	0.0	100.0	0.2	0.0	-0.6	-2.0	-1.1	-0.6	-0.7	-1.5	-2.1	-20.5	-1.2
topTag sig eff. ($t\bar{t}$ hadronisation)	1.1	0.9	-0.0	4.4	0.7	0.5	0.2	100.0	0.5	14.7	-1.1	0.4	-4.1	0.8	-17.9	19.5	-20.1	-57.8
topTag sig eff. ($t\bar{t}$ stat.)	-0.1	-0.1	-0.0	-0.2	-0.1	-0.1	0.0	0.5	100.0	-1.0	0.8	0.8	0.4	0.1	1.8	-2.0	1.1	-25.7
XS W+jets	-2.5	-2.0	-0.5	-8.8	-1.7	-0.9	-0.6	14.7	-1.0	100.0	-12.0	12.4	6.9	-0.1	50.1	-36.9	14.0	-62.4
tt+≥1b NLO gen.	-0.8	-0.6	-3.5	-2.7	0.6	1.7	-2.0	-1.1	0.8	-12.0	100.0	-60.4	-23.6	-3.2	-3.2	-5.6	-2.8	7.1
tt+≥1b PS & had.	0.6	0.3	-1.6	-3.3	-0.1	1.3	-1.1	0.4	0.8	-12.4	-60.4	100.0	-10.6	-2.3	-17.4	15.0	-0.2	6.6
tt+≥1c NLO gen.	0.8	0.6	-0.6	1.2	0.3	0.5	-0.6	-4.1	0.4	6.9	-23.6	-10.6	100.0	-8.0	-41.5	-11.7	2.1	-2.8
tt+≥1c PS & had.	0.3	0.2	0.2	-1.4	-0.1	0.1	-0.7	0.8	0.1	-0.1	-3.2	-2.3	-8.0	100.0	-31.3	-16.8	1.0	-0.6
tt+light NLO gen.	4.1	3.1	-0.4	4.2	2.3	1.6	-1.5	-17.9	1.8	50.1	-3.2	-17.4	-41.5	-31.3	100.0	-35.3	15.0	-25.5
tt+light PS & had.	-5.0	-3.5	-0.6	-10.2	-1.8	-2.0	-2.1	19.5	-2.0	-36.9	-5.6	15.0	-11.7	-16.8	-35.3	100.0	-11.5	16.0
$k_{(tt+\geq 1c/b)}$	52.0	33.0	26.5	-42.0	-21.8	12.2	-20.5	-20.1	1.1	14.0	-2.8	-0.2	2.1	1.0	15.0	-11.5	100.0	-10.3
$k_{(tt+\text{light})}$	-9.5	-6.0	-1.4	11.9	-34.3	-20.7	-1.2	-57.8	-25.7	-62.4	7.1	6.6	-2.8	-0.6	-25.5	16.0	-10.3	100.0

(b) Correlation matrix

Figure 51: Signal strength and normalization factors (top) and correlation matrix (bottom) for the 3000 GeV H^+ mass hypotheses.

774 **7.4 Post-fit plots for Asimov fit**

775 Figures 52 to 59 show the post-fit distributions of the BDT output and H_T^{jets} for the fits using Asimov
 776 dataset under all H^+ mass hypotheses.

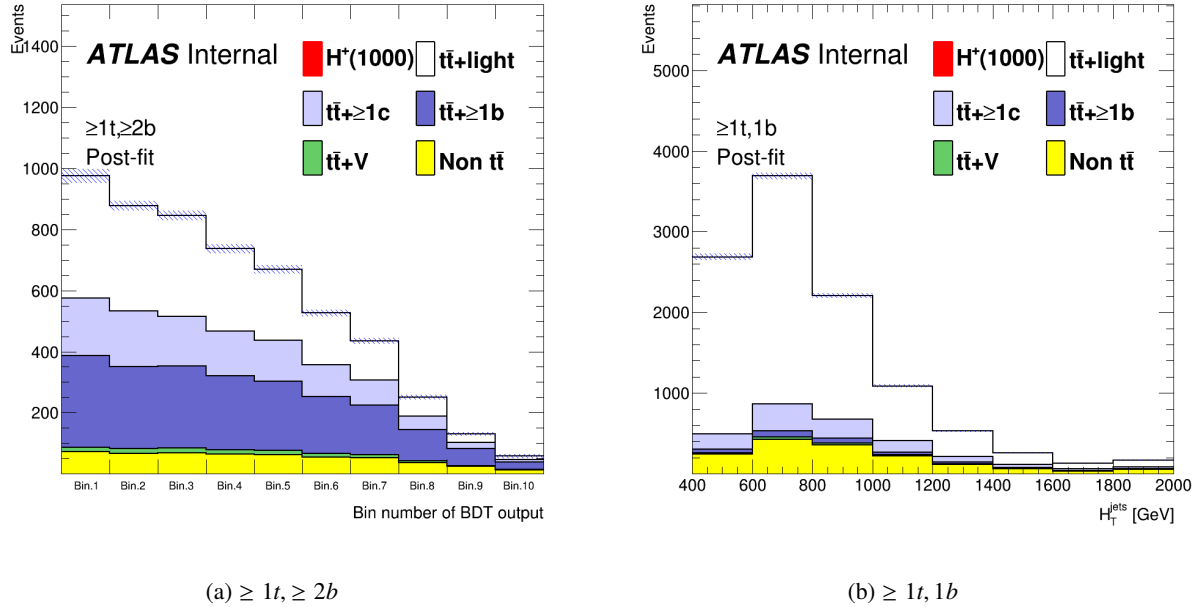


Figure 52: Post-fit distribution of BDT output and H_T^{jets} for the fits using Asimov dataset under the 1000 GeV H^+ mass hypotheses.

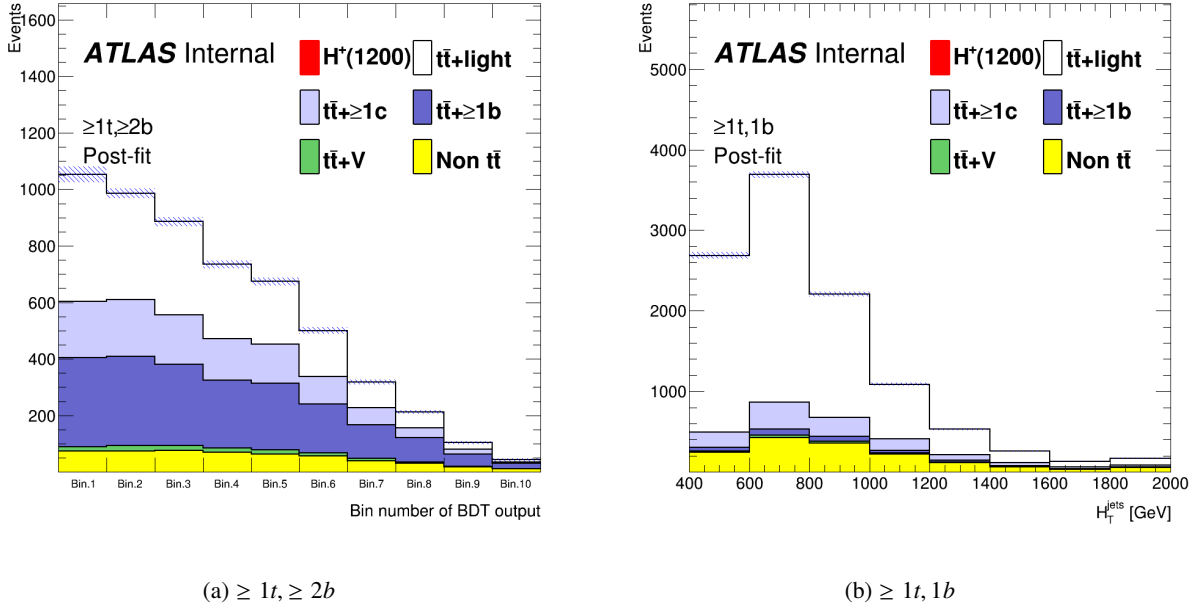


Figure 53: Post-fit distribution of BDT output and H_T^{jets} for the fits using Asimov dataset under the 1200 GeV H^+ mass hypotheses.

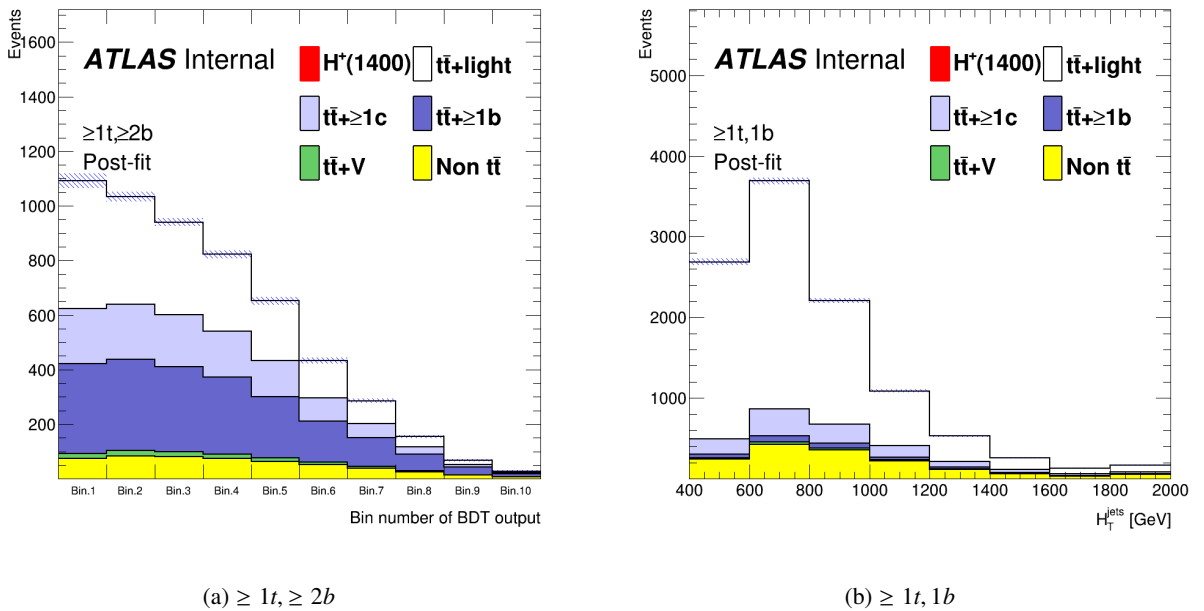


Figure 54: Post-fit distribution of BDT output and H_T^{jets} for the fits using Asimov dataset under the 1400 GeV H^+ mass hypotheses.

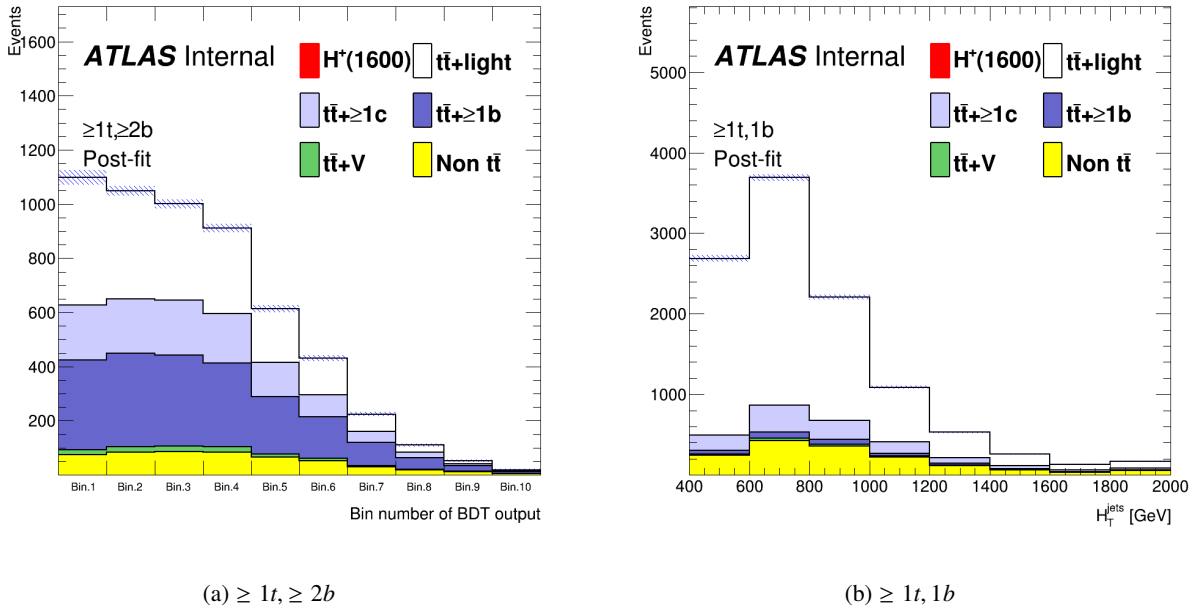


Figure 55: Post-fit distribution of BDT output and H_T^{jets} for the fits using Asimov dataset under the 1600 GeV H^+ mass hypotheses.

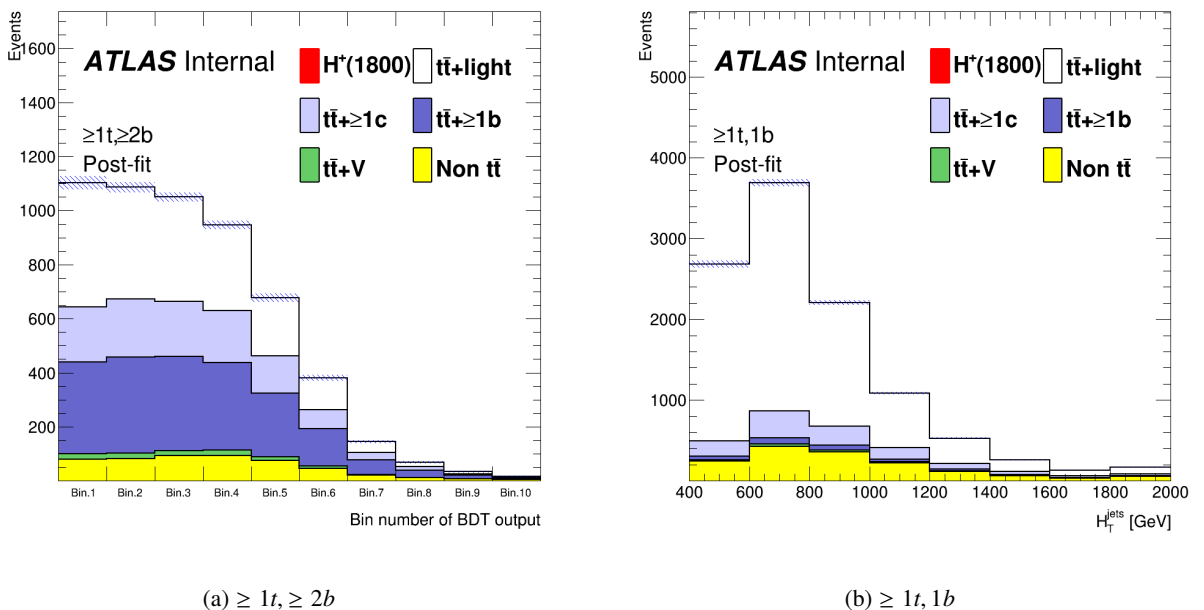


Figure 56: Post-fit distribution of BDT output and H_T^{jets} for the fits using Asimov dataset under the 1800 GeV H^+ mass hypotheses.

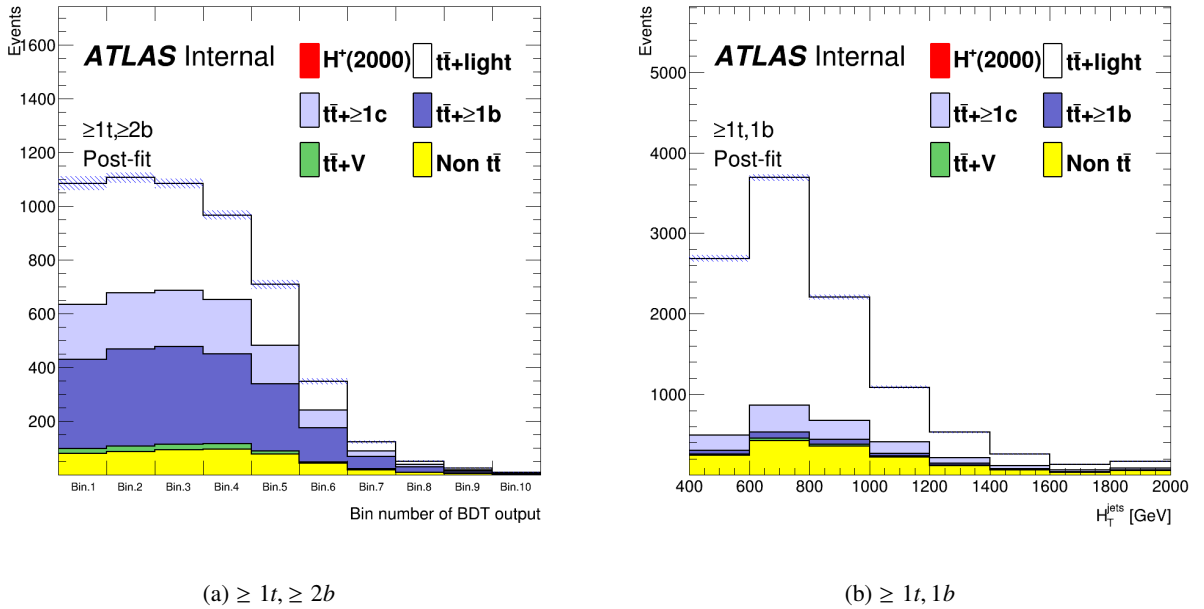


Figure 57: Post-fit distribution of BDT output and H_T^{jets} for the fits using Asimov dataset under the 2000 GeV H^+ mass hypotheses.

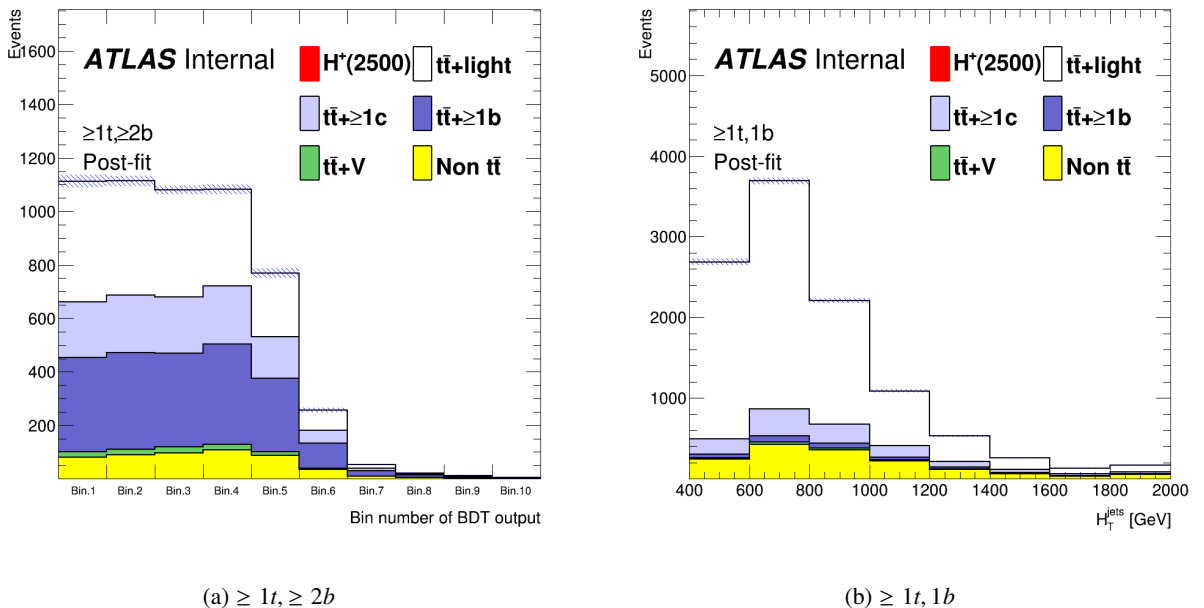


Figure 58: Post-fit distribution of BDT output and H_T^{jets} for the fits using Asimov dataset under the 2500 GeV H^+ mass hypotheses.

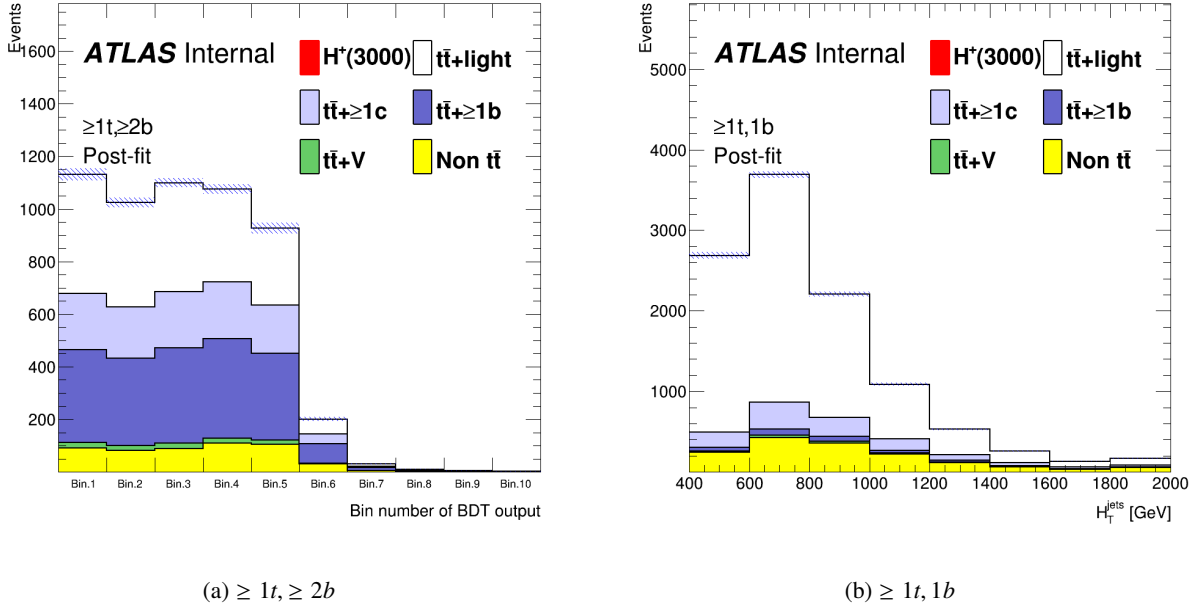


Figure 59: Post-fit distribution of BDT output and H_T^{jets} for the fits using Asimov dataset under the 3000 GeV H^+ mass hypotheses.

7.5 Asimov fit results summary

Figure 60 shows the fitted signal strength and $t\bar{t} + \text{light}$ and $t\bar{t} + \geq 1c/b$ normalisation factors as a function of the H^+ mass hypothesis of the Asimov fit.

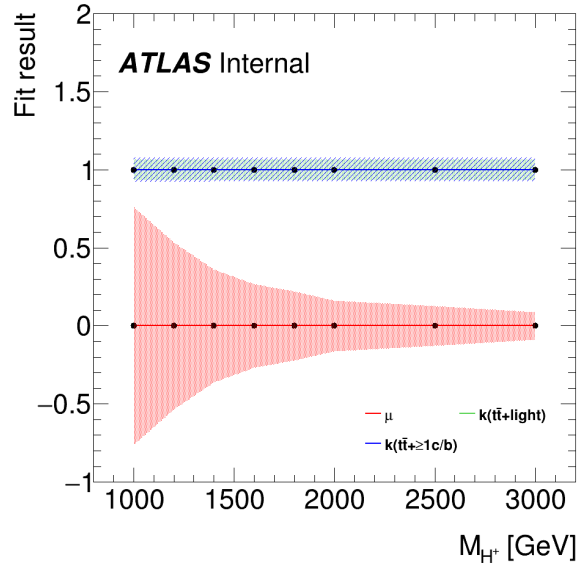


Figure 60: Fitted signal strength and $t\bar{t} + \text{light}$ and $t\bar{t} + \geq 1c/b$ normalisation factors as a function of the H^+ mass hypothesis of the Asimov fit

⁷⁸⁰ **7.6 Upper cross-section limits as a function of the H^+ mass**

⁷⁸¹ The 95% confidence level (CL) upper limit for the production of $H^+ \rightarrow tb$ in association with a top quark
⁷⁸² and a bottom quark using the CL_S method is shown in Figure 61.

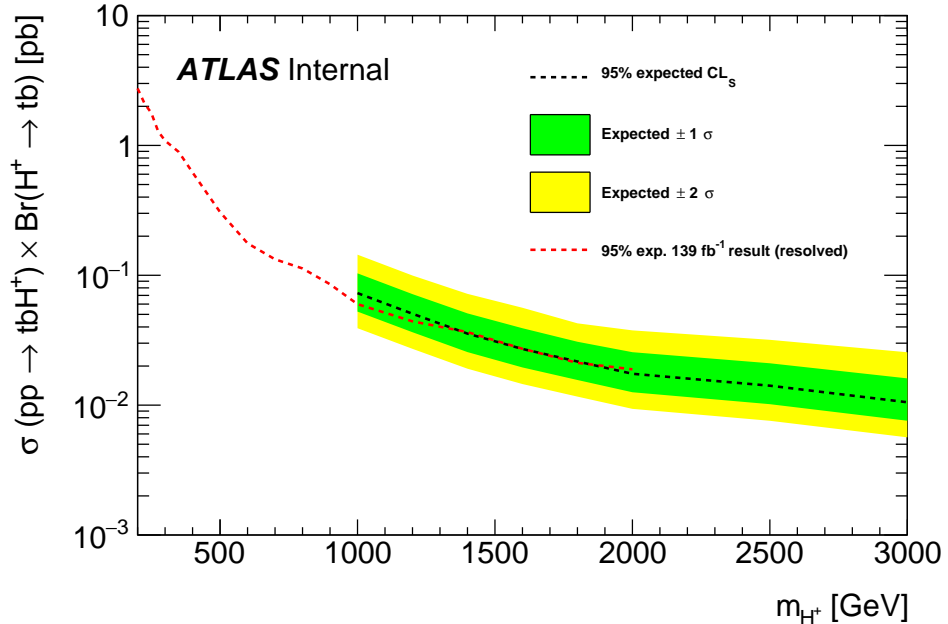


Figure 61: Expected limit for the production of $H^+ \rightarrow tb$ in association with a top quark and a bottom quark. The bands surrounding the expected limit show the 68% and 95% confidence intervals. The expected limit from ATLAS search using Run2 full data with resolved channel is also shown[24].

783 8 Test of tbW' generation

784 Motivation of this section is to check that we can apply same analysis framework to the tbW' search as tbH^+
 785 search. For that reason, we compared the kinematics of tbW' production with ones of tbH^+ production in
 786 the following sections. As result, there were no significant differences between these productions (Section
 787 8.2.3). Therefore, we continue to search tbW' production with same analysis framework as tbH^+ search.

788 8.1 tbW' MC generation in private

789 We also search for $W' \rightarrow tb$ decay with the seach of $H^+ \rightarrow tb$ decay, where W' is produced in association with
 790 tb same as H^+ production. Before the official MC generation, the private MC samples for both left-handed
 791 (LH) and right-handed (RH) W' were generated using MadGraph5_aMC@NLO. These generated test
 792 samples are summarized in Table 18.

W' mass [GeV]	Type (LH or RH)	Size (events)
1000	LH	0.1M
1000	RH	0.1M
2000	LH	0.1M
2000	RH	0.1M
3000	LH	0.1M
3000	RH	0.1M
4000	LH	0.1M
4000	RH	0.1M
5000	LH	0.1M
5000	RH	0.1M

Table 18

793 8.2 Kinematics study in truth level

794 8.2.1 Reconstructed truth objects

795 To study the kinematics properties of $W' \rightarrow tb$ events in truth level, TruthDAOD samples were produced
 796 with *TRUTH1* format [121]. The following truth objects are reconstructed according to the official ATLAS
 797 truth object definition [122]. Moreover, overlapping objects are removed as shown in Table 20.

Truth object	Collection name
Truth electron	TruthElectrons
Truth muon	TruthMuons
Truth small-R jet (j^{truth})	AntiKt4TruthDressedWZJets
Truth large-R jet (J^{truth})	AntiKt10TruthTrimmedPtFrac5SmallR20Jets

Table 19: List of reconstructed truth objects in this study. Each object is selected from the indicated collection of with their corresponding aux containers.

Reject	Against	Criteria
Truth large- R jet	Truth electron	$\Delta R < 1.0$
Truth small- R jet	Truth large- R jet	$\Delta R < 1.0$

Table 20: Summary of overlap removal procedures among truth objects

798 8.2.2 Event selection

799 To study in the same phase space as the "SR" in Section 4.1.1, events are selected according to the number
800 of truth leptons, small- R jets and large- R jets as shown in Table 21.

Cut	Criteria	
Truth leptons (ℓ^{truth})	Exactly 1 truth lepton in event	
	Truth electron	Truth muon
	$p_T > 27 \text{ GeV}$	$p_T > 27 \text{ GeV}$
	$ \eta < 1.37$ or $1.52 < \eta < 2.47$	$ \eta < 2.5$
Truth large- R jets originated from top-quark ($J_{\text{top}}^{\text{truth}}$)	≥ 1 truth large-R jets	
	$350 \text{ GeV} < p_T < 2500 \text{ GeV}$	
	$ \eta < 2.0$	
	$\Delta R(t, J_{\text{top}}^{\text{truth}}) < 1.0$ or $\Delta R(\bar{t}, J_{\text{top}}^{\text{truth}}) < 1.0$	
	(t(\bar{t}): truth particle labelled as PDG ID=6 (-6))	
Truth small- R jets originated from b -quark ($b\text{-jet}^{\text{truth}}$)	≥ 2 truth small-R jets	
	$p_T > 25 \text{ GeV}$	
	$ \eta < 2.5$	
	PDG ID of the highest-E ghost parton is 5	

Table 21: Summary of event selections in truth level.

801 8.2.3 Kinematics comparison with $t b H^+$ events

802 Variables input to BDT training in Section 4.2.3 were defined in truth level as shown in Table 22. These
803 distributions are compared between $t b W'$ and $t b H^+$ in Figure 62 to 65. These were no significant
804 differences.

Symbol	Description
Truth_HT_jets	Scalar sum of the transverse energy of leading $J_{\text{top}}^{\text{truth}}$ and all j^{truth}
Truth_LeadingJet_pt	Leading j^{truth} p_T
Truth_Mjjj_MaxPt	Invariant mass of the j^{truth} triplet with maximum p_T
Truth_Mbb_MaxPt	Invariant mass of the b -jet $^{\text{truth}}$ pair with maximum p_T
Truth_Muu_MinDR	Invariant mass of the j^{truth} -pair with minimum ΔR except for b -jet $^{\text{truth}}$
Truth_dRlepb_MindR	ΔR between ℓ^{truth} and the pair of b -jet $^{\text{truth}}$ with smallest ΔR
Truth_dRbb_avg	Average ΔR between all b -jet $^{\text{truth}}$ pairs in the event
Truth_Centrality_all	Centrality calculated using leading $J_{\text{top}}^{\text{truth}}$, all j^{truth} and ℓ^{truth}
Truth_H1_all	Second Fox-Wolfram moment calculated using all j^{truth} and ℓ^{truth}
Truth_LeadingTop_pt	Leading $J_{\text{top}}^{\text{truth}}$ p_T
Truth_LeadingTop_m	Invariant mass of leading $J_{\text{top}}^{\text{truth}}$
Truth_Pt_tb	p_T of the pair of leading $J_{\text{top}}^{\text{truth}}$ and leading b -jet $^{\text{truth}}$
Truth_M_tb	Invariant mass of the pair of leading $J_{\text{top}}^{\text{truth}}$ and leading b -jet $^{\text{truth}}$
Truth_PtAsymm_tb	p_T asymmetry between leading $J_{\text{top}}^{\text{truth}}$ and leading b -jet $^{\text{truth}}$

Table 22: Definition of variables input to BDT training in truth level.

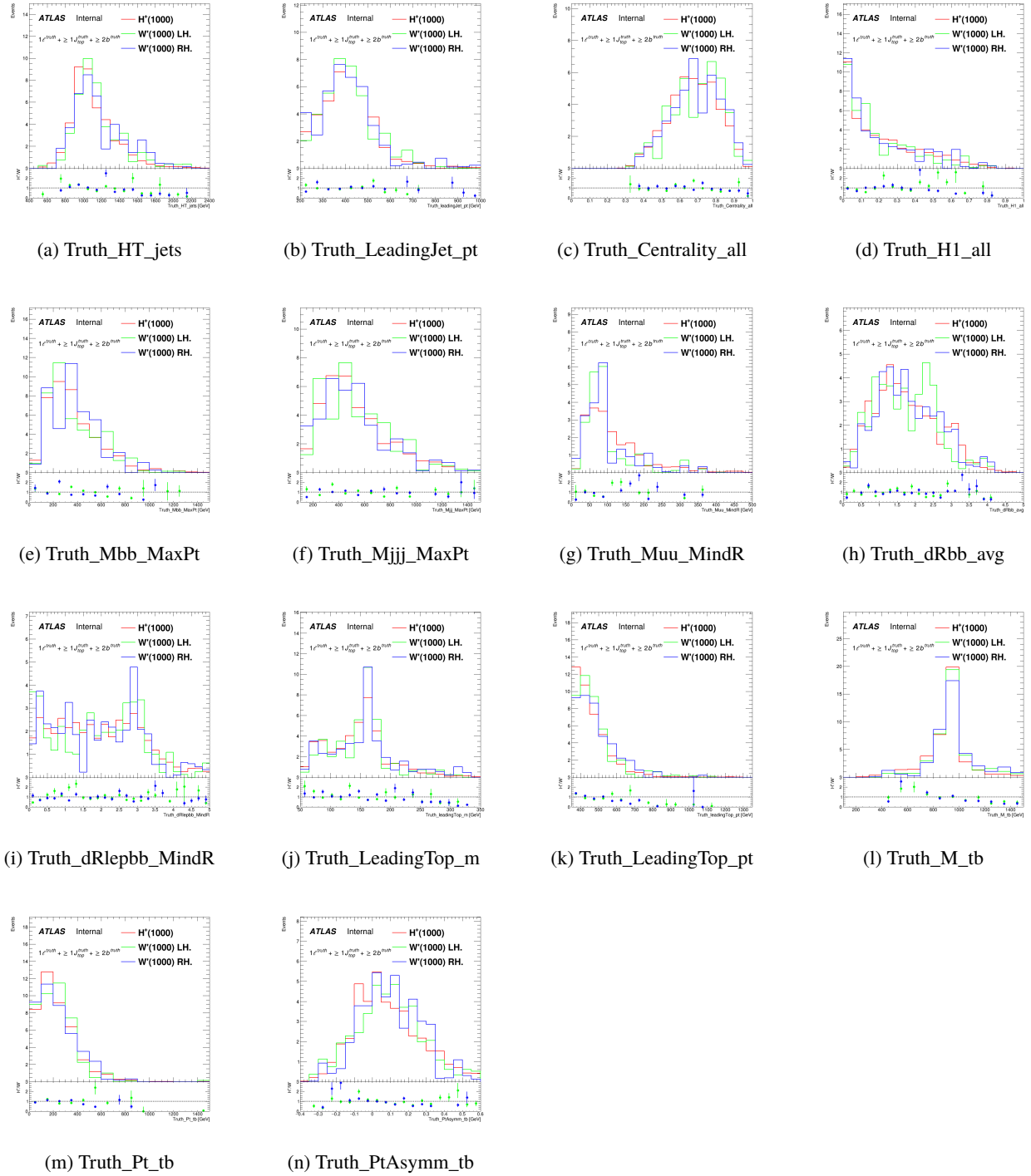


Figure 62: Comparison of the kinematic variables between tbW' and tbH^+ in truth level on 1000 GeV mass hypothesis.

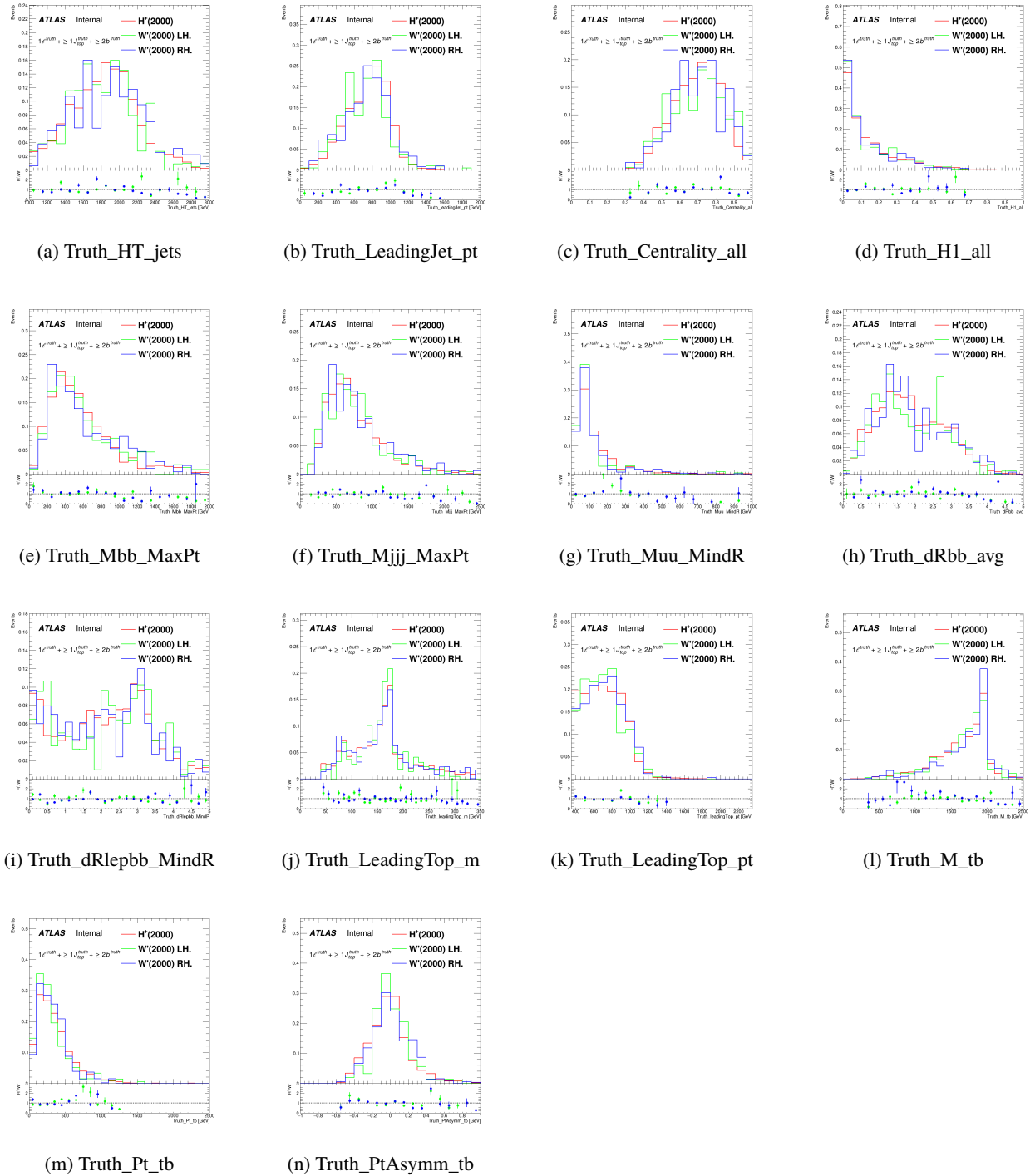


Figure 63: Comparison of the kinematic variables between tbW' and tbH^+ in truth level on 2000 GeV mass hypothesis.

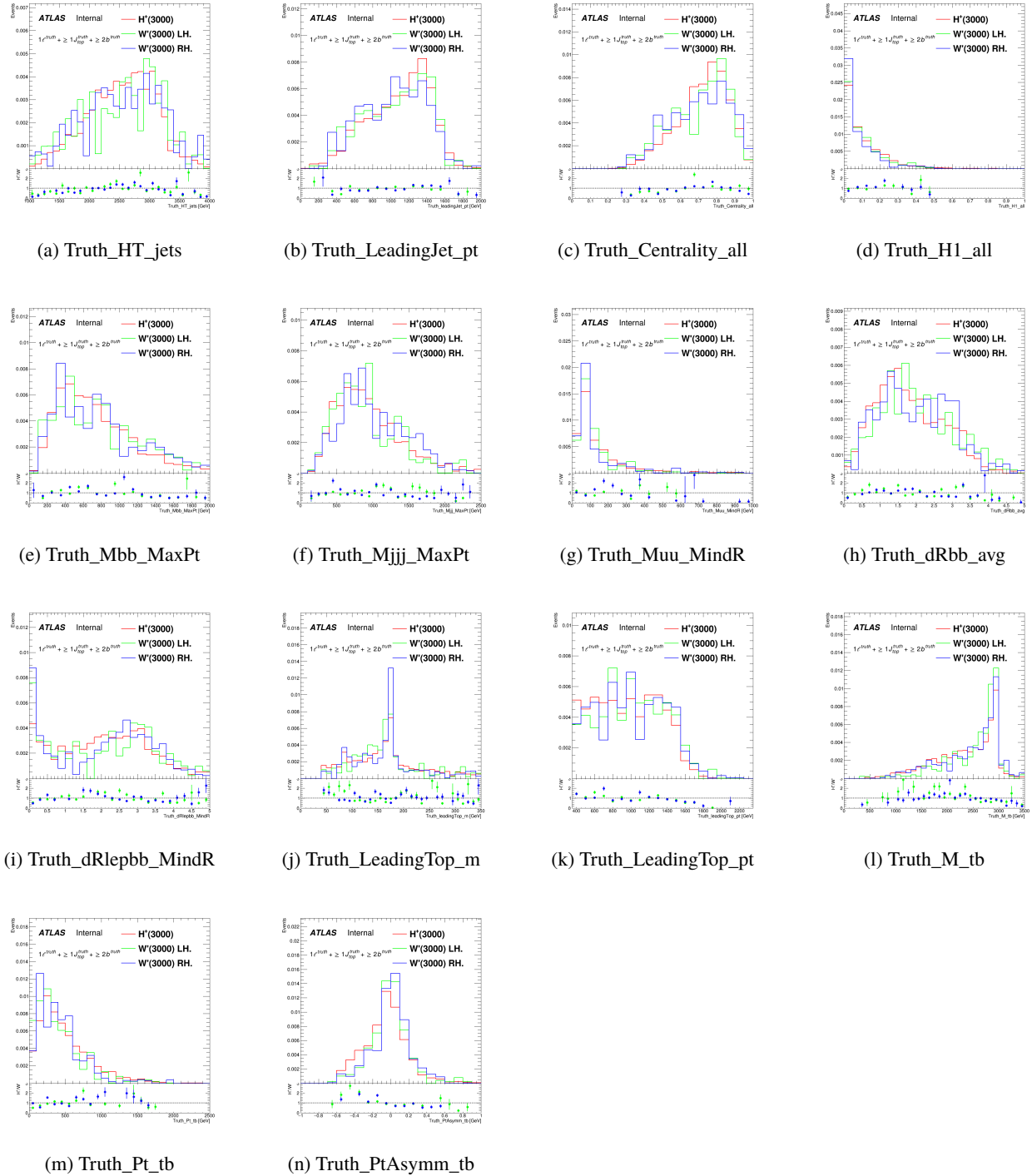


Figure 64: Comparison of the kinematic variables between tbW' and tbH^+ in truth level on 3000 GeV mass hypothesis.

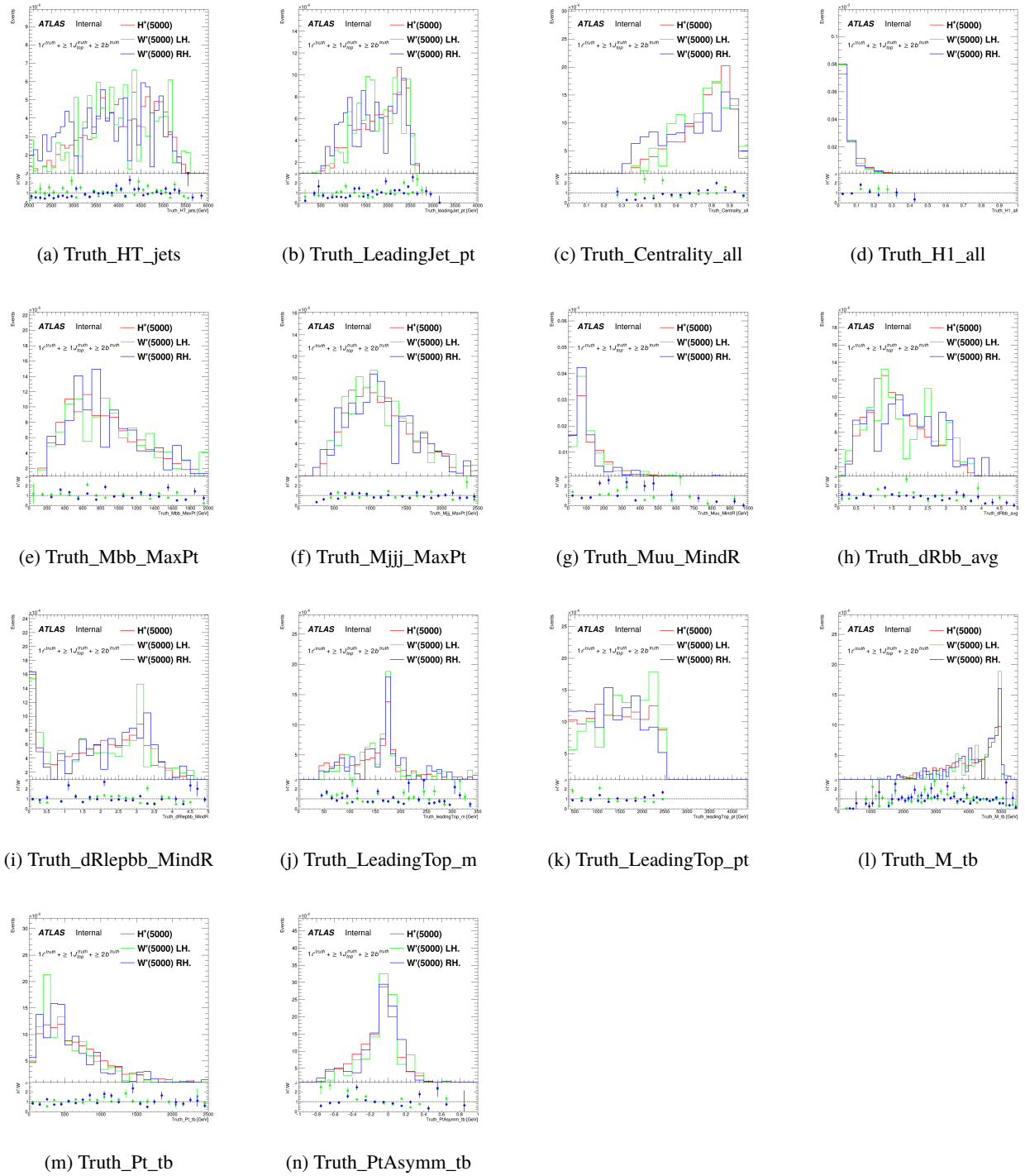


Figure 65: Comparison of the kinematic variables between tbW' and tbH^+ in truth level on 5000 GeV mass hypothesis.

805 9 Summary and Conclusions

806 We have performed a search for charged Higgs boson H^+ as well as W' bosons produced in association with
807 a top quark and a bottom quark, and decaying into a top quark and a bottom quark, in the lepton-plus-jets
808 final state, in the regime where the top quark from the parent boson is highly boosted to be reconstructed as
809 a top-tagged large- R jet. The mass range $1000 < m_{H^+} < 3000$ GeV is investigated. Expected upper cross
810 section limits between 0.073 pb and 0.011 pb were set.

811 **Limits for W' is to be finalized.**

812 References

- 813 [1] ATLAS Collaboration, *Observation of a new particle in the search for the Standard Model Higgs*
 814 *boson with the ATLAS detector at the LHC*, *Phys. Lett. B* **716** (2012) 1, arXiv: [1207.7214](#)
 815 [[hep-ex](#)] (cit. on p. 7).
- 816 [2] CMS Collaboration, *Observation of a new boson at a mass of 125 GeV with the CMS experiment*
 817 *at the LHC*, *Phys. Lett. B* **716** (2012) 30, arXiv: [1207.7235](#) [[hep-ex](#)] (cit. on p. 7).
- 818 [3] ATLAS and CMS Collaborations, *Combined Measurement of the Higgs Boson Mass in pp*
 819 *Collisions at $\sqrt{s} = 7$ and 8 TeV with the ATLAS and CMS Experiments*, *Phys. Rev. Lett.* **114**
 820 (2015) 191803, arXiv: [1503.07589](#) [[hep-ex](#)] (cit. on p. 7).
- 821 [4] T. D. Lee, *A Theory of Spontaneous T Violation*, *Phys. Rev. D* **8** (1973) (cit. on p. 7).
- 822 [5] G. Branco, P. Ferreira, L. Lavoura, M. Rebelo and M. Sher et al., *Theory and phenomenology of*
 823 *two-Higgs-doublet models*, *Phys. Rept.* **516** (2012), arXiv: [1106.0034](#) [[hep-ph](#)] (cit. on p. 7).
- 824 [6] K. Inoue, A. Kakuto, H. Komatsu and S. Takeshita, *Aspects of Grand Unified Models with Softly*
 825 *Broken Supersymmetry*, *Prog.Theor.Phys.* **68** (1982) (cit. on p. 7).
- 826 [7] T. Cheng and L.-F. Li, *Neutrino Masses, Mixings and Oscillations in $SU(2) \times U(1)$ Models of*
 827 *Electroweak Interactions*, *Phys. Rev. D* **22** (1980) (cit. on p. 7).
- 828 [8] J. Schechter and J. Valle, *Neutrino Masses in $SU(2) \times U(1)$ Theories*, *Phys. Rev. D* **22** (1980) (cit. on
 829 p. 7).
- 830 [9] G. Lazarides, Q. Shafi and C. Wetterich, *Proton Lifetime and Fermion Masses in an $SO(10)$ Model*,
 831 *Nucl. Phys. B* **181** (1981) (cit. on p. 7).
- 832 [10] R. Mohapatra and G. Senjanovic, *Neutrino Masses and Mixings in Gauge Models with Spontaneous*
 833 *Parity Violation*, *Phys. Rev. D* **23** (1981) (cit. on p. 7).
- 834 [11] M. Magg and C. Wetterich, *Neutrino Mass Problem and Gauge Hierarchy*, *Phys. Lett. B* **94** (1980)
 835 (cit. on p. 7).
- 836 [12] ATLAS Collaboration, *Search for charged Higgs bosons decaying via $H^\pm \rightarrow \tau\nu$ in $t\bar{t}$ events using*
 837 *pp collision data at $\sqrt{s} = 7$ TeV with the ATLAS detector*, *JHEP* **06** (2012) 039, arXiv: [1204.2760](#)
 838 [[hep-ex](#)] (cit. on p. 7).
- 839 [13] ATLAS Collaboration, *Search for charged Higgs bosons through the violation of lepton universality*
 840 *in $t\bar{t}$ events using pp collision data at $\sqrt{s} = 7$ TeV with the ATLAS experiment*, *JHEP* **03** (2013) 076,
 841 arXiv: [1212.3572](#) [[hep-ex](#)] (cit. on p. 7).
- 842 [14] ATLAS Collaboration, *Search for charged Higgs bosons decaying via $H^\pm \rightarrow \tau^\pm\nu$ in fully hadronic*
 843 *final states using pp collision data at $\sqrt{s} = 8$ TeV with the ATLAS detector*, *JHEP* **03** (2015) 088,
 844 arXiv: [1412.6663](#) [[hep-ex](#)] (cit. on p. 7).
- 845 [15] CMS Collaboration, *Search for a light charged Higgs boson in top quark decays in pp collisions at*
 846 *$\sqrt{s} = 7$ TeV*, *JHEP* **07** (2012) 143, arXiv: [1205.5736](#) [[hep-ex](#)] (cit. on p. 7).
- 847 [16] CMS Collaboration, *Search for a charged Higgs boson in pp collisions at $\sqrt{s} = 8$ TeV*, *JHEP* **11**
 848 (2015) 018, arXiv: [1508.07774](#) [[hep-ex](#)] (cit. on p. 7).
- 849 [17] ATLAS Collaboration, *Search for charged Higgs bosons decaying via $H^\pm \rightarrow \tau^\pm\nu_\tau$ in the $\tau+jets$*
 850 *and $\tau+lepton$ final states with 36fb^{-1} of pp collision data recorded at $\sqrt{s} = 13$ TeV with the ATLAS*
 851 *experiment*, *JHEP* **09** (2018) 139, arXiv: [1807.07915](#) [[hep-ex](#)] (cit. on p. 7).

- [18] ATLAS Collaboration, *Search for a light charged Higgs boson in the decay channel $H^+ \rightarrow c\bar{s}$ in $t\bar{t}$ events using pp collisions at $\sqrt{s} = 7$ TeV with the ATLAS detector*, *Eur. Phys. J. C* **73** (2013) 2465, arXiv: [1302.3694 \[hep-ex\]](#) (cit. on p. 7).
- [19] CMS Collaboration, *Search for a light charged Higgs boson decaying to $c\bar{s}$ in pp collisions at $\sqrt{s} = 8$ TeV*, *JHEP* **12** (2015) 178, arXiv: [1510.04252 \[hep-ex\]](#) (cit. on p. 7).
- [20] CMS Collaboration, *Search for a charged Higgs boson decaying to charm and bottom quarks in proton–proton collisions at $\sqrt{s} = 8$ TeV*, *JHEP* **11** (2018) 115, arXiv: [1808.06575 \[hep-ex\]](#) (cit. on p. 7).
- [21] ATLAS Collaboration, *Search for charged Higgs bosons in the $H^\pm \rightarrow tb$ decay channel in pp collisions at $\sqrt{s} = 8$ TeV using the ATLAS detector*, *JHEP* **03** (2016) 127, arXiv: [1512.03704 \[hep-ex\]](#) (cit. on p. 7).
- [22] ATLAS Collaboration, *Search for charged Higgs bosons produced in association with a top quark and decaying via $H^\pm \rightarrow \tau\nu$ using pp collision data recorded at $\sqrt{s} = 13$ TeV by the ATLAS detector*, *Phys. Lett. B* **759** (2016) 555, arXiv: [1603.09203 \[hep-ex\]](#) (cit. on p. 7).
- [23] ATLAS Collaboration, *Search for charged Higgs bosons decaying into top and bottom quarks at $\sqrt{s} = 13$ TeV with the ATLAS detector*, *JHEP* **11** (2018) 085, arXiv: [1808.03599 \[hep-ex\]](#) (cit. on pp. 7, 49).
- [24] ATLAS Collaboration, *Search for a charged Higgs bosons decaying into a top-quark and a bottom-quark at $\sqrt{s} = 13$ TeV with the ATLAS detector*, *JHEP* **16** (2021) 145, arXiv: [2102.10076 \[hep-ex\]](#) (cit. on pp. 7, 32, 76).
- [25] CMS Collaboration, *Search for a charged Higgs boson decaying into top and bottom quarks in events with electrons or muons in proton–proton collisions at $\sqrt{s} = 13$ TeV*, *JHEP* **01** (2020) 096, arXiv: [1908.09206 \[hep-ex\]](#) (cit. on p. 7).
- [26] CMS Collaboration, *Search for charged Higgs bosons decaying into a top and a bottom quark in the all-jet final state of pp collisions at $\sqrt{s} = 13$ TeV*, (2020), arXiv: [2001.07763 \[hep-ex\]](#) (cit. on p. 7).
- [27] ATLAS Collaboration, *Search for dijet resonances in events with an isolated charged lepton using $\sqrt{s} = 13$ TeV proton–proton collision data collected by the ATLAS detector*, *JHEP* **06** (2020) 151, arXiv: [2002.11325 \[hep-ex\]](#) (cit. on p. 7).
- [28] ATLAS Collaboration, *Search for a Charged Higgs Boson Produced in the Vector-Boson Fusion Mode with Decay $H^\pm \rightarrow W^\pm Z$ using pp Collisions at $\sqrt{s} = 8$ TeV with the ATLAS Experiment*, *Phys. Rev. Lett.* **114** (2015) 231801, arXiv: [1503.04233 \[hep-ex\]](#) (cit. on p. 7).
- [29] CMS Collaboration, *Search for charged Higgs bosons produced via vector boson fusion and decaying into a pair of W and Z bosons using pp collisions at $\sqrt{s} = 13$ TeV*, *Phys. Rev. Lett.* **119** (2017) 141802, arXiv: [1705.02942 \[hep-ex\]](#) (cit. on p. 7).
- [30] ATLAS Collaboration, *Luminosity determination in pp collisions at $\sqrt{s} = 13$ TeV using the ATLAS detector at the LHC*, ATLAS-CONF-2019-021, 2019, URL: <https://cds.cern.ch/record/2677054> (cit. on pp. 9, 45).
- [31] *LuminosityForPhysics* twiki page, URL: <https://twiki.cern.ch/twiki/bin/viewauth/Atlas/LuminosityForPhysics> (cit. on p. 9).
- [32] *Web directory for GoodRunsLists in atlas-groupdata area*, URL: <https://atlas-groupdata.web.cern.ch/atlas-groupdata/GoodRunsLists> (cit. on p. 9).

- [33] C. Degrande, M. Ubiali, M. Wiesemann and M. Zaro, *Heavy charged Higgs boson production at the LHC*, JHEP **10** (2015) 145, arXiv: [1507.02549 \[hep-ph\]](#) (cit. on p. 10).
- [34] J. Alwall et al., *The automated computation of tree-level and next-to-leading order differential cross sections, and their matching to parton shower simulations*, JHEP **07** (2014) 079, arXiv: [1405.0301 \[hep-ph\]](#) (cit. on pp. 10, 52).
- [35] R. D. Ball et al., *Parton distributions with LHC data*, Nucl. Phys. B **867** (2013) 244, arXiv: [1207.1303 \[hep-ph\]](#) (cit. on p. 10).
- [36] R. D. Ball et al., *Parton distributions for the LHC run II*, JHEP **04** (2015) 040, arXiv: [1410.8849 \[hep-ph\]](#) (cit. on pp. 10, 11).
- [37] T. Sjöstrand, S. Mrenna and P. Skands, *A brief introduction to PYTHIA 8.1*, Comput. Phys. Commun. **178** (2008) 852, arXiv: [0710.3820 \[hep-ph\]](#) (cit. on p. 10).
- [38] ATLAS Collaboration, *ATLAS Pythia 8 tunes to 7 TeV data*, ATL-PHYS-PUB-2014-021, 2014, URL: <https://cds.cern.ch/record/1966419> (cit. on pp. 10, 50).
- [39] M. Flechl, M. Klees, M. Krämer, M. Spira and M. Ubiali, *Improved cross-section predictions for heavy charged Higgs boson production at the LHC*, Physical Review D **91** (2015), URL: <http://dx.doi.org/10.1103/PhysRevD.91.075015>, ISSN:1550-2368 (cit. on p. 10).
- [40] S. Dittmaier, M. Krämer, M. Spira and M. Walser, *Charged-Higgs-boson production at the LHC: Next-to-leading-order supersymmetric QCD corrections*, Physical Review D **83** (2011), URL: <http://dx.doi.org/10.1103/PhysRevD.83.055005>, ISSN:1550-2368 (cit. on p. 10).
- [41] E. Berger, T. Han, J. Jiang and T. Plehn, *Associated production of a top quark and a charged Higgs boson*, Physical Review D **71** (2005), URL: <http://dx.doi.org/10.1103/PhysRevD.71.115012>, ISSN:1550-2368 (cit. on p. 10).
- [42] P. Nason, *A new method for combining NLO QCD with shower Monte Carlo algorithms*, JHEP **11** (2004) 040, arXiv: [hep-ph/0409146](#) (cit. on p. 11).
- [43] S. Frixione, P. Nason and C. Oleari, *Matching NLO QCD computations with parton shower simulations: the POWHEG method*, JHEP **11** (2007) 070, arXiv: [0709.2092 \[hep-ph\]](#) (cit. on p. 11).
- [44] S. Alioli, P. Nason, C. Oleari and E. Re, *A general framework for implementing NLO calculations in shower Monte Carlo programs: the POWHEG BOX*, JHEP **06** (2010) 043, arXiv: [1002.2581 \[hep-ph\]](#) (cit. on p. 11).
- [45] J. Campbell, R. Ellis, P. Nason and E. Re, *Top-pair production and decay at NLO matched with parton showers*, JHEP **04** (2015), arXiv: [1412.1828 \[hep-ph\]](#) (cit. on p. 11).
- [46] ATLAS Collaboration, *Studies on top-quark Monte Carlo modelling for Top2016*, ATL-PHYS-PUB-2016-020, 2016, URL: <https://cds.cern.ch/record/2216168> (cit. on pp. 11, 13).
- [47] T. Sjöstrand et al., *An introduction to PYTHIA 8.2*, Comput. Phys. Commun. **191** (2015) 159, arXiv: [1410.3012 \[hep-ph\]](#) (cit. on p. 11).
- [48] M. Bahr et al., *Herwig++ physics and manual*, Eur. Phys. J. C **58** (2008) 639, arXiv: [0803.0883 \[hep-ph\]](#) (cit. on p. 11).
- [49] J. Bellm et al., *Herwig 7.0/Herwig++ 3.0 release note*, Eur. Phys. J. C **76** (2016) 196, arXiv: [1512.01178 \[hep-ph\]](#) (cit. on p. 11).

- [50] ATLAS Collaboration, *Studies on top-quark Monte Carlo modelling with Sherpa and MG5_aMC@NLO*, ATL-PHYS-PUB-2017-007, 2017, URL: <https://cds.cern.ch/record/2261938> (cit. on p. 11).
- [51] H. B. Hartanto, B. Jäger, L. Reina and D. Wackerlo, *Higgs boson production in association with top quarks in the POWHEG BOX*, Phys. Rev. D **91** (2015) 094003, arXiv: [1501.04498 \[hep-ph\]](https://arxiv.org/abs/1501.04498) (cit. on p. 12).
- [52] E. Bothmann et al., *Event Generation with Sherpa 2.2*, SciPost Phys. **7** (2019) 034, arXiv: [1905.09127 \[hep-ph\]](https://arxiv.org/abs/1905.09127) (cit. on p. 12).
- [53] S. Catani, F. Krauss, R. Kuhn and B. R. Webber, *QCD Matrix Elements + Parton Showers*, JHEP **11** (2001) 063, arXiv: [hep-ph/0109231](https://arxiv.org/abs/hep-ph/0109231) (cit. on pp. 12, 14).
- [54] S. Höche, F. Krauss, S. Schumann and F. Siegert, *QCD matrix elements and truncated showers*, JHEP **05** (2009) 053, arXiv: [0903.1219 \[hep-ph\]](https://arxiv.org/abs/0903.1219) (cit. on pp. 12, 14).
- [55] R. Frederix, E. Re and P. Torrielli, *Single-top t-channel hadroproduction in the four-flavour scheme with POWHEG and aMC@NLO*, JHEP **09** (2012) 130, arXiv: [1207.5391 \[hep-ph\]](https://arxiv.org/abs/1207.5391) (cit. on pp. 12, 14).
- [56] S. Frixione, E. Laenen, P. Motylinski and B. R. Webber, *Angular correlations of lepton pairs from vector boson and top quark decays in Monte Carlo simulations*, JHEP **04** (2007) 081, arXiv: [hep-ph/0702198](https://arxiv.org/abs/hep-ph/0702198) (cit. on p. 13).
- [57] P. Artoisenet, R. Frederix, O. Mattelaer and R. Rietkerk, *Automatic spin-entangled decays of heavy resonances in Monte Carlo simulations*, JHEP **03** (2013) 015, arXiv: [1212.3460 \[hep-ph\]](https://arxiv.org/abs/1212.3460) (cit. on p. 13).
- [58] S. Frixione, E. Laenen, P. Motylinski, C. D. White and B. R. Webber, *Single-top hadroproduction in association with a W boson*, JHEP **07** (2008) 029, arXiv: [0805.3067 \[hep-ph\]](https://arxiv.org/abs/0805.3067) (cit. on pp. 13, 14, 52).
- [59] ATLAS Collaboration, *Measurement of the production cross-section of a single top quark in association with a Z boson in proton–proton collisions at 13 TeV with the ATLAS detector*, Phys. Lett. B **780** (2018) 557, arXiv: [1710.03659 \[hep-ex\]](https://arxiv.org/abs/1710.03659) (cit. on p. 14).
- [60] J. Pumplin et al., *New Generation of Parton Distributions with Uncertainties from Global QCD Analysis*, JHEP **07** (2002) 012, arXiv: [hep-ph/0201195](https://arxiv.org/abs/hep-ph/0201195) (cit. on p. 14).
- [61] R. Frederix, D. Pagani and M. Zaro, *Large NLO corrections in $t\bar{t}W^\pm$ and $t\bar{t}t\bar{t}$ hadroproduction from supposedly subleading EW contributions*, JHEP **02** (2018) 031, arXiv: [1711.02116 \[hep-ph\]](https://arxiv.org/abs/1711.02116) (cit. on p. 14).
- [62] T. Gleisberg and S. Höche, *Comix, a new matrix element generator*, JHEP **12** (2008) 039, arXiv: [0808.3674 \[hep-ph\]](https://arxiv.org/abs/0808.3674) (cit. on p. 14).
- [63] F. Cascioli, P. Maierhöfer and S. Pozzorini, *Scattering Amplitudes with Open Loops*, Phys. Rev. Lett. **108** (2012) 111601, arXiv: [1111.5206 \[hep-ph\]](https://arxiv.org/abs/1111.5206) (cit. on p. 14).
- [64] A. Denner, S. Dittmaier and L. Hofer, *Collier: A fortran-based complex one-loop library in extended regularizations*, Comput. Phys. Commun. **212** (2017) 220, arXiv: [1604.06792 \[hep-ph\]](https://arxiv.org/abs/1604.06792) (cit. on p. 14).
- [65] S. Schumann and F. Krauss, *A parton shower algorithm based on Catani–Seymour dipole factorisation*, JHEP **03** (2008) 038, arXiv: [0709.1027 \[hep-ph\]](https://arxiv.org/abs/0709.1027) (cit. on p. 14).

- [66] J.-C. Winter, F. Krauss and G. Soff, *A modified cluster-hadronization model*, *Eur. Phys. J. C* **36** (2004) 381, arXiv: [hep-ph/0311085](#) (cit. on p. 14).
- [67] S. Höche, F. Krauss, M. Schönherr and F. Siegert, *A critical appraisal of NLO+PS matching methods*, *JHEP* **09** (2012) 049, arXiv: [1111.1220 \[hep-ph\]](#) (cit. on p. 14).
- [68] S. Höche, F. Krauss, M. Schönherr and F. Siegert, *QCD matrix elements + parton showers. The NLO case*, *JHEP* **04** (2013) 027, arXiv: [1207.5030 \[hep-ph\]](#) (cit. on p. 14).
- [69] E. Bothmann, M. Schönherr and S. Schumann, *Reweighting QCD matrix-element and parton-shower calculations*, *Eur. Phys. J. C* **76** (2016) 590, arXiv: [1606.08753 \[hep-ph\]](#) (cit. on p. 14).
- [70] ATLAS Collaboration, *Electron reconstruction and identification efficiency measurements with the ATLAS detector using the 2011 LHC proton–proton collision data*, *Eur. Phys. J. C* **74** (2014) 2941, arXiv: [1404.2240 \[hep-ex\]](#) (cit. on p. 16).
- [71] ATLAS Collaboration, *Electron efficiency measurements with the ATLAS detector using the 2015 LHC proton–proton collision data*, ATLAS-CONF-2016-024, 2016, URL: <https://cds.cern.ch/record/2157687> (cit. on p. 16).
- [72] *Lepton isolation recommendations*, URL: <https://twiki.cern.ch/twiki/bin/viewauth/AtlasProtected/IsolationSelectionTool> (cit. on p. 16).
- [73] ATLAS Collaboration, *Muon reconstruction performance of the ATLAS detector in proton–proton collision data at $\sqrt{s} = 13\text{ TeV}$* , *Eur. Phys. J. C* **76** (2016) 292, arXiv: [1603.05598 \[hep-ex\]](#) (cit. on pp. 16, 45, 47).
- [74] ATLAS Collaboration, *Reconstruction, Energy Calibration, and Identification of Hadronically Decaying Tau Leptons in the ATLAS Experiment for Run-2 of the LHC*, ATL-PHYS-PUB-2015-045, 2015, URL: <https://cds.cern.ch/record/2064383> (cit. on p. 16).
- [75] M. Cacciari, G. P. Salam and G. Soyez, *The anti- k_t jet clustering algorithm*, *JHEP* **04** (2008) 063, arXiv: [0802.1189 \[hep-ph\]](#) (cit. on p. 16).
- [76] ATLAS Collaboration, *Jet reconstruction and performance using particle flow with the ATLAS Detector*, *Eur. Phys. J. C* **77** (2017) 466, arXiv: [1703.10485 \[hep-ex\]](#) (cit. on p. 16).
- [77] ATLAS Collaboration, *Jet energy scale and resolution measured in proton–proton collisions at $\sqrt{s} = 13\text{ TeV}$ with the ATLAS detector*, (2020), arXiv: [2007.02645 \[hep-ex\]](#) (cit. on p. 16).
- [78] ATLAS Collaboration, *Performance of pile-up mitigation techniques for jets in pp collisions at $\sqrt{s} = 8\text{ TeV}$ using the ATLAS detector*, *Eur. Phys. J. C* **76** (2016) 581, arXiv: [1510.03823 \[hep-ex\]](#) (cit. on pp. 16, 47).
- [79] ATLAS Collaboration, *ATLAS b-jet identification performance and efficiency measurement with $t\bar{t}$ events in pp collisions at $\sqrt{s} = 13\text{ TeV}$* , *Eur. Phys. J. C* **79** (2019) 970, arXiv: [1907.05120 \[hep-ex\]](#) (cit. on pp. 16, 48).
- [80] ATLAS Collaboration, *Topological cell clustering in the ATLAS calorimeters and its performance in LHC Run 1*, *Eur. Phys. J. C* **77** (2017) 490, arXiv: [1603.02934 \[hep-ex\]](#) (cit. on p. 17).
- [81] D. Krohn, J. Thaler and L.-T. Wang, *Jet trimming*, *Journal of High Energy Physics* **2010** (2010) 84, URL: [https://link.springer.com/article/10.1007/JHEP02\(2010\)084](https://link.springer.com/article/10.1007/JHEP02(2010)084), ISSN:1029-8479 (cit. on p. 17).

- 1015 [82] S. Catani, Y. Dokshitzer, M. Seymour and B. Webber, *Longitudinally invariant K(t) clustering*
 1016 *algorithms for hadron-hadron collisions*, Nuclear Physics B **406** (1993) 187, URL: <https://www.sciencedirect.com/science/article/pii/055032139390166M>, ISSN:0550-3213
 1017 (cit. on p. 17).
- 1019 [83] ATLAS Collaboration, *Identification of boosted, hadronically decaying W bosons and comparisons*
 1020 *with ATLAS data taken at $\sqrt{s} = 8 \text{ TeV}$* , Eur. Phys. J. C **76** (2016) 154, arXiv: [1510.05821](https://arxiv.org/abs/1510.05821) [hep-ex] (cit. on p. 17).
- 1022 [84] ATLAS Collaboration, *Jet mass reconstruction with the ATLAS Detector in early Run 2 data*,
 1023 ATLAS-CONF-2016-035, 2016, URL: <https://cds.cern.ch/record/2200211> (cit. on p. 17).
- 1024 [85] ATLAS Collaboration, *Boosted hadronic vector boson and top quark tagging with ATLAS using*
 1025 *Run 2 data*, ATL-PHYS-PUB-2020-017, 2020, URL: <https://cds.cern.ch/record/2724149>
 1026 (cit. on pp. 17, 49).
- 1027 [86] J. Thaler and K. Van Tilburg, *Identifying Boosted Objects with N-subjettiness*, JHEP **03** (2011) 015,
 1028 arXiv: [1011.2268](https://arxiv.org/abs/1011.2268) [hep-ph] (cit. on p. 17).
- 1029 [87] J. Thaler and L.-T. Wang, *Strategies to Identify Boosted Tops*, JHEP **07** (2008) 092, arXiv:
 1030 [0806.0023](https://arxiv.org/abs/0806.0023) [hep-ph] (cit. on p. 17).
- 1031 [88] A. Larkoski, G. Salam and J. Thaler, *Energy Correlation Functions for Jet Substructure*, JHEP **06**
 1032 (2013) 108, arXiv: [1305.0007](https://arxiv.org/abs/1305.0007) [hep-ph] (cit. on p. 17).
- 1033 [89] D. Adams and et al., *Recommendations of the Physics Objects and Analysis Harmonisation Study*
 1034 *Groups 2014*, ATL-PHYS-INT-2014-018, 2014, URL: <https://cds.cern.ch/record/1743654>
 1035 (cit. on p. 18).
- 1036 [90] *Documentation of the ATLAS AssociationUtils package*, URL: <https://gitlab.cern.ch/atlas/athena/blob/release/21.2.86/PhysicsAnalysis/AnalysisCommon/AssociationUtils/README.rst> (cit. on p. 18).
- 1039 [91] J. Gallicchio and Y.-T. Chien, *Quit Using Pseudorapidity, Transverse Energy, and Massless*
 1040 *Constituents*, 2018, arXiv: [1802.05356](https://arxiv.org/abs/1802.05356) [hep-ph] (cit. on p. 18).
- 1041 [92] A. Hoecker et al., *TMVA - Toolkit for Multivariate Data Analysis*, 2007, arXiv: [physics/0703039](https://arxiv.org/abs/physics/0703039)
 1042 [physics.data-an] (cit. on p. 22).
- 1043 [93] *Automatic binning implematation in TTHFitter*. URL: https://indico.cern.ch/event/455289/contributions/1953694/attachments/1209081/1762963/Calvet_binning_Htop_160108.pdf (cit. on pp. 34, 53).
- 1046 [94] G. Avoni and et al., *The new LUCID-2 detector for luminosity measurement and monitoring in*
 1047 *ATLAS*, JINST **13** (2018) P07017 (cit. on p. 45).
- 1048 [95] ATLAS Collaboration, *Measurement of the Inelastic Proton–Proton Cross Section at $\sqrt{s} = 13 \text{ TeV}$*
 1049 *with the ATLAS Detector at the LHC*, Phys. Rev. Lett. **117** (2016) 182002, arXiv: [1606.02625](https://arxiv.org/abs/1606.02625) [hep-ex] (cit. on p. 45).
- 1051 [96] ATLAS Collaboration, *Electron reconstruction and identification in the ATLAS experiment using*
 1052 *the 2015 and 2016 LHC proton–proton collision data at $\sqrt{s} = 13 \text{ TeV}$* , Eur. Phys. J. C **79** (2019) 639,
 1053 arXiv: [1902.04655](https://arxiv.org/abs/1902.04655) [hep-ex] (cit. on p. 45).
- 1054 [97] ATLAS Collaboration, *Electron and photon performance measurements with the ATLAS detector*
 1055 *using the 2015–2017 LHC proton–proton collision data*, JINST **14** (2019) P12006, arXiv: [1908.00005](https://arxiv.org/abs/1908.00005) [hep-ex] (cit. on p. 47).

- [98] ATLAS Collaboration, *Jet energy scale measurements and their systematic uncertainties in proton–proton collisions at $\sqrt{s} = 13\text{ TeV}$ with the ATLAS detector*, *Phys. Rev. D* **96** (2017) 072002, arXiv: [1703.09665 \[hep-ex\]](#) (cit. on p. 47).
- [99] ATLAS Collaboration, *Determination of jet calibration and energy resolution in proton–proton collisions at $\sqrt{s} = 8\text{ TeV}$ using the ATLAS detector*, (2019), arXiv: [1910.04482 \[hep-ex\]](#) (cit. on p. 47).
- [100] ATLAS Collaboration, *In situ calibration of large-radius jet energy and mass in 13 TeV proton–proton collisions with the ATLAS detector*, *Eur. Phys. J. C* **79** (2019) 135, arXiv: [1807.09477 \[hep-ex\]](#) (cit. on pp. 47, 48).
- [101] ATLAS Collaboration, *Measurement of the ATLAS Detector Jet Mass Response using Forward Folding with 80fb^{-1} of $\sqrt{s} = 13\text{ TeV}$ pp data*, ATLAS-CONF-2020-022, 2020, URL: <https://cds.cern.ch/record/2724442> (cit. on p. 48).
- [102] ATLAS Collaboration, *Measurement of b-tagging efficiency of c-jets in $t\bar{t}$ events using a likelihood approach with the ATLAS detector*, ATLAS-CONF-2018-001, 2018, URL: <https://cds.cern.ch/record/2306649> (cit. on p. 49).
- [103] ATLAS Collaboration, *Calibration of light-flavour b-jet mistagging rates using ATLAS proton–proton collision data at $\sqrt{s} = 13\text{ TeV}$* , ATLAS-CONF-2018-006, 2018, URL: <https://cds.cern.ch/record/2314418> (cit. on p. 49).
- [104] ATLAS Collaboration, *Performance of top-quark and W-boson tagging with ATLAS in Run 2 of the LHC*, *Eur. Phys. J. C* **79** (2019) 375, arXiv: [1808.07858 \[hep-ex\]](#) (cit. on p. 49).
- [105] J. Butterworth et al., *PDF4LHC recommendations for LHC Run II*, *J. Phys. G* **43** (2016) 023001, arXiv: [1510.03865 \[hep-ph\]](#) (cit. on p. 49).
- [106] D. de Florian et al., *Handbook of LHC Higgs Cross Sections: 4. Deciphering the Nature of the Higgs Sector*, (2016), arXiv: [1610.07922 \[hep-ph\]](#) (cit. on p. 51).
- [107] R. Raitio and W. W. Wada, *Higgs Boson Production at Large Transverse Momentum in QCD*, *Phys. Rev. D* **19** (1979) (cit. on p. 51).
- [108] W. Beenakker and et al., *NLO QCD corrections to t anti-t H production in hadron collisions*, *Nucl. Phys. B* **653** (2003), arXiv: [hep-ph/0211352 \[hep-ph\]](#) (cit. on p. 51).
- [109] S. Dawson, C. Jackson, L. H. Orr, L. Reina and D. Wackerlo, *Associated Higgs production with top quarks at the large hadron collider: NLO QCD corrections*, *Phys. Rev. D* **68** (2003), arXiv: [hep-ph/0305087 \[hep-ph\]](#) (cit. on p. 51).
- [110] Y. Zhang, W.-G. Ma, R.-Y. Zhang, C. Chen and L. Guo, *QCD NLO and EW NLO corrections to $t\bar{t}H$ production with top quark decays at hadron collider*, *Phys. Lett. B* **738** (2014), arXiv: [1407.1110 \[hep-ph\]](#) (cit. on p. 51).
- [111] S. Frixione, V. Hirschi, D. Pagani, H.-S. Shao and M. Zaro, *Electroweak and QCD corrections to top-pair hadroproduction in association with heavy bosons*, *JHEP* **06** (2015), arXiv: [1504.03446 \[hep-ph\]](#) (cit. on p. 51).
- [112] LHCTopWG, *NLO single-top channel cross sections*, 2017, URL: <https://twiki.cern.ch/twiki/bin/view/LHCPhysics/SingleTopRefXsec> (cit. on p. 52).
- [113] A. D. Martin, W. J. Stirling, R. S. Thorne and G. Watt, *Parton distributions for the LHC*, *Eur. Phys. J. C* **63** (2009) 189, arXiv: [0901.0002 \[hep-ph\]](#) (cit. on p. 52).

- 1098 [114] A. D. Martin, W. Stirling, R. Thorne and G. Watt, *Uncertainties on α_S in global PDF analyses*
1099 *and implications for predicted hadronic cross sections*, *Eur. Phys. J. C* **64** (2009) 653, arXiv:
1100 [0905.3531 \[hep-ph\]](#) (cit. on p. 52).
- 1101 [115] M. Aliev et al., *HATHOR – HAdronic Top and Heavy quarks crOss section calculatoR*, *Comput.*
1102 *Phys. Commun.* **182** (2011) 1034, arXiv: [1007.1327 \[hep-ph\]](#) (cit. on p. 52).
- 1103 [116] P. Kant et al., *HatHor for single top-quark production: Updated predictions and uncertainty*
1104 *estimates for single top-quark production in hadronic collisions*, *Comput. Phys. Commun.* **191**
1105 (2015) 74, arXiv: [1406.4403 \[hep-ph\]](#) (cit. on p. 52).
- 1106 [117] LHCHXSWG1, *Recommended predictions for $t\bar{t}V$ cross sections*, URL: https://twiki.cern.ch/twiki/bin/view/LHCPhysics/LHCHXSWGTT#Plans_for_YR4 (cit. on p. 52).
- 1107 [118] J. M. Campbell and R. K. Ellis, *$t\bar{t}W^{+-}$ production and decay at NLO*, *JHEP* **07** (2012), arXiv:
1108 [1204.5678 \[hep-ph\]](#) (cit. on p. 52).
- 1109 [119] ATLAS PMG Top processes twiki page, URL: <https://twiki.cern.ch/twiki/bin/view/AtlasProtected/PmgTopProcesses> (cit. on p. 52).
- 1110 [120] ATLAS Collaboration, *Multi-boson simulation for 13 TeV ATLAS analyses*, ATL-PHYS-PUB-
1111 2016-002, 2016, URL: <https://cds.cern.ch/record/2119986> (cit. on p. 52).
- 1112 [121] PhysicsModellingGroup, *TruthDAOD*, URL: <https://twiki.cern.ch/twiki/bin/view/AtlasProtected/TruthDAOD> (cit. on p. 77).
- 1113 [122] W. Bell et al., *Proposal for truth particle observable definitions*, (), URL: <https://cds.cern.ch/record/1700541> (cit. on p. 77).

1118 **Appendices**

1119 **A TOPQ1 DAOD list**

1120 **A.1 Data**

1121 Table 23 is the TOPQ1 DAOD list for data sample in this analysis.

data15_13TeV.AllYear.physics_Main.PhysCont.DAOD_TOPQ1.grp15_v01_p4513
data16_13TeV.AllYear.physics_Main.PhysCont.DAOD_TOPQ1.grp16_v01_p4513
data17_13TeV.AllYear.physics_Main.PhysCont.DAOD_TOPQ1.grp17_v01_p4513
data18_13TeV.AllYear.physics_Main.PhysCont.DAOD_TOPQ1.grp18_v01_p4513

Table 23: TOPQ1 DAOD list for data sample in this analysis.

1122 **A.2 $t\bar{t}H^+$**

1123 Table 24 is the TOPQ1 DAOD list for H^+ sample in this analysis.

Nominal
mc16_13TeV.450004.aMcAtNloPythia8EvtGen_A14NNPDF23LO_Hplus4FS_H1000_tb.deriv.DAOD_TOPQ1.e7137_s3126_r9364_p4514
mc16_13TeV.450598.aMcAtNloPythia8EvtGen_A14NNPDF23LO_Hplus4FS_H1200_tb.deriv.DAOD_TOPQ1.e7429_s3126_r9364_p4514
mc16_13TeV.450599.aMcAtNloPythia8EvtGen_A14NNPDF23LO_Hplus4FS_H1400_tb.deriv.DAOD_TOPQ1.e7429_s3126_r9364_p4514
mc16_13TeV.450600.aMcAtNloPythia8EvtGen_A14NNPDF23LO_Hplus4FS_H1600_tb.deriv.DAOD_TOPQ1.e7429_s3126_r9364_p4514
mc16_13TeV.450601.aMcAtNloPythia8EvtGen_A14NNPDF23LO_Hplus4FS_H1800_tb.deriv.DAOD_TOPQ1.e7429_s3126_r9364_p4514
mc16_13TeV.450602.aMcAtNloPythia8EvtGen_A14NNPDF23LO_Hplus4FS_H2000_tb.deriv.DAOD_TOPQ1.e7429_s3126_r9364_p4514
mc16_13TeV.451490.aMcAtNloPythia8EvtGen_A14NNPDF23LO_Hplus4FS_H2500_tb.deriv.DAOD_TOPQ1.e7970_s3126_r9364_p4514
mc16_13TeV.451491.aMcAtNloPythia8EvtGen_A14NNPDF23LO_Hplus4FS_H3000_tb.deriv.DAOD_TOPQ1.e7970_s3126_r9364_p4514
mc16_13TeV.508710.MGPy8EG_A14NNPDF30_Hplus4FS_H4000_tb.deriv.DAOD_TOPQ1.e8276_s3126_r9364_p4514
mc16_13TeV.508711.MGPy8EG_A14NNPDF30_Hplus4FS_H5000_tb.deriv.DAOD_TOPQ1.e8276_s3126_r9364_p4514

Table 24: TOPQ1 DAOD list for H^+ sample in this analysis.

1124 **A.3 $t\bar{t} + \text{jets}$**

1125 Table 25 is the TOPQ1 DAOD list for $t\bar{t} + \text{jets}$ sample in this analysis.

Nominal
mc16_13TeV.410470.PhPy8EG_A14_ttbar_hdamp258p75_nonallhad.deriv.DAOD_TOPQ1.e6337_s3126_r9364_p4514
mc16_13TeV.410471.PhPy8EG_A14_ttbar_hdamp258p75_allhad.deriv.DAOD_TOPQ1.e6337_s3126_r9364_p4514
mc16_13TeV.411073.PhPy8EG_A14_ttbar_hdamp258p75_ljets_BBFilt.deriv.DAOD_TOPQ1.e6798_s3126_r9364_p4514
mc16_13TeV.411074.PhPy8EG_A14_ttbar_hdamp258p75_ljets_BFiltBBVeto.deriv.DAOD_TOPQ1.e6798_s3126_r9364_p4514
mc16_13TeV.411075.PhPy8EG_A14_ttbar_hdamp258p75_ljets_CFiltBVeto.deriv.DAOD_TOPQ1.e6798_s3126_r9364_p4514
mc16_13TeV.411076.PhPy8EG_A14_ttbar_hdamp258p75_dil_BBFilt.deriv.DAOD_TOPQ1.e6798_s3126_r9364_p4514
mc16_13TeV.411077.PhPy8EG_A14_ttbar_hdamp258p75_dil_BFiltBBVeto.deriv.DAOD_TOPQ1.e6798_s3126_r9364_p4514
mc16_13TeV.411078.PhPy8EG_A14_ttbar_hdamp258p75_dil_CFiltBVeto.deriv.DAOD_TOPQ1.e6798_s3126_r9364_p4514
Reference
mc16_13TeV.410470.PhPy8EG_A14_ttbar_hdamp258p75_nonallhad.deriv.DAOD_TOPQ1.e6337_a875_r9364_p4514
mc16_13TeV.410471.PhPy8EG_A14_ttbar_hdamp258p75_allhad.deriv.DAOD_TOPQ1.e6337_a875_r9364_p4514
mc16_13TeV.411073.PhPy8EG_A14_ttbar_hdamp258p75_ljets_BBFilt.deriv.DAOD_TOPQ1.e6798_a875_r9364_p4514
mc16_13TeV.411074.PhPy8EG_A14_ttbar_hdamp258p75_ljets_BFiltBBVeto.deriv.DAOD_TOPQ1.e6798_a875_r9364_p4514
mc16_13TeV.411075.PhPy8EG_A14_ttbar_hdamp258p75_ljets_CFiltBVeto.deriv.DAOD_TOPQ1.e6798_a875_r9364_p4514
mc16_13TeV.411076.PhPy8EG_A14_ttbar_hdamp258p75_dil_BBFilt.deriv.DAOD_TOPQ1.e6798_a875_r9364_p4514
mc16_13TeV.411077.PhPy8EG_A14_ttbar_hdamp258p75_dil_BFiltBBVeto.deriv.DAOD_TOPQ1.e6798_a875_r9364_p4514
mc16_13TeV.411078.PhPy8EG_A14_ttbar_hdamp258p75_dil_CFiltBVeto.deriv.DAOD_TOPQ1.e6798_a875_r9364_p4514
Alternative
mc16_13TeV.410557.PowhegHerwig7EvtGen_H7UE_tt_hdamp258p75_704_SingleLep.deriv.DAOD_TOPQ1.e6366_a875_r9364_p4514
mc16_13TeV.410558.PowhegHerwig7EvtGen_H7UE_tt_hdamp258p75_704_dil.deriv.DAOD_TOPQ1.e6366_a875_r9364_p4514
mc16_13TeV.411082.PhHerwig7EG_H7UE_ttbar_hdamp258p75_ljets_BBFilt.deriv.DAOD_TOPQ1.e6799_a875_r9364_p4514
mc16_13TeV.411083.PhHerwig7EG_H7UE_ttbar_hdamp258p75_ljets_BFiltBBVeto.deriv.DAOD_TOPQ1.e6799_a875_r9364_p4514
mc16_13TeV.411084.PhHerwig7EG_H7UE_ttbar_hdamp258p75_ljets_CFiltBVeto.deriv.DAOD_TOPQ1.e6799_a875_r9364_p4514
mc16_13TeV.411085.PhHerwig7EG_H7UE_ttbar_hdamp258p75_dil_BBFilt.deriv.DAOD_TOPQ1.e6799_a875_r9364_p4514
mc16_13TeV.411086.PhHerwig7EG_H7UE_ttbar_hdamp258p75_dil_BFiltBBVeto.deriv.DAOD_TOPQ1.e6799_a875_r9364_p4514
mc16_13TeV.411087.PhHerwig7EG_H7UE_ttbar_hdamp258p75_dil_CFiltBVeto.deriv.DAOD_TOPQ1.e6799_a875_r9364_p4514
mc16_13TeV.411088.PhHerwig7EG_H7UE_ttbar_hdamp258p75_allhad_BBFilt.deriv.DAOD_TOPQ1.e6799_a875_r9364_p4514
mc16_13TeV.411089.PhHerwig7EG_H7UE_ttbar_hdamp258p75_allhad_BFiltBBVeto.deriv.DAOD_TOPQ1.e6799_a875_r9364_p4514
mc16_13TeV.411090.PhHerwig7EG_H7UE_ttbar_hdamp258p75_allhad_CFiltBVeto.deriv.DAOD_TOPQ1.e6799_a875_r9364_p4514
mc16_13TeV.410464.aMcAtNloPy8EvtGen_MEN30NLO_A14N23LO_ttbar_noShWe_SingleLep.deriv.DAOD_TOPQ1.e6762_a875_r9364_p4514
mc16_13TeV.410465.aMcAtNloPy8EvtGen_MEN30NLO_A14N23LO_ttbar_noShWe_dil.deriv.DAOD_TOPQ1.e6762_a875_r9364_p4514
mc16_13TeV.410466.aMcAtNloPy8EvtGen_MEN30NLO_A14N23LO_ttbar_noShWe_AllHadronic.deriv.DAOD_TOPQ1.e6762_a875_r9364_p4514
mc16_13TeV.412066.aMcAtNloPy8EG_A14_ttbar_hdamp258p75_ljets_BBFilt.deriv.DAOD_TOPQ1.e7129_a875_r9364_p4514
mc16_13TeV.412067.aMcAtNloPy8EG_A14_ttbar_hdamp258p75_ljets_BFiltBBVeto.deriv.DAOD_TOPQ1.e7129_a875_r9364_p4514
mc16_13TeV.412068.aMcAtNloPy8EG_A14_ttbar_hdamp258p75_ljets_CFiltBVeto.deriv.DAOD_TOPQ1.e7129_a875_r9364_p4514
mc16_13TeV.412069.aMcAtNloPy8EG_A14_ttbar_hdamp258p75_dil_BBFilt.deriv.DAOD_TOPQ1.e7129_a875_r9364_p4514
mc16_13TeV.412070.aMcAtNloPy8EG_A14_ttbar_hdamp258p75_dil_BFiltBBVeto.deriv.DAOD_TOPQ1.e7129_a875_r9364_p4514
mc16_13TeV.412071.aMcAtNloPy8EG_A14_ttbar_hdamp258p75_dil_CFiltBVeto.deriv.DAOD_TOPQ1.e7129_a875_r9364_p4514

Table 25: TOPQ1 DAOD list for $t\bar{t}$ + jets sample in this analysis.

1126 A.4 $t\bar{t}H$

1127 Table 26 is the TOPQ1 DAOD list for $t\bar{t}H$ sample in this analysis.

Nominal	
mc16_13TeV.346343.PhPy8EG_A14NNPDF23_NNPDF30ME_ttH125_allhad.deriv.DAOD_TOPQ1.e7148_s3126_r9364_p4514	
mc16_13TeV.346344.PhPy8EG_A14NNPDF23_NNPDF30ME_ttH125_semilep.deriv.DAOD_TOPQ1.e7148_s3126_r9364_p4514	
mc16_13TeV.346345.PhPy8EG_A14NNPDF23_NNPDF30ME_ttH125_dilep.deriv.DAOD_TOPQ1.e7148_s3126_r9364_p4514	
Reference	
mc16_13TeV.346343.PhPy8EG_A14NNPDF23_NNPDF30ME_ttH125_allhad.deriv.DAOD_TOPQ1.e7148_a875_r9364_p4514	
mc16_13TeV.346344.PhPy8EG_A14NNPDF23_NNPDF30ME_ttH125_semilep.deriv.DAOD_TOPQ1.e7148_a875_r9364_p4514	
mc16_13TeV.346345.PhPy8EG_A14NNPDF23_NNPDF30ME_ttH125_dilep.deriv.DAOD_TOPQ1.e7148_a875_r9364_p4514	
Alternative	
mc16_13TeV.346443.aMcAtNloPythia8EvtGen_ttH_noShWe_dilep.deriv.DAOD_TOPQ1.e7310_a875_r9364_p4514	
mc16_13TeV.346444.aMcAtNloPythia8EvtGen_ttH_noShWe_semilep.deriv.DAOD_TOPQ1.e7310_a875_r9364_p4514	
mc16_13TeV.346445.aMcAtNloPythia8EvtGen_ttH_noShWe_allhad.deriv.DAOD_TOPQ1.e7310_a875_r9364_p4514	
mc16_13TeV.346346.PhH7EG_H7UE_NNPDF30ME_ttH125_allhad.deriv.DAOD_TOPQ1.e7148_a875_r9364_p4514	
mc16_13TeV.346347.PhH7EG_H7UE_NNPDF30ME_ttH125_semilep.deriv.DAOD_TOPQ1.e7148_a875_r9364_p4514	
mc16_13TeV.346348.PhH7EG_H7UE_NNPDF30ME_ttH125_dilep.deriv.DAOD_TOPQ1.e7148_a875_r9364_p4514	

Table 26: TOPQ1 DAOD list for $t\bar{t}H$ sample in this analysis.

1128 **A.5 $t\bar{t}V$**

1129 Table 27 is the TOPQ1 DAOD list for $t\bar{t}V$ sample in this analysis.

Nominal	
mc16_13TeV.410155.aMcAtNloPythia8EvtGen_MEN30NLO_A14N23LO_ttW.deriv.DAOD_TOPQ1.e5070_s3126_r9364_p4514	
mc16_13TeV.410156.aMcAtNloPythia8EvtGen_MEN30NLO_A14N23LO_ttZnunu.deriv.DAOD_TOPQ1.e5070_s3126_r9364_p4514	
mc16_13TeV.410157.aMcAtNloPythia8EvtGen_MEN30NLO_A14N23LO_ttZqq.deriv.DAOD_TOPQ1.e5070_s3126_r9364_p4514	
mc16_13TeV.410218.aMcAtNloPythia8EvtGen_MEN30NLO_A14N23LO_ttee.deriv.DAOD_TOPQ1.e5070_s3126_r9364_p4514	
mc16_13TeV.410219.aMcAtNloPythia8EvtGen_MEN30NLO_A14N23LO_ttmumu.deriv.DAOD_TOPQ1.e5070_s3126_r9364_p4514	
mc16_13TeV.410220.aMcAtNloPythia8EvtGen_MEN30NLO_A14N23LO_ttautau.deriv.DAOD_TOPQ1.e5070_s3126_r9364_p4514	
mc16_13TeV.410276.aMcAtNloPythia8EvtGen_MEN30NLO_A14N23LO_tee_mll_1_5.deriv.DAOD_TOPQ1.e6087_s3126_r9364_p4514	
mc16_13TeV.410277.aMcAtNloPythia8EvtGen_MEN30NLO_A14N23LO_ttmumu_mll_1_5.deriv.DAOD_TOPQ1.e6087_s3126_r9364_p4514	
mc16_13TeV.410278.aMcAtNloPythia8EvtGen_MEN30NLO_A14N23LO_ttautau_mll_1_5.deriv.DAOD_TOPQ1.e6087_s3126_r9364_p4514	
Alternative	
mc16_13TeV.410142.Sherpa_NNPDF30NNLO_ttll_mll5.deriv.DAOD_TOPQ1.e4686_s3126_r9364_p4514	
mc16_13TeV.410143.Sherpa_NNPDF30NNLO_ttZnnqq.deriv.DAOD_TOPQ1.e4686_s3126_r9364_p4514	
mc16_13TeV.410144.Sherpa_NNPDF30NNLO_ttW.deriv.DAOD_TOPQ1.e4686_s3126_r9364_p4514	

Table 27: TOPQ1 DAOD list for $t\bar{t}V$ sample in this analysis.

1130 **A.6 Single top**

1131 Table 28 is the TOPQ1 DAOD list for single top sample in this analysis.

Nominal
mc16_13TeV.410644.PowhegPythia8EvtGen_A14_singletop_schan_lept_top.deriv.DAOD_TOPQ1.e6527_s3126_r9364_p4514
mc16_13TeV.410645.PowhegPythia8EvtGen_A14_singletop_schan_lept_antitop.deriv.DAOD_TOPQ1.e6527_s3126_r9364_p4514
mc16_13TeV.410646.PowhegPythia8EvtGen_A14_Wt_DR_inclusive_top.deriv.DAOD_TOPQ1.e6552_s3126_r9364_p4514
mc16_13TeV.410647.PowhegPythia8EvtGen_A14_Wt_DR_inclusive_antitop.deriv.DAOD_TOPQ1.e6552_s3126_r9364_p4514
mc16_13TeV.410658.PhPy8EG_A14_tchan_BW50_lept_top.deriv.DAOD_TOPQ1.e6671_s3126_r9364_p4514
mc16_13TeV.410659.PhPy8EG_A14_tchan_BW50_lept_antitop.deriv.DAOD_TOPQ1.e6671_s3126_r9364_p4514
Reference
mc16_13TeV.410644.PowhegPythia8EvtGen_A14_singletop_schan_lept_top.deriv.DAOD_TOPQ1.e6527_a875_r9364_p4514
mc16_13TeV.410645.PowhegPythia8EvtGen_A14_singletop_schan_lept_antitop.deriv.DAOD_TOPQ1.e6527_a875_r9364_p4514
mc16_13TeV.410646.PowhegPythia8EvtGen_A14_Wt_DR_inclusive_top.deriv.DAOD_TOPQ1.e6552_a875_r9364_p4514
mc16_13TeV.410647.PowhegPythia8EvtGen_A14_Wt_DR_inclusive_antitop.deriv.DAOD_TOPQ1.e6552_a875_r9364_p4514
mc16_13TeV.410658.PhPy8EG_A14_tchan_BW50_lept_top.deriv.DAOD_TOPQ1.e6671_a875_r9364_p4514
mc16_13TeV.410659.PhPy8EG_A14_tchan_BW50_lept_antitop.deriv.DAOD_TOPQ1.e6671_a875_r9364_p4514
Alternative
mc16_13TeV.410654.PowhegPythia8EvtGen_A14_Wt_DS_inclusive_top.deriv.DAOD_TOPQ1.e6552_s3126_r9364_p4514
mc16_13TeV.410655.PowhegPythia8EvtGen_A14_Wt_DS_inclusive_antitop.deriv.DAOD_TOPQ1.e6552_s3126_r9364_p4514
mc16_13TeV.411032.PowhegHerwig7EvtGen_H7UE_704_tchan_lept_antitop.deriv.DAOD_TOPQ1.e6719_a875_r9364_p4514
mc16_13TeV.411033.PowhegHerwig7EvtGen_H7UE_704_tchan_lept_top.deriv.DAOD_TOPQ1.e6719_a875_r9364_p4514
mc16_13TeV.411034.PhHerwig7EG_H7UE_singletop_schan_lept_top.deriv.DAOD_TOPQ1.e6734_a875_r9364_p4514
mc16_13TeV.411035.PhHerwig7EG_H7UE_singletop_schan_lept_antitop.deriv.DAOD_TOPQ1.e6734_a875_r9364_p4514
mc16_13TeV.411036.PowhegHerwig7EvtGen_H7UE_Wt_DR_inclusive_top.deriv.DAOD_TOPQ1.e6702_a875_r9364_p4514
mc16_13TeV.411037.PowhegHerwig7EvtGen_H7UE_Wt_DR_inclusive_antitop.deriv.DAOD_TOPQ1.e6702_a875_r9364_p4514
mc16_13TeV.412002.aMcAtNloPythia8EvtGen_HThalfscale_tW_inclusive.deriv.DAOD_TOPQ1.e6817_a875_r9364_p4514
mc16_13TeV.412004.aMcAtNloPy8EG_tchan_NLO.deriv.DAOD_TOPQ1.e6888_a875_r9364_p4514

Table 28: TOPQ1 DAOD list for single top sample in this analysis.

1132 A.7 tH

1133 Table 29 is the TOPQ1 DAOD list for tH sample in this analysis.

Nominal
mc16_13TeV.346676.aMcAtNloPythia8EvtGen_tHjb125_4fl_CPalpha_0.deriv.DAOD_TOPQ1.e7815_a875_r9364_p4514
mc16_13TeV.346678.aMcAtNloPythia8EvtGen_tWH125_4fl_CPalpha_0.deriv.DAOD_TOPQ1.e7816_a875_r9364_p4514

Table 29: TOPQ1 DAOD list for tH sample in this analysis.

1134 A.8 Rare t processes

1135 Table 30 is the TOPQ1 DAOD list for rare t processes' sample in this analysis.

Nominal
mc16_13TeV.410560.MadGraphPythia8EvtGen_A14_tZ_4fl_tchan_noAllHad.deriv.DAOD_TOPQ1.e5803_s3126_r9364_p4514
mc16_13TeV.410408.aMcAtNloPythia8EvtGen_tWZ_Ztoll_minDR1.deriv.DAOD_TOPQ1.e6423_s3126_r9364_p4514
mc16_13TeV.412043.aMcAtNloPythia8EvtGen_A14NNPDF31_SM4topsNLO.deriv.DAOD_TOPQ1.e7101_a875_r9364_p4514

Table 30: TOPQ1 DAOD list for rare processes' sample in this analysis.

1136 A.9 Vector bosons plus jets

1137 A.9.1 $W +$ jets

1138 Table 31 is the TOPQ1 DAOD list for $W +$ jets sample in this analysis.

Nominal

mc16_13TeV.364170.Sherpa_221_NNPDF30NNLO_Wenu_MAXHTPTV0_70_CVetoBVeto.deriv.DAOD_TOPQ1.e5340_s3126_r9364_p4512
 mc16_13TeV.364171.Sherpa_221_NNPDF30NNLO_Wenu_MAXHTPTV0_70_CFilterBVeto.deriv.DAOD_TOPQ1.e5340_s3126_r9364_p4512
 mc16_13TeV.364172.Sherpa_221_NNPDF30NNLO_Wenu_MAXHTPTV0_70_BFilter.deriv.DAOD_TOPQ1.e5340_s3126_r9364_p4512
 mc16_13TeV.364173.Sherpa_221_NNPDF30NNLO_Wenu_MAXHTPTV0_140_CVetoBVeto.deriv.DAOD_TOPQ1.e5340_s3126_r9364_p4512
 mc16_13TeV.364174.Sherpa_221_NNPDF30NNLO_Wenu_MAXHTPTV0_140_CFilterBVeto.deriv.DAOD_TOPQ1.e5340_s3126_r9364_p4512
 mc16_13TeV.364175.Sherpa_221_NNPDF30NNLO_Wenu_MAXHTPTV0_140_BFilter.deriv.DAOD_TOPQ1.e5340_s3126_r9364_p4512
 mc16_13TeV.364176.Sherpa_221_NNPDF30NNLO_Wenu_MAXHTPTV0_280_CVetoBVeto.deriv.DAOD_TOPQ1.e5340_s3126_r9364_p4512
 mc16_13TeV.364177.Sherpa_221_NNPDF30NNLO_Wenu_MAXHTPTV0_280_CFilterBVeto.deriv.DAOD_TOPQ1.e5340_s3126_r9364_p4512
 mc16_13TeV.364178.Sherpa_221_NNPDF30NNLO_Wenu_MAXHTPTV0_280_BFilter.deriv.DAOD_TOPQ1.e5340_s3126_r9364_p4512
 mc16_13TeV.364179.Sherpa_221_NNPDF30NNLO_Wenu_MAXHTPTV280_500_CVetoBVeto.deriv.DAOD_TOPQ1.e5340_s3126_r9364_p4512
 mc16_13TeV.364180.Sherpa_221_NNPDF30NNLO_Wenu_MAXHTPTV280_500_CFilterBVeto.deriv.DAOD_TOPQ1.e5340_s3126_r9364_p4512
 mc16_13TeV.364181.Sherpa_221_NNPDF30NNLO_Wenu_MAXHTPTV280_500_BFilter.deriv.DAOD_TOPQ1.e5340_s3126_r9364_p4512
 mc16_13TeV.364182.Sherpa_221_NNPDF30NNLO_Wenu_MAXHTPTV500_1000.deriv.DAOD_TOPQ1.e5340_s3126_r9364_p4512
 mc16_13TeV.364183.Sherpa_221_NNPDF30NNLO_Wenu_MAXHTPTV1000_E_CMS.deriv.DAOD_TOPQ1.e5340_s3126_r9364_p4512
 mc16_13TeV.364156.Sherpa_221_NNPDF30NNLO_Wmumu_MAXHTPTV0_70_CVetoBVeto.deriv.DAOD_TOPQ1.e5340_s3126_r9364_p4512
 mc16_13TeV.364157.Sherpa_221_NNPDF30NNLO_Wmumu_MAXHTPTV0_70_CFilterBVeto.deriv.DAOD_TOPQ1.e5340_s3126_r9364_p4512
 mc16_13TeV.364158.Sherpa_221_NNPDF30NNLO_Wmumu_MAXHTPTV0_70_BFilter.deriv.DAOD_TOPQ1.e5340_s3126_r9364_p4512
 mc16_13TeV.364159.Sherpa_221_NNPDF30NNLO_Wmumu_MAXHTPTV0_140_CVetoBVeto.deriv.DAOD_TOPQ1.e5340_s3126_r9364_p4512
 mc16_13TeV.364160.Sherpa_221_NNPDF30NNLO_Wmumu_MAXHTPTV0_140_CFilterBVeto.deriv.DAOD_TOPQ1.e5340_s3126_r9364_p4512
 mc16_13TeV.364161.Sherpa_221_NNPDF30NNLO_Wmumu_MAXHTPTV0_140_BFilter.deriv.DAOD_TOPQ1.e5340_s3126_r9364_p4512
 mc16_13TeV.364162.Sherpa_221_NNPDF30NNLO_Wmumu_MAXHTPTV0_140_CVetoBVeto.deriv.DAOD_TOPQ1.e5340_s3126_r9364_p4512
 mc16_13TeV.364163.Sherpa_221_NNPDF30NNLO_Wmumu_MAXHTPTV0_140_CFilterBVeto.deriv.DAOD_TOPQ1.e5340_s3126_r9364_p4512
 mc16_13TeV.364164.Sherpa_221_NNPDF30NNLO_Wmumu_MAXHTPTV0_140_BFilter.deriv.DAOD_TOPQ1.e5340_s3126_r9364_p4512
 mc16_13TeV.364165.Sherpa_221_NNPDF30NNLO_Wmumu_MAXHTPTV0_280_500_CVetoBVeto.deriv.DAOD_TOPQ1.e5340_s3126_r9364_p4512
 mc16_13TeV.364166.Sherpa_221_NNPDF30NNLO_Wmumu_MAXHTPTV0_280_500_CFilterBVeto.deriv.DAOD_TOPQ1.e5340_s3126_r9364_p4512
 mc16_13TeV.364167.Sherpa_221_NNPDF30NNLO_Wmumu_MAXHTPTV0_280_500_BFilter.deriv.DAOD_TOPQ1.e5340_s3126_r9364_p4512
 mc16_13TeV.364168.Sherpa_221_NNPDF30NNLO_Wmumu_MAXHTPTV0_500_1000.deriv.DAOD_TOPQ1.e5340_s3126_r9364_p4512
 mc16_13TeV.364169.Sherpa_221_NNPDF30NNLO_Wmumu_MAXHTPTV1000_E_CMS.deriv.DAOD_TOPQ1.e5340_s3126_r9364_p4512
 mc16_13TeV.364184.Sherpa_221_NNPDF30NNLO_Wtaunu_MAXHTPTV0_70_CVetoBVeto.deriv.DAOD_TOPQ1.e5340_s3126_r9364_p4512
 mc16_13TeV.364185.Sherpa_221_NNPDF30NNLO_Wtaunu_MAXHTPTV0_70_CFilterBVeto.deriv.DAOD_TOPQ1.e5340_s3126_r9364_p4512
 mc16_13TeV.364186.Sherpa_221_NNPDF30NNLO_Wtaunu_MAXHTPTV0_70_BFilter.deriv.DAOD_TOPQ1.e5340_s3126_r9364_p4512
 mc16_13TeV.364187.Sherpa_221_NNPDF30NNLO_Wtaunu_MAXHTPTV0_140_CVetoBVeto.deriv.DAOD_TOPQ1.e5340_s3126_r9364_p4512
 mc16_13TeV.364188.Sherpa_221_NNPDF30NNLO_Wtaunu_MAXHTPTV0_140_CFilterBVeto.deriv.DAOD_TOPQ1.e5340_s3126_r9364_p4512
 mc16_13TeV.364189.Sherpa_221_NNPDF30NNLO_Wtaunu_MAXHTPTV0_140_BFilter.deriv.DAOD_TOPQ1.e5340_s3126_r9364_p4512
 mc16_13TeV.364190.Sherpa_221_NNPDF30NNLO_Wtaunu_MAXHTPTV0_280_CVetoBVeto.deriv.DAOD_TOPQ1.e5340_s3126_r9364_p4512
 mc16_13TeV.364191.Sherpa_221_NNPDF30NNLO_Wtaunu_MAXHTPTV0_280_CFilterBVeto.deriv.DAOD_TOPQ1.e5340_s3126_r9364_p4512
 mc16_13TeV.364192.Sherpa_221_NNPDF30NNLO_Wtaunu_MAXHTPTV0_280_BFilter.deriv.DAOD_TOPQ1.e5340_s3126_r9364_p4512
 mc16_13TeV.364193.Sherpa_221_NNPDF30NNLO_Wtaunu_MAXHTPTV0_500_CVetoBVeto.deriv.DAOD_TOPQ1.e5340_s3126_r9364_p4512
 mc16_13TeV.364194.Sherpa_221_NNPDF30NNLO_Wtaunu_MAXHTPTV0_500_CFilterBVeto.deriv.DAOD_TOPQ1.e5340_s3126_r9364_p4512
 mc16_13TeV.364195.Sherpa_221_NNPDF30NNLO_Wtaunu_MAXHTPTV0_500_BFilter.deriv.DAOD_TOPQ1.e5340_s3126_r9364_p4512
 mc16_13TeV.364196.Sherpa_221_NNPDF30NNLO_Wtaunu_MAXHTPTV500_1000.deriv.DAOD_TOPQ1.e5340_s3126_r9364_p4512
 mc16_13TeV.364197.Sherpa_221_NNPDF30NNLO_Wtaunu_MAXHTPTV1000_E_CMS.deriv.DAOD_TOPQ1.e5340_s3126_r9364_p4512

Table 31: TOPQ1 DAOD list for $W + \text{jets}$ sample in this analysis.**A.9.2 $Z + \text{jets}$**

¹¹³⁹ Table 32 is the TOPQ1 DAOD list for $Z + \text{jets}$ sample in this analysis.

¹¹⁴⁰ Table 32 is the TOPQ1 DAOD list for $Z + \text{jets}$ sample in this analysis.

Nominal

Table 32: TOPQ1 DAOD list for $Z + \text{jets}$ sample in this analysis.

1141 A.10 Diboson

1142 Table 33 is the TOPQ1 DAOD list for diboson sample in this analysis.

Nominal
mc16_13TeV.364250.Sherpa_222_NNPDF30NNLO_llll.deriv.DAOD_TOPQ1.e5894_s3126_r9364_p4512
mc16_13TeV.364253.Sherpa_222_NNPDF30NNLO_lllv.deriv.DAOD_TOPQ1.e5916_s3126_r9364_p4512
mc16_13TeV.364254.Sherpa_222_NNPDF30NNLO_llvv.deriv.DAOD_TOPQ1.e5916_s3126_r9364_p4512
mc16_13TeV.364255.Sherpa_222_NNPDF30NNLO_lvvv.deriv.DAOD_TOPQ1.e5916_s3126_r9364_p4512
mc16_13TeV.364288.Sherpa_222_NNPDF30NNLO_llll_lowMllPtComplement.deriv.DAOD_TOPQ1.e6096_s3126_r9364_p4512
mc16_13TeV.364289.Sherpa_222_NNPDF30NNLO_lllv_lowMllPtComplement.deriv.DAOD_TOPQ1.e6133_s3126_r9364_p4512
mc16_13TeV.364290.Sherpa_222_NNPDF30NNLO_llvv_lowMllPtComplement.deriv.DAOD_TOPQ1.e6096_s3126_r9364_p4512
mc16_13TeV.363355.Sherpa_221_NNPDF30NNLO_ZqqZv.deriv.DAOD_TOPQ1.e5525_s3126_r9364_p4512
mc16_13TeV.363356.Sherpa_221_NNPDF30NNLO_ZqqZll.deriv.DAOD_TOPQ1.e5525_s3126_r9364_p4512
mc16_13TeV.363357.Sherpa_221_NNPDF30NNLO_WqqZvv.deriv.DAOD_TOPQ1.e5525_s3126_r9364_p4512
mc16_13TeV.363358.Sherpa_221_NNPDF30NNLO_WqqZll.deriv.DAOD_TOPQ1.e5525_s3126_r9364_p4512
mc16_13TeV.363359.Sherpa_221_NNPDF30NNLO_WpqqWmlv.deriv.DAOD_TOPQ1.e5583_s3126_r9364_p4512
mc16_13TeV.363360.Sherpa_221_NNPDF30NNLO_WplvWmqq.deriv.DAOD_TOPQ1.e5983_s3126_r9364_p4512
mc16_13TeV.363489.Sherpa_221_NNPDF30NNLO_WlvZqq.deriv.DAOD_TOPQ1.e5525_s3126_r9364_p4512
mc16_13TeV.363494.Sherpa_221_NNPDF30NNLO_vvvv.deriv.DAOD_TOPQ1.e5332_s3126_r9364_p4512
mc16_13TeV.364283.Sherpa_222_NNPDF30NNLO_llljjj_EW6.deriv.DAOD_TOPQ1.e6055_s3126_r9364_p4512
mc16_13TeV.364284.Sherpa_222_NNPDF30NNLO_llvjjj_EW6.deriv.DAOD_TOPQ1.e6055_s3126_r9364_p4512
mc16_13TeV.364285.Sherpa_222_NNPDF30NNLO_llvijj_EW6.deriv.DAOD_TOPQ1.e6055_s3126_r9364_p4512
mc16_13TeV.364287.Sherpa_222_NNPDF30NNLO_llvjjj_ss_EW6.deriv.DAOD_TOPQ1.e6055_s3126_r9364_p4512
mc16_13TeV.345705.Sherpa_222_NNPDF30NNLO_ggllll_0M41130.deriv.DAOD_TOPQ1.e6213_s3126_r9364_p4512
mc16_13TeV.345706.Sherpa_222_NNPDF30NNLO_ggllll_130M41.deriv.DAOD_TOPQ1.e6213_s3126_r9364_p4512
mc16_13TeV.345723.Sherpa_222_NNPDF30NNLO_ggllvvZZ.deriv.DAOD_TOPQ1.e6213_s3126_r9364_p4512

Table 33: TOPQ1 DAOD list for diboson sample in this analysis.

1143 **B Signal/background comparisons**

1144 **B.1 BDT input variables**

1145 Figures 66(a) to Fig.66(n) compare the shape of the variables included in the BDT for all H^+ signal masses
1146 and background.

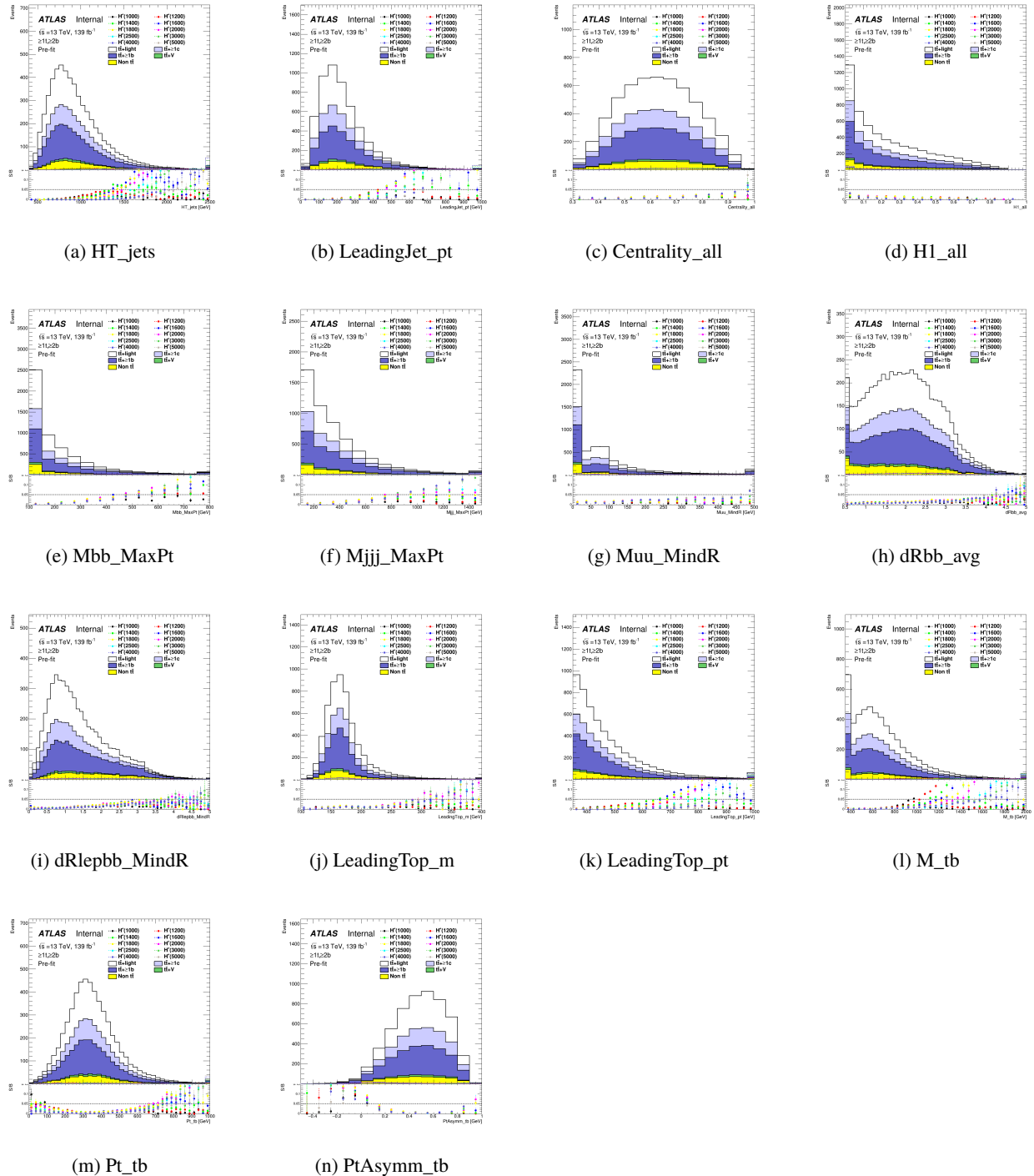


Figure 66: Comparison of the kinematic variables included in the BDT in the SR for the various H^+ signal masses between signal and background.

1147 B.2 BDT output

1148 Figures 67(a) to Figure 67(j) compare the shape of BDT output distribution in SR region between the
1149 signal and background on each H^+ signal mass hypothesis at equal bin intervals.

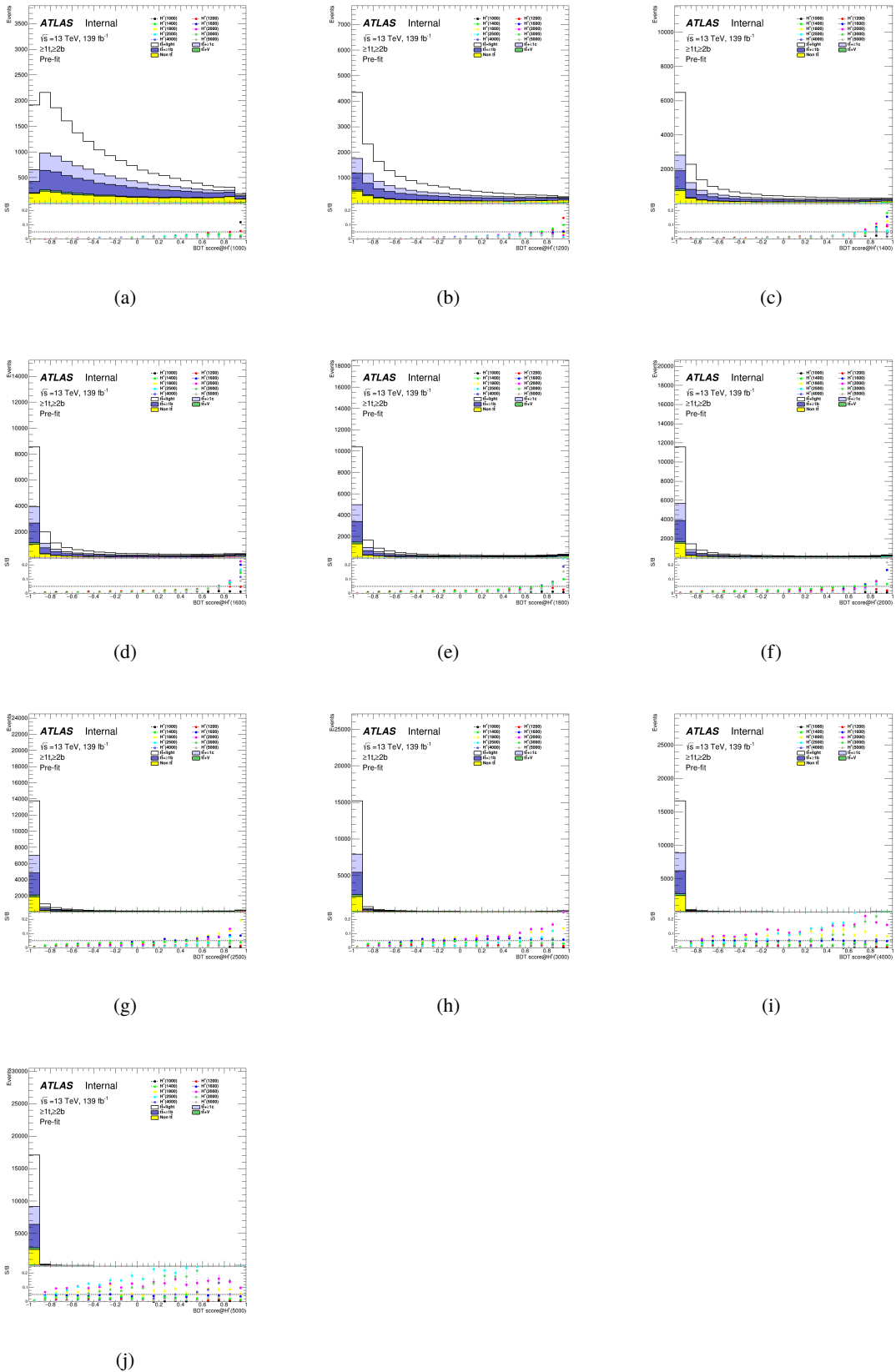


Figure 67

1150 Figures 68(a) to Fig.68(j) compare the shape of BDT output distribution in SR region between the signal
1151 and background on each H^+ signal mass hypothesis at not equal bin intervals. These binning is optimised
1152 using TRexFitter.

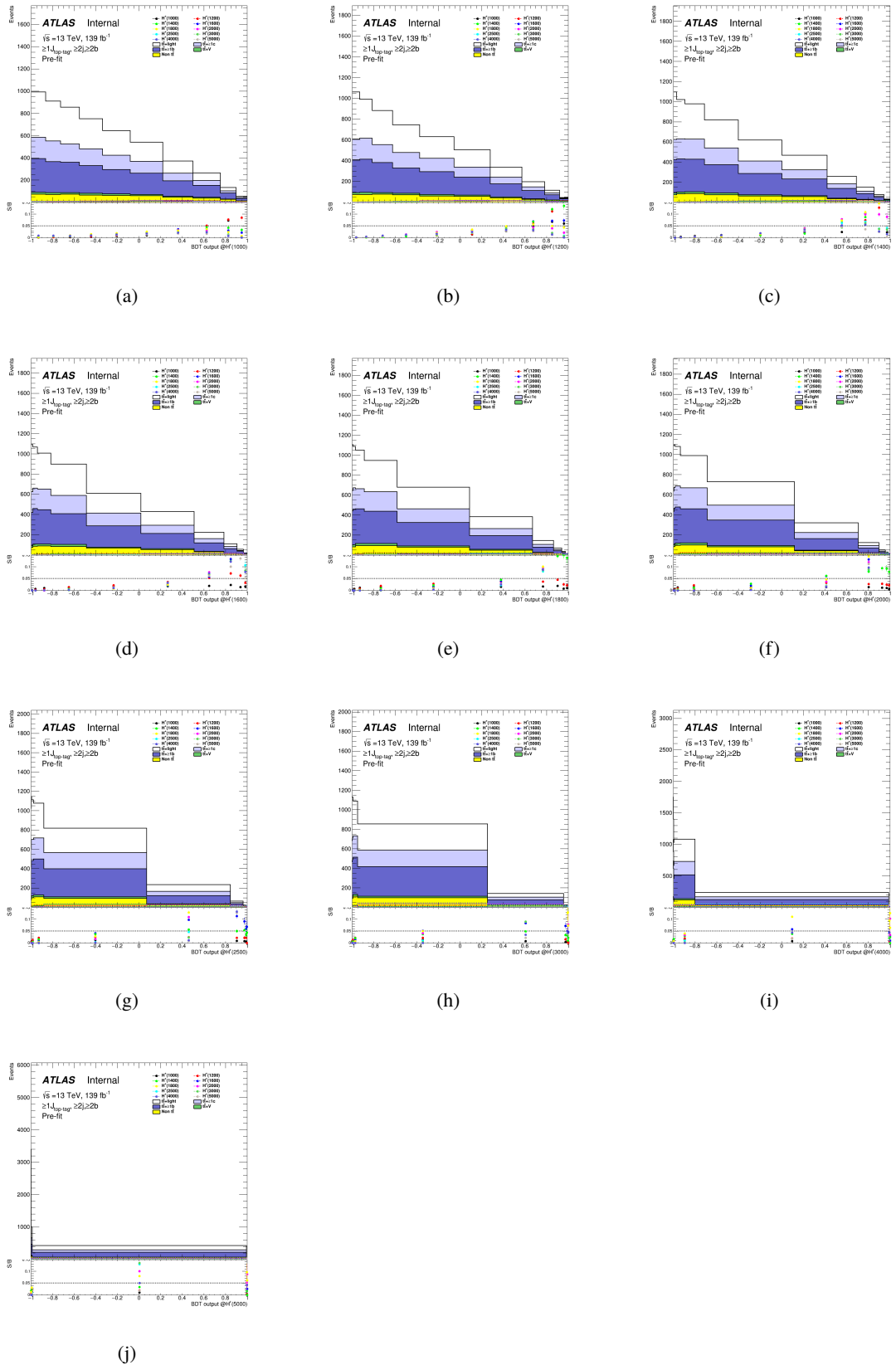


Figure 68

₁₁₅₃ Figures 69(a) to Figure 69(j) are BDT output distributions for events used in the derivation of weight factors.
₁₁₅₄ These compare the shape of BDT output distribution in SR region between the signal and background on
₁₁₅₅ each H^+ signal mass hypothesis at equal bin intervals.

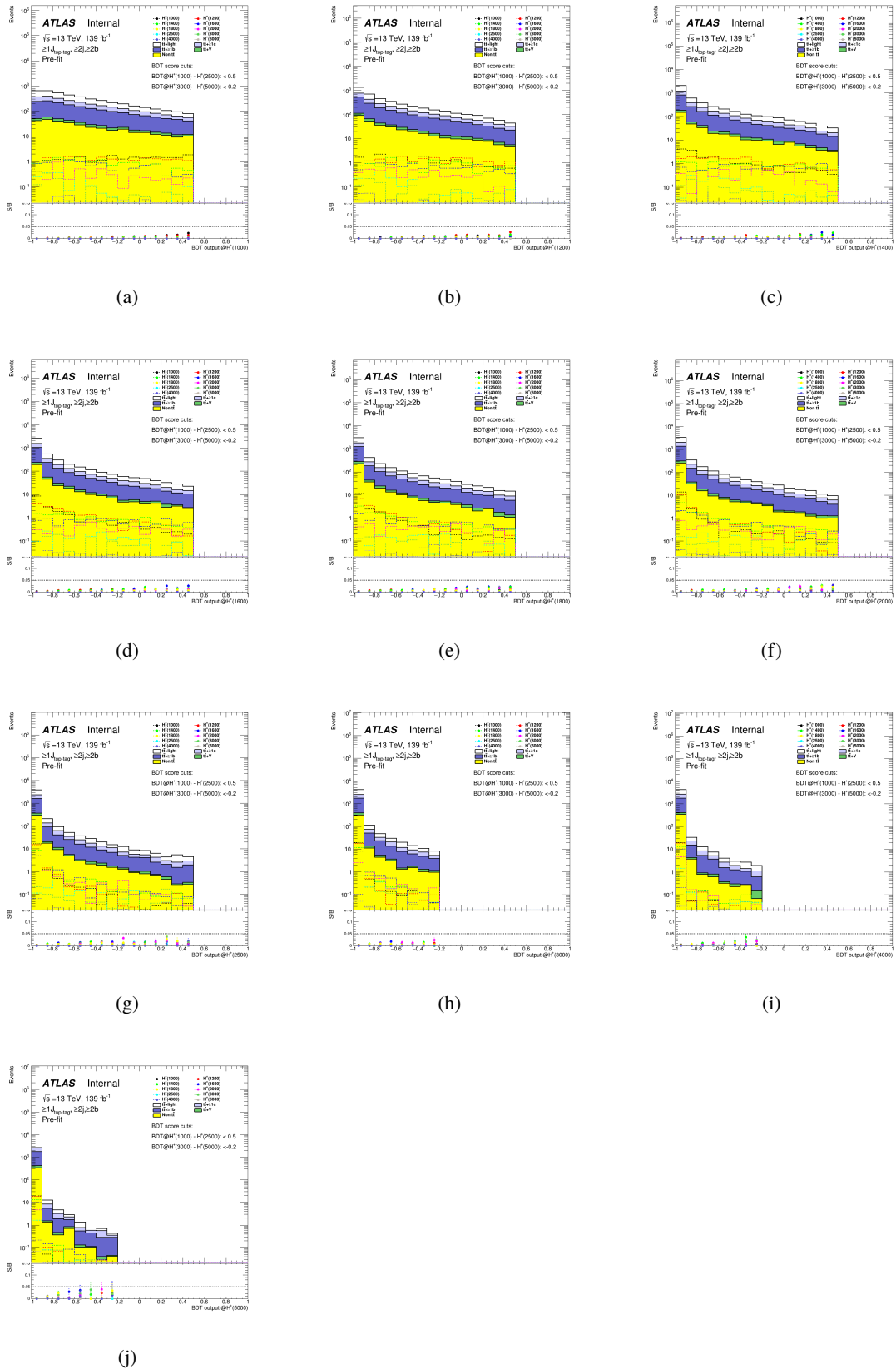


Figure 69

1156 **B.3 H_T^{jets} distribution in CR**

1157 Figures 70 compare the shape of H_T^{jets} distribution in CR region between the signal and background on
 1158 each H^+ signal mass hypothesis at equal bin intervals.

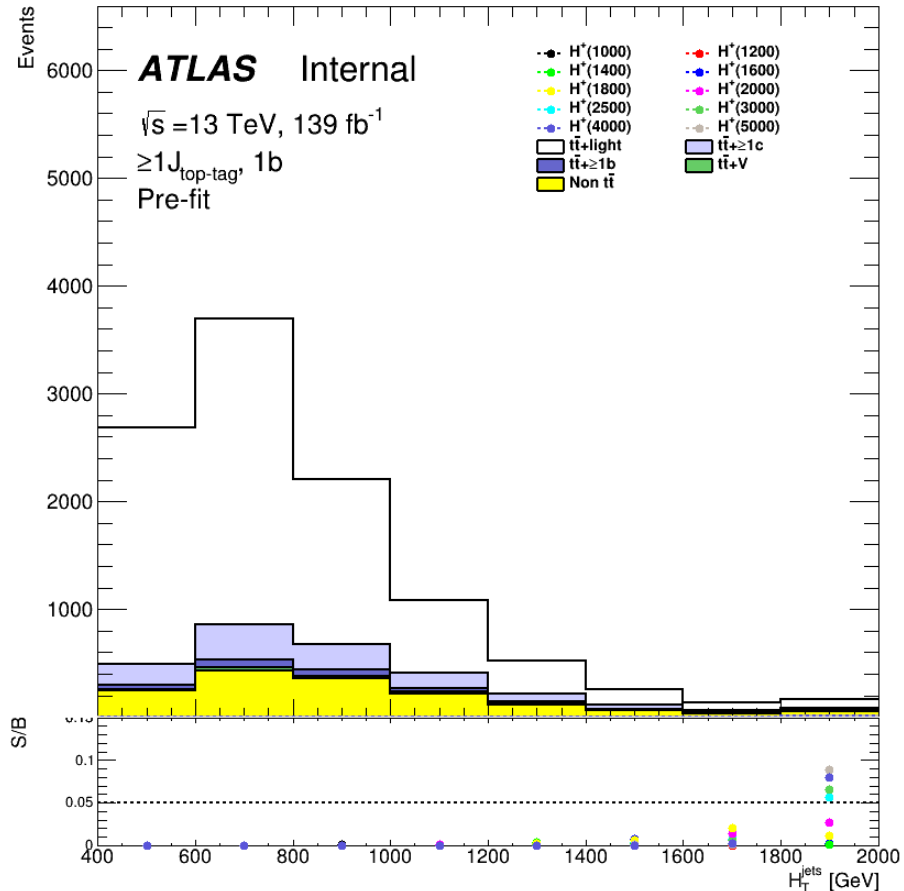


Figure 70: Comparison of the H_T^{jets} in the CR for the various H^+ signal masses between signal and background.

₁₁₅₉ **C Pruning**

₁₁₆₀ **C.1 Asimov fit**

₁₁₆₁ Figures 71 to 77 show the pruning applied in the systematic uncertainties for the Asimov fits for all the H^+
₁₁₆₂ mass fits.

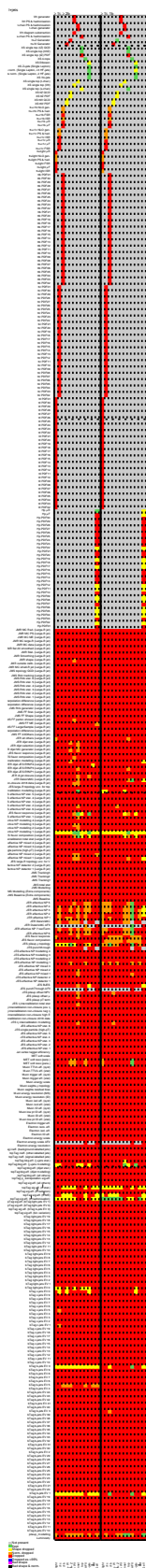


Figure 71: Pruned systematic uncertainties in the 1000 GeV H^+ mass Asimov fits

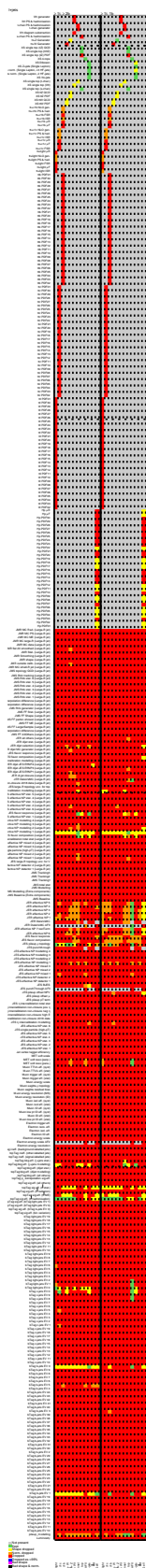


Figure 72: Pruned systematic uncertainties in the 1200 GeV H^+ mass Asimov fits

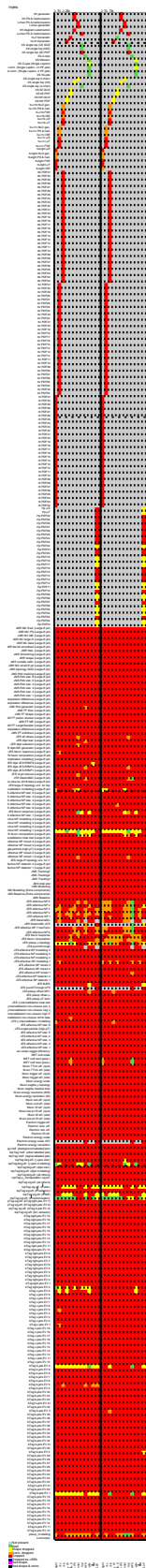


Figure 73: Pruned systematic uncertainties in the 1400 GeV H^+ mass Asimov fits

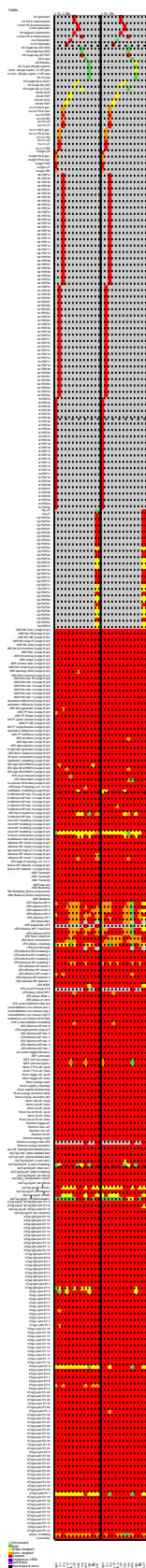


Figure 74: Pruned systematic uncertainties in the 1600 GeV H^+ mass Asimov fits

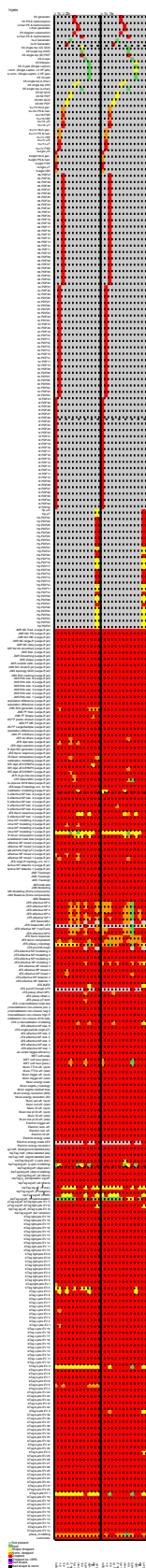


Figure 75: Pruned systematic uncertainties in the 2000 GeV H^+ mass Asimov fits

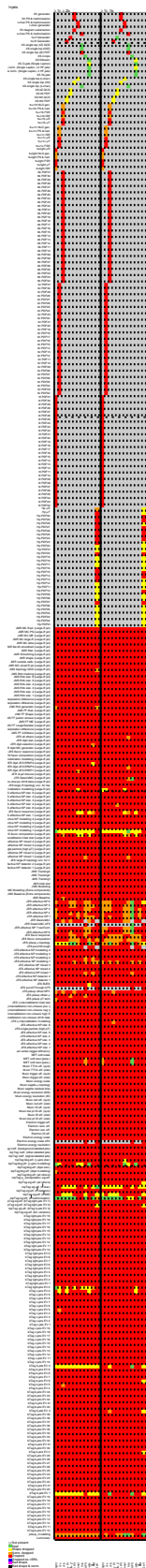


Figure 76: Pruned systematic uncertainties in the 2500 GeV H^+ mass Asimov fits

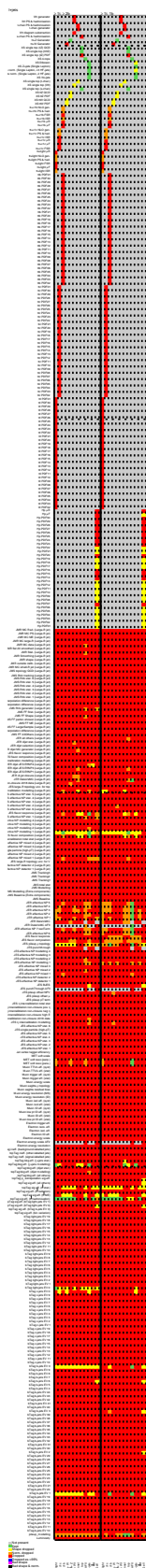


Figure 77: Pruned systematic uncertainties in the 3000 GeV H^+ mass Asimov fits